Optical Orientation in Self Assembled Quantum Dots.

by

Gregory C. Stevens

A thesis submitted for the degree of
Doctor of Philosophy
at the Department of Physics and Astronomy,
University of Southampton

January 2002

UNIVERSITY OF SOUTHAMPTON

ABSTRACT

FACULTY OF SCIENCE

PHYSICS

Doctor of Philosophy

Optical Orientation in Self Assembled Quantum Dots

by Gregory Charles Stevens

We examined Zeeman splitting in a series of $In_xGa_{(1-x)}As/GaAs$ self assembled quantum dot samples (SAQD's) with different polarisations of the incident beam. All these measurements were made in very low external magnetic fields where direct determination of the Zeeman splitting energy is impossible due to the small energy difference between the split states in comparison to the photoluminescence linewidth. The use of a technique developed by M. J. Snelling allowed us to obtain the Zeeman splitting and hence the excitonic g-factors indirectly. We observed a linear low field splitting, becoming increasingly non-linear at higher fields. We attribute this non-linearity to field induced level mixing. It is believed these are the first low field measurements in these structures.

A number of apparent nuclear effects in the Zeeman splitting measurements led to the possibility of the examination of nuclear effects in these structures. The transverse and oblique Hanle effects allowed us to obtain the sign of the electronic g-factors in two of our samples. For one sample, a (311) grown $In_{0.5}Ga_{0.5}As/GaAs$ SAQD sample, we were able to ascertain the spin relaxation time, the maximum value of the nuclear field, and provide evidence of the existence of nuclear spin freezing in at least one of our samples.

We have then used a novel technique investigated by D. J. Guerrier, to examine optically detected nuclear magnetic resonance in our samples. We believe this is the first such study on these structures. We could not ascertain the dipolar indium resonance signal, even though all other isotopes were seen. We have therefore suggested a number of possible mechanisms that may be responsible for the lack of an indium resonance signal.

Contents

Acknowledgements

First and foremost I wish to sincerely thank my supervisor Prof. Richard Harley for his constant enthusiasm and guidance. My gratitude must also go to Prof. J. Bowden for discussions on NMR.

I must thank my colleague, Philip Marsden with whom I worked in collaboration during the first year for his advise, enthusiasm and friendship.

The lunchtime crowd deserve a special mention: Steve, Michele, Andy, Matthew and Gareth who have helped, supported and guided throughout my Ph.D., for this I am very grateful.

I would like to acknowledge the help of all the technical staff, Colin Miles, Vince Davey, Mark Sculley, Alan Purvy and Tom Perkins, whose assistance I found invaluable.

My thanks must also go to Phil Larkin, with whom I shared a house for three years, for his friendship and wisdom.

Lastly I would like to thank Cheryl for her friendship, and the incredible kindness that she shows all people.

For my Parents

Chapter 1

Introduction

1.1 Introduction

There are a number of methods to confine electronic carriers to a specific region of space. Research in this field is led by the sandwiching of lattice matched semiconductors together, such that the different band-gaps produce a potential well that confine carriers in one dimension, this is the so called quantum well [1]. A number of spin off applications have since transformed numerous industries [2][3], and this in turn has led to interest in the study of materials that confine carriers in more than one dimension [1].

The ultimate confinement geometry is three dimensional confinement in which the motion of the carriers is confined in all directions with dimensions smaller than the exciton Bohr radius (a_B):

$$a_B = 4\pi\epsilon\frac{\hbar^2}{\mu e^2} \tag{1.1}$$

where e is the particles charge, μ is the reduced mass, (given as $\frac{1}{\mu} = \frac{1}{m_e} + \frac{1}{m_h}$), m_e is the electron mass, m_h is the hole mass, and ϵ is the dielectric constant.

One of the earliest successful methods used to obtain three dimensional confinement was the use of the fluctuations of the interfaces in quantum wells, close examination of the photoluminescence emanating from these structures showed features characteristic of three dimensional confinement of electrons. Another method is using the chemistry of reactions to produce colloidal quantum dots [4]. These are free standing spheres of one

type of material and are strain free. In order to ensure the suppression of the coagulation of small dots during growth, they are coated with an organic ligand, having a size distribution of 20–100Å. Due to the fact that they are free standing, they may be studied in solution, as powder, or arrays in films. Colloidal dots have been realised in III-V, II-VI and I-VII semiconductors [5].

The third technique is the production of the so-called self-assembled quantum dots. The aim of the work described in this thesis was to investigate the electronic and other properties of self assembled quantum dots (SAQDs) using first, the Zeeman effect to determine the electronic g-factors, and secondly, optically detected nuclear magnetic resonance (ODNMR) which can potentially give information on chemical composition and internal strain in III-V nano-structures [6] [7]. ODNMR relies on the alignment of the nuclear moments via polarised optical pumping which is predicted to be an efficient process in these systems due to the strong electron confinement. A necessary preliminary to ODNMR is the examination of the oblique Hanle effect, which allows the characterisation of the nuclear alignment.

SAQDs have shown the narrowest size distribution [8]. The main methods of manufacture of these structures are molecular beam epitaxy, nano-scale patterning, and metal-organic chemical vapour deposition, or a mixture of these growth techniques. These crystal growth techniques have led to the production of high quality samples with a dot size distribution of less than 10% [5].

In the Stanski-Krastinov growth mode [9][10], a layer of semiconductor is

grown on top of a substrate having a lattice mismatch between the two greater than 5%, a very strained layer begins to form up to a critical thickness (L_c), thereafter, 3 dimensional islands begin to form that become the quantum dots. The growth of the islands is very dependent on the amount of lattice mismatch, the crystallographic orientation of the substrate, the substrate roughness and temperature. The islands will form up to a critical thickness, after which, dislocations begin to form in order to minimise the strain between the substrate and layer material. The zero dimensional density of states exhibited by these structures have realized lasers benefiting from a reduced current threshold and higher temperature stability [11].

The islands exhibit a number of different geometries. In the (100) growth direction, the dots are pyramidal shaped whereas, in the (311) direction [12], they are arrow shaped. However, the size and geometry is currently controversial due to the fact that any capping layer can severely distort the geometry. From a theoretical point of view, the critical coverage parameter L_c has been reported in the range 1.0-1.8ML by including numerous refinements to their calculations [13][14][15][16][17]. However, from an experimental point of view, a unifying picture SAQD characteristics is complicated by actual growth conditions. The SAQD emission energy depends on growth rates [18], growth temperatures, molecular beam fluxes [20], and the thicknesses, temperatures and growth rates of the capping layers. [13][21]. Indium Arsenide (InAs) SAQDs embedded in Gallium Arsenide (GaAs) have an average distance apart of about 60 nm, a height of 3nm, and a 12 nm half base. The size distribution is of the order $\pm$ 5-15%

It has to be noted that as the morphology of the crystal changes, L_c also changes significantly [5]. Furthermore, the dot density and shape also change with increasing mixed crystal composition. Since both size and shape vary, and changes in the fraction of indium in the alloy lead to shifts in the optical absorption features, an exact knowledge of the Indium fraction becomes essential in $In_xGa_{x-1}As$ for the understanding of the electronic structure. The samples in this report are all of the self-assembled type and therefore it is this type of quantum dot we will concentrate on.

Initial theoretical papers were not able to explain the low luminescence efficiency found in these structures [5][23], further papers predicted different states, as an example Fafard [19] found the existence of only one excited state, but Grundmann [24] found numerous states hybridizing with the wetting layer. As a consequence of this, numerous authors have taken very different methods to calculate the electronic structure in SAQDs, Zunger has taken the direct diagonalisation approach[5][26], solving the single particle Schrödinger equation in the presence of a pseudo-potential of surrounding atoms. On the other hand, Grundmann has relied on the $k.p$ theory, but incorporating the effects of strain into the calculation [24].

To compound this, similarly grown SAQDs also seem to show different properties. For example [22] found three different responses from SAQDs on the same sample. Therefore, information on the electronic structure is of paramount importance in the understanding of these structures. The electron g-factor is an important parameter in the understanding of the electronic structure of these systems because it is a function of the spin and orbital angular momentum, and therefore gives a sensitive measure of the electronic structure of these systems [25].

Therefore, in this thesis, we have investigated the electronic structure of SAQDs by examining the g-factors in these systems using the Zeeman effect. The dynamics of the transitions (in particular the relaxation mechanisms) have now been shown to be determined by the existence of excited states, and therefore the dynamics of various transitions was also of interest.

The hyperfine interaction is also predicted to be much greater in these systems because the electrons are strongly confined [27], therefore, it was decided that the nuclear spin system would be of great interest to examine. This was done by examination of the Hanle effect, which allows us to gauge information on the spin relaxation time and simultaneously, the presence of a nuclear field, and optically detected nuclear magnetic resonance (ODNMR), which allows us to examine the strength of the hyperfine interaction.

Bibliography

[1] H. Haug and S Koch, Quantum Theory of the Optical and Electronic Properties of Semiconductors, World Scientific, (1994)

[2] Various Authors, Scottish Summer School in Low Dimensional Semiconductor Structures – Physics and Applications, Institute of Physics, (1998)

[3] S. Hoogland et al, IEEE Photonics Technol. Lett., **12**, 1135 (2000)

[4] V.F. Puntes et al, Science,**291**, 2115 (2001)

[5] Various Authors, M.R.S. bulletin, February, 1998

[6] D.J. Guerrier and R.T. Harley, Appl. Phys. Lett. **70**, 1,739 (1997)

[7] D.J. Guerrier, PhD. Thesis, University of Southampton (1997)

[8] The Optics of Nanostructured Materials, K.Wang and A Balandin, Wiley, 2001

[9] W.J. Scaffer et al, Vac. Sci. Technol. B.,**1**, 688 (1983).

[10] K. Eberl P.M. Petroff and H. Demeester, Kluwer Dordrecht, NATO ASI series, (1995)

[11] Q.Xie, A. Kalburge, P. Chen and A. Madhukar, IEEE Photonics Technol. Lett., **8**, 965, (1996)

[12] M. Henini, S. Sanguinetti, S.C. Fortina, E. Grilli, M. Guzzi, G. Panzarini, L.C. Andreani, M.D. Upward, P. Moriaty, P.H. Beton, and L. Eaves, Phys. Rev. B, **57**, 6815 (1998)

[13] B.A Joyce, J.L. Sudijono, J.G. Belk, H. Yamaguchi, X.M. Zhang, H.T. Dobbs, A. Zangwill, D.D. Vvedensky, and T.S. Jones, Jpn J. Appl. Phys., Part 1 **36**, 4111 (1997)

[14] B.W. Wessels, J. Vac. Sci. Technol. B **15**, 1056 (1997)

[15] I. Daruka and A.L. Barabasi, Phys. Rev. Lett. **79**, 3708 (1997)

[16] Y. Chen and J. Washburn, Phys. Rev. Lett. **77**, 4046 (1996)

[17] C. Priester and M. Lannoo, Phys. Rev. Lett. **75**, 93 (1995)

[18] J.M. Jerard, J.B. Genin, J. Lefebvre, J.M. Moison, N. Lebouche and F. Barthe, J. Cryst. Growth **150**, 351 (1995)

[19] S. Fafard, D. Leonard, J.L. Merz, and P.M. Petroff, Appl. Phys. Lett. **65**,1388 (1994)

[20] L. Samuelson, S. Anand, N. Carlsson, P. Castrillo, K. Georgsson, D. Hessman, M.E. Pistol, C. Pryor, W. Seifert, L.R.Wallenberg, A. Carlsson, J-O. Bovin, S. Nomura, Y. Aoyagi, T. Sugano, K. Uchida, and N. Miura, Proceedings of the 23rd ICPS, edited by Matthias Scheffler and R. Zimmermann, World Scientific, NJ, p1269 (1996)

[21] J.M. Garcia, T. Mankad, P.O. Holtz, P.J. Wellman, and P.M. Petroff, Appl. Phys. Lett. **72**, 3172 (1998)

[22] M. Bayer, A. Kuther, F. Schäfer, J. P. Reithmaier, and A. Forchel, Phys. Rev. B, **60**, 8481 (1999)

[23] H. Benisty, C.M. Sotomayer-Torres, and C. Weisbuch, Phys .Rev. B, **44**, 10945 (1991)

[24] M. Grundmann, J. Christen, N.N. Ledentsov, J. Bohrer, D. Bimberg, S.S. Ruvimov, P.Werner, U. Richter, U. Goesele, J. Heydenreich, V.M. Ustinov, A Yu. Egorov, A.E. Zhukov, P.S. Kop'ev, and Zh. I. Alferov, Phys Rev Lett., **74**, 4043 (1995)

[25] G.P Flinn, R.T. Harley, M.J. Snelling, A.C. Tropper, and T.M. Kerr, Semicond. Sci. Technol., **5**, 533 (1990)

[26] Huaxiang Fu, Lin-Wang Wang, and Alex Zunger, Appl. Phys. Lett., **23**, 3433 (1997)

[27] D. Paget, G. Lampel, B. Sapoval, and V.I. Safarov, Phys. Rev. B, **15**, 780 (1976)

Chapter 2

The Theory of Optical Orientation in III-V Semiconductors

2.1 Introduction

This chapter provides an overview of optical orientation in III-V direct band semiconductor materials. We begin by introducing band-structure in III-V semiconductors, we then give a brief overview of the current theory on the electronic structure of SAQDs. An introduction to optical orientation is presented, a closer view of the electronic structure is subsequently presented, together with a brief introduction to nuclear structure. The chapter is brought to a close by a discussion on the coupling between the electron and the nuclear spin system, namely, the hyperfine interaction.

Inter-band optical absorption in III-V materials results in the generation of an electron in the conduction band, and a hole in the valence band [1]. The incident photon's angular momentum is distributed between the spin angular momenta of the electron (S_e) and hole (S_h) according to the selection rules associated with these transitions, and determined by the materials electronic structure.

The photo-excited state exists for a characteristic time (τ_r) called the recombination time, before the electron recombines with a hole. There are a number of different possible spin relaxation processes within the photo-excited state which have the effect of decreasing the spin orientation. Each process has a characteristic time which may be combined with other spin relaxation processes to produce the characteristic spin relaxation time (τ_s) for the material.

For a recombination time shorter than the spin relaxation time, there is a preferred spin orientation on recombination. Therefore recombination luminescence is partially polarised. It is necessary to distinguish between spin relaxation of free electrons and holes on the one hand and excitons on the other. In bulk GaAs and similar crystal structures, the hole has a fast spin relaxation time with respect to the electron [2] and this is also true in many quantum confined structures. Therefore the electron dictates the polarisation of recombination radiation. An exception to this rule is in n-type quantum wells. Because electrons and holes have opposite charge, the Coulomb attraction between the two carriers tends to form an electron-hole bound state or exciton.

The above is only valid in the situation where the hyperfine interaction between conduction electrons and lattice nuclei is not important. For III-V materials, the hyperfine interaction cannot be ignored and there may be extra optical effects due to the dynamic polarisation of the lattice nuclei. Two conditions for dynamic nuclear polarisation are the presence of an applied magnetic field, (which may be no more than a few ten's of gauss), and an optically pumping process that drives the electron spin system away from thermal equilibrium.

Nuclei polarised by photo-excited electrons then create an effective, or fictitious magnetic field, which acts back on the electron spin, and therefore modifies the band edge luminescence. This is termed optical orientation and has been used since the early 1960's, originally by Lampel [3].

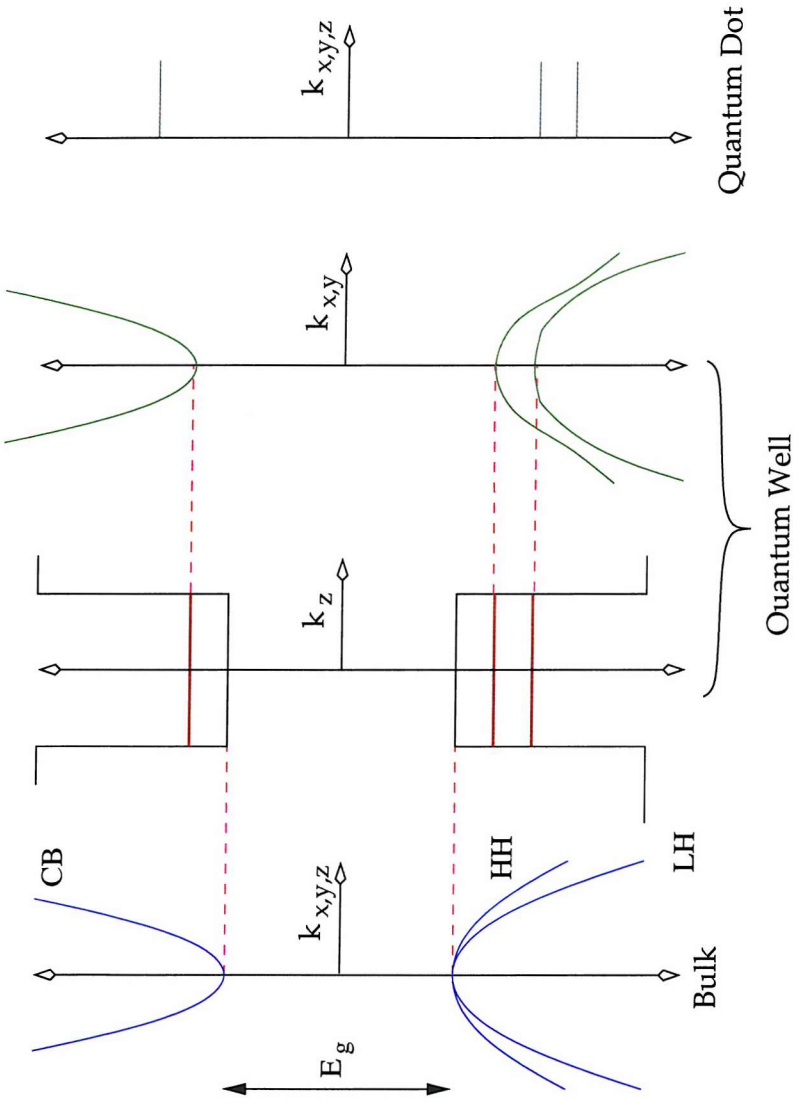

Figure 2.1: **Diagram showing the electronic structure of bulk (blue), quantum wells (brown and green), and quantum dots (cyan).**

2.2 Band Structure

2.2.1 Bulk Semiconductor Band Structure

The band-structure of a solid may be considered to be formed when isolated atoms are brought in close enough proximity to cause the electron wave-functions from nearest neighbour atoms to overlap [4]. The isolated levels form bands of allowed states separated by forbidden gaps. The most important of these gaps is the band gap (E_g) which separates valence and conduction bands and dictates the wavelength of edge luminescence in direct band semiconductors.

The samples in this chapter are all direct band semiconductors, (one in which the conduction band minimum and the valence band maximum correspond to k=0) [5]. A diagram showing bulk band structure is shown in the left hand diagram in figure 2.1.

The conduction band (CB) in zinc-blende crystals is formed from the first anti-bonding level and has an S atomic character. This is twice degenerate in spin with a z-axis projection of the total angular momentum of $S_z = \pm\frac{1}{2}$ (in units of $\hbar$). The conduction band has a parabolic dispersion close to the Γ point, deviating from this with increasing k due to interaction with the valence bands.

The valence bands are formed from the highest bonding levels and have a P atomic character. Band theory calculations predict three twice degenerate bands in the absence of spin-orbit coupling. These bands have been

named the heavy hole (HH), the light hole (LH), and the split off band (SO) (not shown in figure 2.1), with the heavy hole spin, $S_z^{HH} = \pm\frac{3}{2}$, the light hole spin, $S_z^{LH} = \pm\frac{1}{2}$ and the split off band spin, $S_z^{SO} = \pm\frac{1}{2}$.

Inclusion of the spin-orbit interaction in the band theory calculation causes the degeneracy of the SO valence band to be removed from the HH and LH bands, resulting in a splitting between these levels (Δ). Optical excitation from the split off band into the conduction band results in loss of optical orientation [6], however, as this is only important for excitation energies larger than $E_g + \Delta$, and we can therefore neglect the split off band in these experiments. Physically confining the electron and hole wave-functions to a specific region of space in III-V semiconductors has a drastic effect on the band-structure as discussed below.

2.2.2 Band structure in Confined Systems

One of the simplest forms of confinement potential is the quantum well. A quantum well is formed when two lattice matched semiconductors are sandwiched together that have different band-gap energies. The material with the narrower band-gap forms a potential well transverse to the layers and an illustration of its band-structure is given in the two central diagrams of figure 2.1.

If the material that forms the potential well is grown sufficiently thin, quantum confinement effects will be found in the form of a series of discrete energy levels analogous to the energy levels found in the solution to

one dimensional potential well. The accepted method used to calculate the energy levels in this system is the envelope function formalism [7].

The theory predicts at least one bound ground state and a series of excited states within the potential well. When the energy of successive excited states becomes larger than the conduction band offset, they become virtual states of the bulk. The energy of the ground state increases for decreasing well width.

The quantised electronic states are denoted in the usual energy level notation, n, where the ground state is denoted n=1, and successive higher states denoted with n greater than 1. It is important to point out that the conduction electrons are only confined in one direction and dispersion of electrons in k-space in the plane of the well is still exists.

The valence bands also undergo modification due to the confining potential. The most noticeable effect of the confinement being the lifting of the degeneracy of the zone centre between the heavy (HH), and light holes (LH) due to their different confinement energies. This is a result of their differing effective masses. One curious effect is that the HH along the z axis possesses a LH mass along the plane of the well and visa versa which leads to a crossing between the HH and LH at a particular value of k. However, the inclusion of higher $k \bullet p$ terms in the valence band Luttinger Hamiltonian gives an anti-crossing [8] behaviour as shown in figure 2.1.

Another type of confining potential is the self assembled quantum dot (SAQD). Strain is introduced into the system by growing a very thin layer of one semiconductor onto another semiconductor whose lattice constant

differs from the former. Initially, a highly strained layer forms on the surface called the wetting layer. As this layer grows, a critical thickness is reached and it becomes energetically more favourable for three dimensional structures to form [9] forming the quantum dots. Above this thickness the three dimensional growth stops and dislocations become more favourable. The quantum dots are then capped with the same material that was used to form the substrate. The electronic structure of SAQDs differs in a number of ways to that of the quantum well and therefore the next section is devoted to it.

2.3 Electronic Structure of Self Assembled Quantum Dots

For SAQDs realized via Stanski-Krastanov growth mode [10][11][12], strain is the driving force for the creation of the dots. SAQDs form by minimising the free energy when a lattice mismatched material is deposited on another material. The strain is accommodated entirely elastically without plastic deformation via structural defects (i.e. dislocations). The distortion to the lattice produced by the lattice mismatch between dot and substrate leads to an inherent difficulty in calculating the electronic structure of SAQDs.

Because of their highly strained nature, knowledge of the strain distribution within these systems is important to be able to calculate the electronic structure. However, strain modifies a number of other properties

as well, the longitudinal optical (LO) phonons are thought to play a significant role in the relaxation of carriers in these samples [13], (relaxation via LO phonon emission is severely restricted as soon as the average electron energy level spacing reaches a small fraction of the phonon energy range ($\hbar\omega_{LO} \approx 30$ meV)), and the LO phonon energy is modified by the presence of strain. Secondly, the confinement potential is also modified via strain and piezoelectric effects [14]. Therefore the optical properties of SAQDs are modified depending on the strain distribution experienced by the SAQDs.

To date, there are a number different methods used to calculate the strain distribution in SAQDs. For example, Priester calculated the strain distribution in un-capped SAQDs using the valence force field model [15] and Christiansen used finite element analysis [16] instead, to incorporate strain into the calculations. However, the most comprehensive study to date has been made by Grundmann et al [14]. They obtained the strain distribution in capped SAQDs using elastic strain continuum theory, by minimising the total strain energy of the quantum dot, barrier and wetting layer together for a slab, cylinder, sphere, and finally an InAs pyramid.

As other material structures became available, Grundmann then went on to apply the same theory to these structures, namely lens shaped $In_{0.5}$-$Ga_{0.5}As$ SAQDs embedded in GaAs, and $Al_xGa_{1-x}As$ SAQD structures also embedded in GaAs [17].

Grundmann found that the strain distribution is not very dependent on the size of quantum dot, but very dependent on its shape. This further compounds the difficulty of performing the calculation due to the fact that,

the capping layer tends to distort the pyramidal shape of the dots, and therefore would have a significant effect on the dot shape. Shear strain is also found to be significant at the pyramid edges, the inner part of the quantum dot contains nearly homogeneous hydrostatic (isotropic) strain, biaxial strain is transferred to the barrier and has a distinct minimum in the quantum dot itself.

From the strain distribution, Grundmann et al [9] calculated the modification to the LO phonon energy to be 32.1 meV for InAs SAQDs in agreement with their own experimental results [18]. From the strain distribution, it is possible to calculate the modification to the band structure.

Initially, this was done by a number of authors using the effective mass approximation, with extra $k \bullet p$ terms to obtain closer agreement with experiment. However, it was pointed out by Zunger [19], that this method was less accurate due to the fact that periodic boundary conditions may not be used when solving the Hamiltonian for the system because periodic boundary conditions may only be used in a periodic structure, and SAQDs form in a random pattern of dots across the wetting layer.

In order to find a way around this problem, Zunger used the tight binding model [20] to calculate the electronic structure for small quantum dots consisting of up to 10^6 atoms. However, the calculation increases rapidly in complexity with increasing number of atoms, and therefore can only be used for smaller SAQDs.

For larger quantum dots, Grundmann et al [9] found the following method: they calculated the energy of the conduction band as this depends on the

isotropic component of the strain only. In order to calculate the shift and splitting of the valence bands, they used a 6 x 6 Hamiltonian in the presence of the calculated strain distribution. The upper band was found to be the usual heavy hole (HH) $|\frac{3}{2}, \pm\frac{3}{2}>$ states, the other two bands were considered to be split too far apart from the valence band edge to effect the optical properties of the HH and therefore were ignored.

Grundmann found the edges of the pyramid to exist under shear strain, this induces a piezoelectric polarisation P, which creates fixed charges ρ_P:

$$\rho_P = -\nabla \bullet P \tag{2.1}$$

where

$$P_i = e_{ijk}\epsilon_{ij} \tag{2.2}$$

and e_{ijk} is the piezoelectric moduli. The piezoelectric charge reside close to the pyramid's edges but mainly in the barrier, and have opposite signs for adjacent edges. It was found that the potential due to the piezoelectric potential has a very complicated geometry and scales linearly with dot size. The inclusion of the piezoelectric potential into the calculation shifts the level energies by less than 1 meV however so therefore was ignored. The Hamiltonian for the electron-hole pair is [14]:

$$H(r_e, r_h) = H_{e,kin}(r_e) + V_e(r_e) + H_{h,kin}(r_h) + V_h(r_h) + H_c(r_e, r_h) \tag{2.3}$$

where $H(r_e, r_h)$ has been separated into $H_{e,kin}(r_e)$, the Hamiltonian for the

electron, $V_e(r_e)$ is the strain induced electronic potential, $H_{h,kin}(r_h)$ is the hole Hamiltonian, $V_h(r_h)$ is the strain induced hole potential, and $H_c(r_e, r_h)$ is the coupling between the electron and hole. These components are given as:

$$H_{e,kin}(r_e) = \frac{\hbar^2}{2} \sum_{i=x,y,z} \nabla_i \frac{1}{m_e(r_e)} \nabla_i \tag{2.4}$$

where m_e is the mass of the electron at co-ordinate r_e.

$$H_{h,kin}(r_h) = \frac{\hbar^2}{2} \left(\sum_{i=x,y} \nabla_i \frac{1}{m_{h,\perp}(r_h)} \nabla_i + \nabla_z \frac{1}{m_{h,\parallel}(r_h)} \nabla_z \right) \tag{2.5}$$

where m_h is the hole mass at r_h perpendicular ($\perp$), i.e. the x,y direction, and parallel ($\parallel$) to the growth direction, and:

$$H_c(r_e, r_h) = \frac{-e^2}{4\pi\epsilon_r\epsilon_o} \frac{1}{|r_e - r_h|} \tag{2.6}$$

is the Hamiltonian of the Coulomb interaction, here e is the electron charge, ϵ_r the relative permitivity in the SAQDs, and ϵ_o is the permitivity of free space.

Because the electrons are in the strong confinement regime [21], the confinement energy is the dominating part of the total carrier energy. Therefore the Coulomb interaction is also added as a perturbation. The results for the energy diagram are shown in figure 2.2 for InAs/GaAs SAQDs, with a base length of 12 nm and height 3nm.

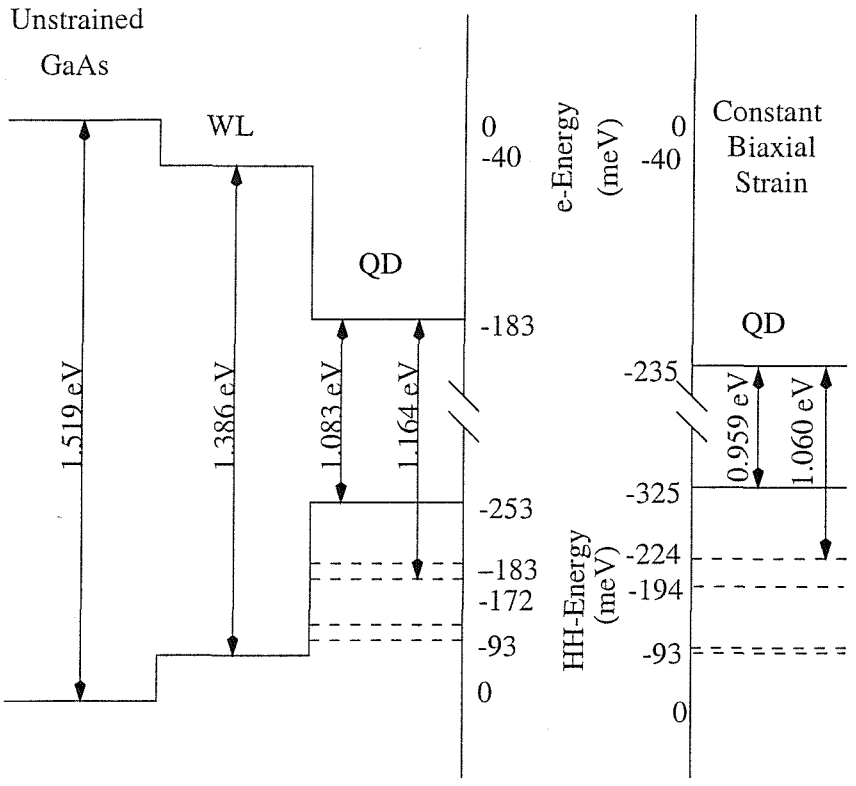

Figure 2.2: **Diagram showing the calculated InAs/GaAs SAQD energy level scheme for a base length of 12nm [14]. The left hand side show the energy level for bulk GaAs, the wetting layer (WL), the quantum dot (QD), the right hand side the energy levels are shown for constant biaxial strain. The zeros are taken at the unstrained bulk GaAs conduction and valence bands. The dashed lines represent the heavy hole energy levels.**

The calculated wave-functions found only one electron hole state, higher states hybridizing with those of the wetting layer. These are shown in figure 2.2 as dotted lines.

The right hand side of figure 2.2 shows the calculated energies with the assumption that the strain is constant within the quantum dot and wetting layer with the same value. As shown, this has a significant change in conduction and valence energy levels. However experimentally, InAs dots appear to show photoluminescence features closer to the left hand side of the figure and therefore Grundmann et al [9] showed that strain is not constant in these structures.

Grundmann et al [9] also showed that the spherical approximation (a sphere of radius r whose volume is equal to the volume of the pyramid), produced inaccurate hole energies, and that the "adiabatic approximation", (i.e. solving the Schrödinger equation in one dimension, and subsequently solving the two dimensional in plane Schrödinger equation), tends to produce inaccuracies in both electron and hole energies.

Experimentally, the phonon bottleneck has been found to be suppressed in SAQD samples that have not been allowed to anneal after growth [17] [22]. This is because the dominant carrier relaxation mechanisms in $In_{0.5}Ga_{0.5}As$ SAQDs are multiple phonon relaxation processes at low carrier densities [18] [23] [24], and Auger processes at high carrier excitation density [23]. One other interesting suggestion was that carrier relaxation is due to tunnelling through deep levels from a trap and coupled to the SAQD [25].

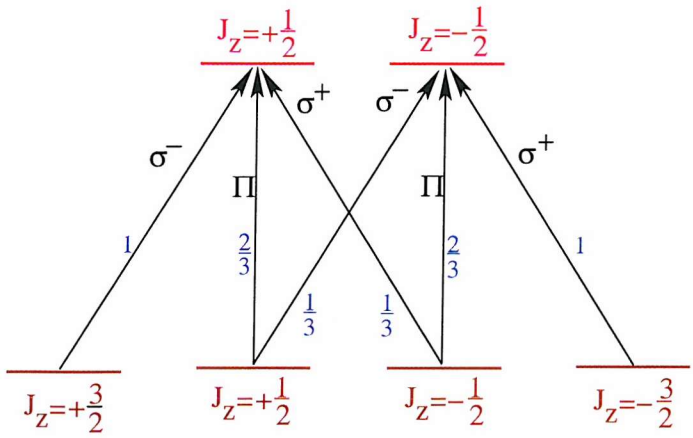

Figure 2.3: **Diagram showing the bulk optical transition selection rules and transition probabilities for band edge optical excitation in III-V semiconductors.**

2.4 Optical Orientation and Optical Transitions

The absorption of sufficiently energetic polarised photons creates electron hole pairs. The electrons and holes have predetermined spin orientations according to the selection rules shown in figure 2.3 for bulk and 2.4 for confined systems. We can therefore define the electron polarisation P, as the difference between the population of spin up electrons, $(N_{S_\uparrow})$, to the population of spin down electrons, $(N_{S_\downarrow})$, normalised to the total population of spin up and down electrons in the conduction band, $(N_{S_\uparrow} + N_{S_\downarrow})$ as

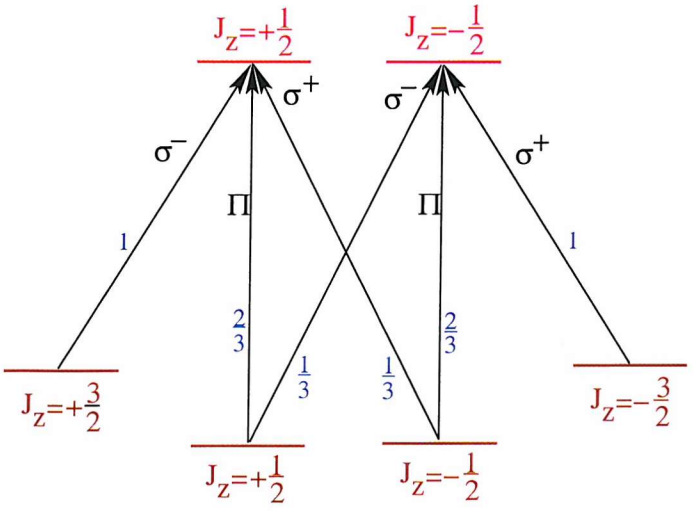

Figure 2.4: **The Effect of Confinement on the Optical Transition Selection Rules**

follows:

$$P = \frac{N_{S_\uparrow} - N_{S_\downarrow}}{N_{S_\uparrow} + N_{S_\downarrow}} \tag{2.7}$$

Therefore, pumping a bulk semiconductor with σ^+ polarised radiation will produce a fixed ratio of $J_z = -\frac{1}{2}$ to $J_z = +\frac{1}{2}$ electrons of 3:1. Equally the population of the valence band will consist predominantly of $-\frac{3}{2}$ heavy holes. From equation 2.7, we find the maximum electron polarisation will be 0.5.

However, recombination is covered by the same rules as excitation [26] and we may define the polarisation of luminescence as:

$$P_l = \frac{I_{\sigma+} - I_{\sigma-}}{I_{\sigma+} + I_{\sigma-}} \tag{2.8}$$

where $I_{\sigma+}$ and $I_{\sigma-}$ is the intensity left and right circularly polarised light. Assuming no relaxation of carrier spin, we would obtain a maximum degree of circular luminescence of 0.25. It should be noted that spin relaxation plays an important role in the degree of circular polarisation seen at recombination and will be discussed in the next section.

2.5 Spin Relaxation of Carriers

Excited carriers tend to undergo spin relaxation before recombination. Thus the spin orientation created at the moment of excitation is likely to be reduced. In bulk, hole spin relaxation is very fast due to mixing of LH and HH populations at $k = 0$. The lifting of the degeneracy of the LH and HH in confined systems tends to increase the hole spin relaxation time.

Under continuous wave (CW) excitation, dynamic equilibrium is reached between excitation and recombination of carriers. The resulting steady state conduction spin polarisation of electrons S_0 [3] may be defined as:

$$S_0 = S_i \frac{1}{1 + \frac{\tau_r}{\tau_s}} \tag{2.9}$$

where S_i is the initial spin polarisation and is 0.25 for bulk GaAs and similar crystals, τ_s and τ_r are the electron spin relaxation time and recombination times respectively.

2.6 The Electronic Spin System

In the presence of a magnetic field, the spin of an electron tends to precess about that field direction. This phenomenon is called Larmor precession. In order to describe Larmor precession we may make use of the Hamiltonian describing an electron in a magnetic field:

$$H = \frac{\mu_B g^*}{2} \sigma \bullet B \tag{2.10}$$

where μ_B is the Bohr magneton, g^* is the electron g factor, σ is the electron angular momentum, and B is the magnetic field. We define the magnetic field to be in the growth direction of the SAQDs and parallel to the z direction. Solution of this equation describes a spin precession about the z axis with angular frequency Ω, the Larmor frequency:

$$\Omega = \frac{\mu_B g^* B}{\hbar} \tag{2.11}$$

For a static magnetic field in time t, the spin is modulated by a factor $\cos(\Omega t)$. There is also the reduction due to spin relaxation. Therefore the spin orientation is further reduced by a factor $\exp(-\frac{t}{\tau_s})$. So after time t, the final value of spin orientation S_z is:

$$S_z = S_o e^{-\frac{t}{\tau_s}} \cos(\Omega t) \tag{2.12}$$

However, electrons will only exist in the conduction band for a characteristic time, before they recombine. We define the probability of an electron

having a lifetime t as $W(t)$:

$$W(t) = \frac{1}{\tau_r} e^{-\frac{t}{\tau_r}} \tag{2.13}$$

The average electron spin orientation may be obtained by combining the above with S_z and integrating with respect to t [27]:

$$S_z(B) = S_i \int_0^\infty W(t) e^{-\frac{t}{\tau_s}} \cos(\Omega t) dt \tag{2.14}$$

which leads to a Lorentzian dependence of electron spin polarisation with magnetic field. This is the transverse Hanle effect:

$$S_z(B) = \frac{S_o}{1 + (\Omega T)^2} \tag{2.15}$$

where $\frac{1}{T} = \frac{1}{\tau_s} + \frac{1}{\tau_r}$. The effective electronic g factor is now obtainable if we make a measurement at $S_z(B) = \frac{1}{2} S_o$, i.e. the measurement of the half width at half height $\Delta B_{\frac{1}{2}}$ of the Lorentzian and using [28]:

$$\Delta B_{\frac{1}{2}} = \frac{\hbar}{\mu_B g^* T} \tag{2.16}$$

which is obtained by rearrangement of equation 2.15. The above can only be used to find g^* if both τ_r and τ_s are known.

Nuclear Properties of Samples			
Element	Spin, I	Abundance, ρ (%)	Magnetic Moment, μ ($MHzT^{-1}$)
^{69}Ga	$\frac{3}{2}$	60.4	10.22
^{71}Ga	$\frac{3}{2}$	39.6	12.96
^{113}In	$\frac{9}{2}$	3.28	9.31
^{115}In	$\frac{9}{2}$	95.72	9.33
^{75}As	$\frac{3}{2}$	100	7.29

Table 2.1: **Table giving the spin, natural abundance, and magnetic moment of the nuclear species found in the SAQD samples studied. All data obtained from reference [29].**

2.7 The Nuclear Spin System

Optical orientation in semiconductors give rise to a number of strong effects that have no analogy under optical pumping of free atoms. This is due to the coupling between the electron and nuclear spin systems through the hyperfine interaction.

The nuclear spin system of an atom α is characterised by the abundance (ρ_α), nuclear spin (I_α) and the gyro-magnetic ratio (γ_α). The hyperfine interaction is also required for full characterisation of the nuclear spin system in lattices of III-V semiconductors.

Nuclear orientation effects are only seen in nuclei with a spin greater than a $\frac{1}{2}$. All nuclei in the samples studied for this thesis have non-zero nuclear spin (I) as listed in table 2.1 and therefore nuclear effects are expected to

play a part in all optical orientation experiments.

Optical orientation of electrons affects the nuclear spin system by orienting the nuclear spin in the same direction via the hyperfine interaction. A secondary effect is that due to the nature of the transfer of angular momenta from electronic to nuclear spin system, electron spin tends to relax at the same time.

This mechanism is reversible and the polarised nuclei also act back on the electron spin system. However, the direction and magnitude of the hyperfine interaction that acts back on the electrons is affected by the establishment of equilibrium between the nuclear spins in the nuclear spin system.

This equilibrium is characterised by two different characteristic times, T_1, the longitudinal relaxation time and T_2, the transverse relaxation time. These two characteristic times lead to the concept of a nuclear spin temperature which is actually a measure of the nuclear spin-spin interactions [30].

For a nucleus with a magnetic moment (μ), the spin of the nuclear species (I) is related to its intrinsic spin by:

$$\mu = \gamma I \hbar \tag{2.17}$$

where γ is the nuclear gyro-magnetic ratio. In the absence of any external perturbation, the $2I(I+1)$ nuclear states in a given species are degenerate in spin. This degeneracy may be removed by either the application of an

external magnetic field or an electric field gradient. Electric field gradients are caused by the exchange of one type of atom in a crystal lattice, with another type. Further information is given later in the ODNMR chapter where it is shown that electric field gradients are important for nuclear quadrapole splitting.

Transitions between nuclear levels occur by energy exchanges with the fixed lattice, this spin-lattice relaxation is not in general very fast, having a relaxation time of seconds to days depending on the lattice temperature [32] [33]. We define the spin-lattice relaxation time in terms of the relaxation of the level populations ($N(t)$), towards its thermal equilibrium value as T_1:

$$\frac{dN}{dt} = \frac{N(t=0) - N(t)}{T_1} \tag{2.18}$$

or equivalently

$$N(t) = N_0 \left(1 - e^{-\frac{t}{T_1}}\right) \tag{2.19}$$

The second relaxation time describes the spin-spin transitions. Transitions which do not occur by thermal exchanges with the fixed lattice must conserve the total energy of the nuclear system, and the characteristic time for these transitions is called the transverse relaxation time T_2. The time of establishment of equilibrium is given by [30]:

$$T_2 = \frac{1}{\gamma B_L} \tag{2.20}$$

where B_L is a measure of the local nuclear fields and is of the order 1 Gauss [34].

An order of magnitude estimate of T_2 is given in reference [35]. Paget estimated T_2 assuming the local nuclear fields could be approximated to $B_L \approx \frac{\gamma\hbar}{r^3}$ with r the inter-atomic spacing. Using this approximation T_2 becomes of the order 100 μs.

Therefore the spin system of the nuclei is effectively isolated from the lattice because the longitudinal relaxation time is very much longer than the transverse relaxation time. In other words the nuclear spin system predominantly relaxes via spin-spin transitions. The difference between T_1 and T_2 lead directly to the concept of a nuclear spin temperature Θ. This is useful to describe the degree of orientation of spins in the nuclear spin system when the nuclear spin system is not in equilibrium with the lattice. In general the nuclear spin temperature is different from the lattice temperature due to these differing relaxation times [1].

When an external static magnetic field (B_{ext}) is large enough to overcome the local nuclear fields, the nuclear spins tend to align themselves parallel to the external magnetic field. This is because the nuclear spin system interacts by the simultaneous exchange of spin angular momenta between states. However, for applied fields lower or of the same order as the local fields, the nuclear spin states overlap in energy and the average nuclear spin $< I >$ is zero.

By assuming the Boltzmann distribution in an equally spaced set of levels, we can sum over all spin states to obtain the average nuclear spin $< I >$

[36]:

$$< I >= \frac{\hbar\gamma}{3} I(I+1) \frac{B_{ext}}{k_B \Theta} \tag{2.21}$$

where k_B is Boltzmann's constant and Θ is the nuclear spin temperature. The value of the spin temperature is in general different to the lattice temperature [37]:

$$\frac{1}{\Theta} = \frac{1}{\Theta_o} \frac{B_{ext}}{B_{ext}^2 + \xi B_L^2} \tag{2.22}$$

where Θ_o depends mainly on the hyperfine coupling with the electronic spin system. The number ξ is related to the nuclear spin-spin interactions and is generally of the order unity [33]. Equation 2.22 shows that the nuclei cannot become polarised if the local nuclear fields are of the same order, or greater than the external magnetic field. Combining equations 2.22 and 2.21 gives a formula for the average nuclear field:

$$< I >= \hbar\gamma \frac{I(I+1)}{3} \frac{1}{k_B \Theta_o} \frac{B_{ext}^2}{B_{ext}^2 + \xi B_L^2} \hat{\mathbf{u}} \tag{2.23}$$

where $\hat{\mathbf{u}}$ is a unit vector pointing in the same direction as the external magnetic field as experienced by the nuclei.

2.8 The Hyperfine Interaction

The interaction of an electron of spin S and a nucleus of spin I is given by the Hamiltonian for the contact interaction as [38]:

$$H_F = A\mathbf{I} \bullet \mathbf{S} = AIS\cos(\theta) \tag{2.24}$$

where θ is the angle between the average nuclear spin $< I >$ and the average electron spin $< S >$ and:

$$A = \frac{16\pi}{3}\mu_B\gamma\hbar|\psi(0)|^2 \tag{2.25}$$

where $|\psi(0)|^2$ is the electron probability density at the nucleus and μ_B is the Bohr magneton.

The strength of the interaction for conduction electrons increases significantly due to the $|\psi(0)|^2$ term. Therefore we find a stronger interaction for electrons in an s-orbital due to their large wave-function density at the nucleus, and localised electrons. Thus for SAQDs we expected nuclear effects to play a significant role in the photoluminescence spectrum under optical orientation.

For electrons with orbital angular momenta greater than zero, ($l > 0$), we find there is a contribution to the hyperfine interaction due to the non-zero value of the electron wave-function at the nucleus, however, the effect is quite small and may for all intent and purposes be considered a second or-

der effect. We shall separate the discussion into static and dynamic effects for simplification.

2.8.1 Dynamic Effects of the Hyperfine Interaction

Figure 2.5 illustrates the feedback mechanism through which the electronic and nuclear spin systems influence each other. The interaction is dynamic due to the existence of various relaxation mechanisms not the least of which is the hyperfine interaction itself, (the hyperfine interaction tends to relax the electron spins and orient the nuclear spins under optical pumping).

The ellipses represent the two spin systems interacting dynamically through the hyperfine interaction. The electronic spin system is oriented through optical pumping, loss of spin orientation of the electrons being due to the hyperfine interaction and spin relaxation. The dynamic effects of this interaction are manifest as rapid exchanges of angular momenta between the conduction electrons and the lattice nuclei. This process results in the simultaneous reversal of spin of both participants.

The nuclear spin system is then oriented by the exchange of angular momenta with the electronic spin system due to the existence of a nuclear spin temperature. The nuclear spin system may relax by lattice relaxation or unpolarised holes. Due to the double sided nature of the hyperfine interaction, the electron spins tend to feel an effective magnetic field due to the presence of the oriented lattice nuclei spins, therefore providing a

feedback mechanism in the coupling system.

Assuming the spin-lattice relaxation of the nuclei is small, the mean nuclear spin $< I >$ may be given as [34]:

$$< I >= \frac{I(I+1)}{S(S+1)}(< S > - < S' >) \tag{2.26}$$

where $< S >$ is the mean electron spin in the presence of optical pumping, $< S' >$ is the mean electron spin in the absence of optical pumping, (and in most cases is zero) and I is the nuclear spin. Due to a number of relaxation mechanisms, the average nuclear spin is reduced by a factor f:

$$f = \frac{T_{other}}{T_{other} + T_{hyperfine}} \tag{2.27}$$

where $T_{hyperfine}$ is the relaxation time due to the hyperfine interaction and T_{other} is the characteristic time for nuclear spin-lattice relaxation. This may be affected by unpolarised holes and the nuclear quadrapole interaction to name a few mechanisms.

Because the direct exchange of angular momentum quanta from electrons to nuclei, the nuclei spin tend to align parallel to the electron spins, and parallel to the incident light direction. However, in the absence of an external field greater than the local nuclear fields, the nuclei spin are quickly disoriented.

For oblique external magnetic fields greater than the local nuclear fields, the nuclear spin aligns parallel to the external magnetic field rather than

the average electron spin direction, this is due to the existence of a nuclear spin temperature. However, the exchange of angular momenta continues and so does the feedback mechanism, therefore the resulting polarisation state to the photoluminescence may appear very complex.

2.8.2 Static Effects of the Hyperfine Interaction

The conduction electron spin system influences the nuclei spin system via the hyperfine interaction and visa versa. This influence is more easily visualised by expressing it in terms of an effective internal magnetic field. In general the effective field experienced by the electron spins is large and that experienced by the nuclear spins is small.

A nucleus i at co-ordinates r will experience an effective magnetic field, B_e^i due to the presence of electrons in the vicinity of the nucleus. This field is mediated through the hyperfine interaction [39]:

$$B_e^i = -\frac{16\pi}{3}\mu_B \sum_q S_q |\psi_q(r_i)|^2 \tag{2.28}$$

where we sum over all occupied conduction electron states, q for the particular nucleus, i. This field may be detected as a shift in the nuclear magnetic resonance (NMR) frequency and is named the Knight shift [40]. Our experimental apparatus is not sensitive enough to be able to resolve this shift.

The hyperfine interaction also couples the electronic spin system to the nu-

clear spin system, and therefore the electrons also experience an effective magnetic field. The magnitude of the effective magnetic field experienced by an electron due to the presence of surrounding polarised nuclei is given as [39]:

$$B_N^q = -\frac{16\pi}{3}\frac{\hbar}{g^*}\sum_i \gamma_i I_i |\psi_q(r_i)|^2 \tag{2.29}$$

where the electron is in orbital state ψ_q and, if the nuclei are uniformly polarised this field may be expressed as:

$$B_N = b_N < I > \tag{2.30}$$

where

$$b_N = \frac{16\pi}{3}\frac{\hbar}{g^*}\sum_i \gamma_i |\psi_q(r_i)|^2 \tag{2.31}$$

Note that b_N is dependent on the conduction electron g factor (g^*).

So the magnitude of the nuclear field depends on the effective electron g factor g^* of the conduction electrons, the nuclear polarisation (which depends on the magnitude and relative orientation of the electron polarisation) and any nuclear relaxation processes other than the hyperfine interaction itself. This dependence may be summarised in the following expression for nuclear field obtained using equations 2.21, 2.26, 2.27 and 2.30:

$$B_N^{'} = f b_N \frac{I(I+1)}{S(S+1)}\frac{B_{ext}^2}{B_{ext}^2 + \xi B_L^2} < S > \cos(\theta) \tag{2.32}$$

2.9 The Hanle Effect

The transverse Hanle effect has already been discussed in terms of the electron spin system in section 2.6. Here we discuss the Hanle effect in the presence of a nuclear field, or the so called oblique Hanle effect.

Equation 2.32 shows that the existence of a nuclear field is dependent on the contact of optically oriented electrons with nuclei. This is further dependent on the external magnetic field being strong enough to stop the randomisation of nuclear spins under local nuclear fields and the average spin orientation being at an angle other than perpendicular to the external magnetic field. The interaction strength is therefore dependent on the electron localisation in the sample and we therefore expect nuclear effects to be strongly enhanced in SAQDs.

The transverse Hanle curve is significantly modified in the presence of a nuclear field. This is because the total field experienced by the electron spins is the vector sum of both the external magnetic field, and the internal nuclear field.

In such a system, the de-polarisation of optically orientated electrons is radically altered: For external magnetic fields lower than the local nuclear

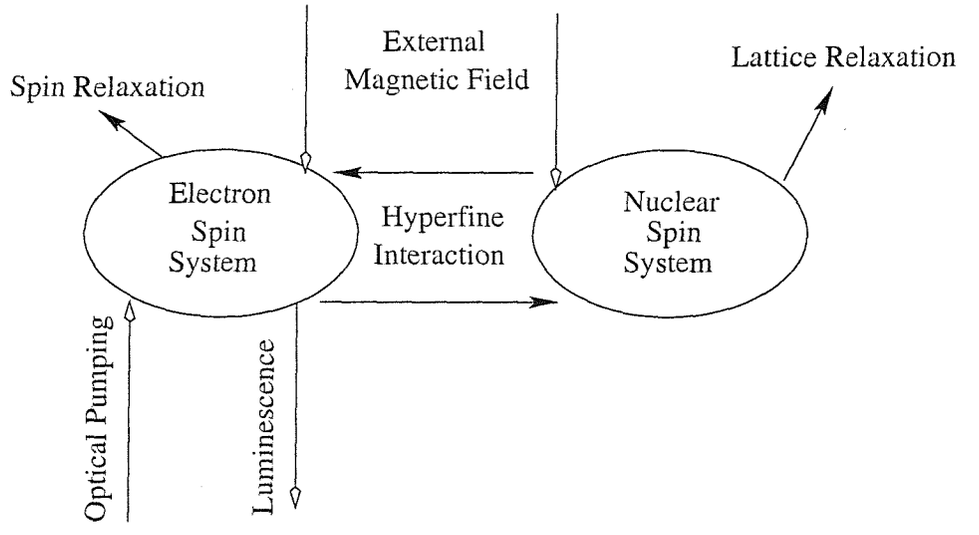

Figure 2.5: **Schematic diagram showing the coupling of the nuclear spin system with the electronic spin system of a semiconductor. This coupling is mediated via the hyperfine interaction and feeds back on itself. Optical pumping produces an electronic spin alignment, the nuclear spin system then experiences an effective magnetic field that tends to align the nuclei spin. Feedback from the orientated nuclei tend to the influence the electronic spin system through the hyperfine interaction due to the existence of a spin temperature. The electronic spin system may loose polarisation through recombination and spin relaxation, the nuclei via lattice relaxation or interaction with unpolarised holes.**

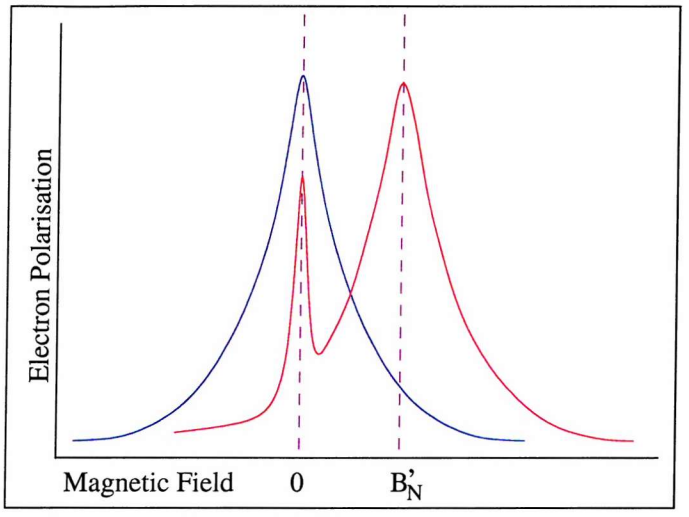

Figure 2.6: **The Hanle effect. The blue curve represents the transverse Hanle effect, i.e. with the incident light, (and therefore the average electron spin), perpendicular to the external magnetic field. Tilting the sample causes the angle between the external magnetic field and the electron polarisation to become less than 90^o, this allows the existence of a nuclear field and we obtain the the oblique Hanle effect. Compensation of the external magnetic field by the nuclear field is seen as a shift in the Lorentzian maximum, the spike at zero magnetic field is due to the randomising nature of the local nuclear fields.**

fields we find nuclear orientation insignificant and therefore we obtain a spike close to zero magnetic field. For external magnetic fields greater than the local nuclear fields, the Lorentzian maximum is displaced from zero field due to compensation of the external field by the nuclear field. This has been pictorially represented in figure 2.6

The equation of motion for an electron in the presence of a magnetic field [41], taking into account spin relaxation, generation of photoexcited electrons and recombination is:

$$\frac{dS}{dt} = \Omega \times S - \frac{S}{\tau_s} - \frac{S - S_0}{\tau_r} \tag{2.33}$$

where

$$\Omega = \frac{\mu_B g^* B_T}{\hbar} \tag{2.34}$$

is the Larmor spin vector of the conduction electrons and S is the average spin of the electron. The vector lies along vectorial sum of the external magnetic field and the nuclear field, here represented by B_T.

The solution of the equation of motion allows us to obtain the variation of electron spin as a function of applied magnetic field along the direction of excitation.

Therefore we define the z axis in the growth direction of our samples and parallel to the incident light and, define θ to be the angle between the external field and the incident light, (and therefore the average electron spin),

then, from the above equation we get the equilibrium electron polarisation component along the z axis as:

$$S_z(B) = S_0 \left[\frac{\sin^2(\theta)}{1 + (\Omega T)^2} + \cos^2(\theta) \right] \tag{2.35}$$

The shape of the oblique Hanle curve yields a number of important pieces of information, the first of these is also the most obvious, it signifies the existence of nuclear orientation.

Secondly, examination of equations 2.30, and 2.31 show that it is possible to obtain the sign of the electron g factor. This is because the direction of the nuclear field relative to the external field depends on the sign of the electronic g factor.

The third piece of information has to do with the secondary peak indicated in figure 2.6 as B_N', the external magnetic field has to overcome the local nuclear fields giving the secondary peak. The secondary peak maxima is the point where the external magnetic field compensates exactly for the local nuclear fields. Therefore the appearance of the displaced Lorentzian curve gives a measure of the local nuclear field strength.

This method was very successful in confirming g factor measurements using conduction electron spin resonance [42] and in identifying changes in sign of the electron g factor in quantum wells [28].

2.10 Nuclear Magnetic Resonance

A description of optically detected nuclear magnetic resonance (ODNMR) will be delayed until chapter 6. Here we introduce conventional NMR as a prelude to the ODNMR measurements.

Bloch [43] and Purcell [44] both independently developed the conventional NMR technique. A static magnetic field is applied to the sample of interest in order to split the nuclear spin levels. The application of an oscillating radio frequency field perpendicular to the static magnetic field is then used to detect NMR.

This works by inducing transitions between nuclear levels when the energy of the oscillating radio frequency wave ($\hbar\omega$, where ω is the frequency of the oscillating field) becomes comparable to the difference between the nuclear spin levels ($\hbar\gamma B_{ext}$). Figure 6.2 illustrates this pictorially.

Detection of these transitions relies on the radio frequency circuit supplying the oscillating wave. Radio frequency quanta are absorbed by the nuclear spin system and therefore a resonance circuit may detect this change in the circuit's Q factor. One of the largest disadvantages with this method is the large number of nuclei ($> 10^{18}$ [45]) that have to absorb the radio frequency photons before any appreciable effect is seen.

Bibliography

[1] F. Meier and B. P. Zacharchenya, Optical Orientation, North Holland, (1984) (Chapter 3, Page 78)

[2] F. Meier and B. P. Zakhaechenya, Optical Orientation, North Holland, (1984) (Chapter 3, Pages 125–126)

[3] G. Lampel, Phys Rev Lett., **20**, 491 (1968)

[4] H. Haug and S. Koch, Quantum Theory of the Optical and Electronic Properties of Semiconductors, World Scientific, (1994) (Chapter 3, Page 38-44)

[5] C. Kittel, Introduction to Solid State Physics, 7^{th} Edition, Wiley International, (1996) (Chapter 4, Page 100)

[6] M. I. D'yakanov and V. I. Perel, Optical Orientaion, North Holland, (1984) (Ch2, p29)

[7] Ed. E. E. Mendez and K. von Klitzing, Physics and Applications of Quantum Wells and Superlattices, NATO ASI Series B, Physics Vol 170 (Plenum Press 1987)

[8] G. D. Sanders and Y. C. Chang, Phys Rev B **31**, 6892 (1984)

[9] M. Grundmann, J. Christen, N. N. Ledentsov, J. Bohrer, D. Bimberg, S. S. Ruvimov, P.Werner, U. Richter, U. Goesele, J. Heydenreich, V. M. Ustinov, A Yu. Egorov, A. E. Zhukov, P. S. Kop'ev, and Zh. I. Alferov, Phys Rev Lett., **74**, 4043 (1995)

[10] D. Leonard, M. Krishnamurty, C. M. Reaves, S. P. DenBaars, and P. M. Petroff, Appl. Phys. Lett. **63**, 3203 (1993)

[11] J. M. Moison, F. Houzay, F. Barthe, L. Leprince, E. André, and O. Vatel, Appl. Phys. Lett. **64**, 196 (1994)

[12] N. N. Ledentsov, M. Grundmann, N. Kirstaedter, J. Christen, R. Heitz, J. Böhrer, F. Heinrichsdorff, D. Bimberg, S. Ruvimov, P. Werner, U. Richter, U. Gösele, J. Heydenreich, V. M. Ustinov, A. Yu. Egorov, M. V. Maximov, P.S. Kop'ev, and Zh. I. Alferov, Proceedings of the 22^{nd} International Conference on the Physics of Semiconductors, edited by D.J. Lockwood, World Scientific, Singapore, (1995)

[13] H. Benisty, C. M. Sotomayer-Torrès, and C. Weisbuch, Phys. Rev. B. **44**, 10945 (1991)

[14] M. Grundmann, O. Stier, and D. Bimberg, Phys. Rev. B **52**, 11969 (1995)

[15] C. Priester, I. Lefebre, G. Allan, and 0. Lannoo, Mechanisms of Thin Film Evolution, MRS Symposia Proceedings No. 137 (Materials Research Society, Pittsburgh, 1994), Page 131

[16] S. Christiansen, M. Albrecht, H. P. Strunk, and H. J. Maier, Appl. Phys. Lett. **64**, 3617 (1994)

[17] B. Ohnesorge, M. Albrecht, J, Oshinowo, and A. Forshel, Phys. Rev. B. **54**, 11532 (1996)

[18] R. Heitz, M. Grundmann, N. N. Ledentsov, L. Eckey, M. Veit, D. Bimberg, V. M. Ustinov, A. Yu. Egorov, A. E. Zhurkov, P. S. Kop'ev, and Zh. I. Alferov, Appl. Phys. Lett. **68**, 361 (1996)

[19] H. Fu and A. Zunger, Phys. Rev. B, **55**, 1642 (1997)

[20] C. Kittel, Introduction to Solid State Physics, 7^{th} Edition, Wiley International, (1996) (Chapter 9, Page 245)

[21] Al. L. Efros and A.L. Efros, Sov. Phys. Semicond. **16**, 772 (1982)

[22] T. S. Sosnowski, and T. B. Norris, Phys. Rev. B **57**, 9423 (1998)

[23] U. Brockelmann, and T. Egeler, Phys. Rev. B **46**, 15 574 (1992)

[24] M. Vollmer, E. J. Mayer, W. W. Rühle, A. Kurtenbach and K. Eberl, Phys. Rev. B **54**, 17292 (1996)

[25] P. C. Sercel, Phys. Rev. B, **51**, 14532 (1995)

[26] F. Meier and B. P. Zakhaechenya, Optical Orientation, North Holland, (1984) (Chapter 2, Page 23)

[27] M. I. D'yakanov and V. I. Perel, Optical Orientation, North Holland, (1984), (Chaper 2, Page 40)

[28] M. J. Snelling, G. P. Flinn, A. S. Plaut, R. T. Harley, A. C. Tropper, R. C. Eccleston, and C. C. Phillips, Phys. Rev. B, **44**, 11345 (1991)

[29] C. R. Weast, Handbook of Chemistry and Physics, 69^{th} Edition, CRC press, (1988)

[30] M. Goldman, Spin Temperature and Nuclear Magnetic Resonance in Solids, Clarendon Press, (1970)

[31] S. Gasiorowicz, Quantum Physics, Wiley International, (1974) (Chapter 14, Page 236)

[32] F. Meier and B. P. Zakharchenya, Optical Orientation, North Holland, (1984) (Chapter 2, Page 50)

[33] D. Paget, Phys Rev B, **25**, 4444 (1982)

[34] D. Paget, G. Lampel, B. Sapoval, and V.I. Safarov, Phys. Rev B, **15**, 5780 (1977)

[35] D. Paget, Phys Rev B, **24**, 3776 (1981)

[36] A. Abragam, Principles of Nuclear magnetism, Oxford Scientific Publishing, (1961) (Chapter 1 page 2)

[37] D. Paget, Optical Orientation, North Holland, (1984)

[38] A. Abragam, Principles of Nuclear magnetism, Oxford Scientific Publishing, (1961) (Chapter 6 page 160)

[39] F. Meier and B. P. Zakharchenya, Optical Orientation, North Holland, (1984) (Chapter 9, page 389)

[40] C. P. Slichter, Principles of Magnetic Resonance, Harper and Row, (1963) (Chapter 4, page 89)

[41] M. I. D'yakanov and V. I. Perel, Optical Orientation, North Holland, (1984), (Chaper 2, Page 62)

[42] C. Eeisbuch and C. Hermann, Phys. Rev. B, **15**, 816 (1977)

[43] F. Bloch, W. W. Hansen, and M. Packard, Phys. Rev., **70**, 474 (1946)

[44] E. M. Purcell, H.C. Torrey, and R.V. Pound, Phys. Rev., **69**, 37 (1946)

[45] A. Abragam, Principles of Nuclear magnetism, Oxford Scientific Publishing, (1961) (Chapter 1, page 3)

Chapter 3

Experimental Apparatus and Sample Details

3.1 Introduction

This chapter details all the samples under investigation. The experimental apparatus used for the Zeeman splitting experiments is discussed, together with the method used to aquire the data. The three main experiments presented in this thesis had a similar setup, and therefore information relating to the neccessary modifications to the experimental apparatus is given. Finally, relevant detailed information on each major component used in the experiments is given.

3.2 Samples

See table 3.1 for a summary of sample properties. All samples are self organized quantum dots grown by Dr H. Henini of Nottingham University. For samples NU1652, NU1654, NU1658, NU1660, and NU1659, a very thin amount of arsenic was used to passivate the substrate at 580°C, then 0.20μm of GaAs was deposited at 580°C, a further 0.50μm of GaAs was deposited at 600°C, L nm (see table 3.1) of $Ga_{0.5}In_{0.5}As$ was then deposited to form the quantum dots and capped with 250Å of GaAs at 450°C. Arsenic was again used to passivate the sample surface at 300 °C.

Sample NU1511 had somewhat different growth conditions, arsenic was blown over the substrate at 580°C, then 0.20μm of GaAs was deposited at 580°C, a further 0.50μm of GaAs was deposited at 600°C, 0.8μm of InAs was then deposited to form the quantum dots and capped with 254.4Å of GaAs at 450°C. Arsenic gas was again blown over the surface of the

Sample Growth Properties		
Sample Name	Crystallographic Orientation	L(nm)
NU1652	100	1.1
NU1654	311	1.1
NU1658	100	1.7
NU1659	(311)A	1.7
NU1660	(311)B	1.7
NU1511	100	1.8

Table 3.1: **Table showing known characteristics of the quantum dot samples.**

sample at 300 ^{o}C.

Reference [1] gives information on the possible shape of the samples. (311) grown SAQD's appear arrow shaped, elongated along the [233] direction. The (100) grown dots on the other hand appear to be isotropically distributed, with a dome like shape. Because these samples were not annealed after growth, we believe they do not exhibit the phonon bottleneck and therefore, for our pump powers, we believe multiphonon relaxation of electrons is the dominant carrier relaxation mechanism.

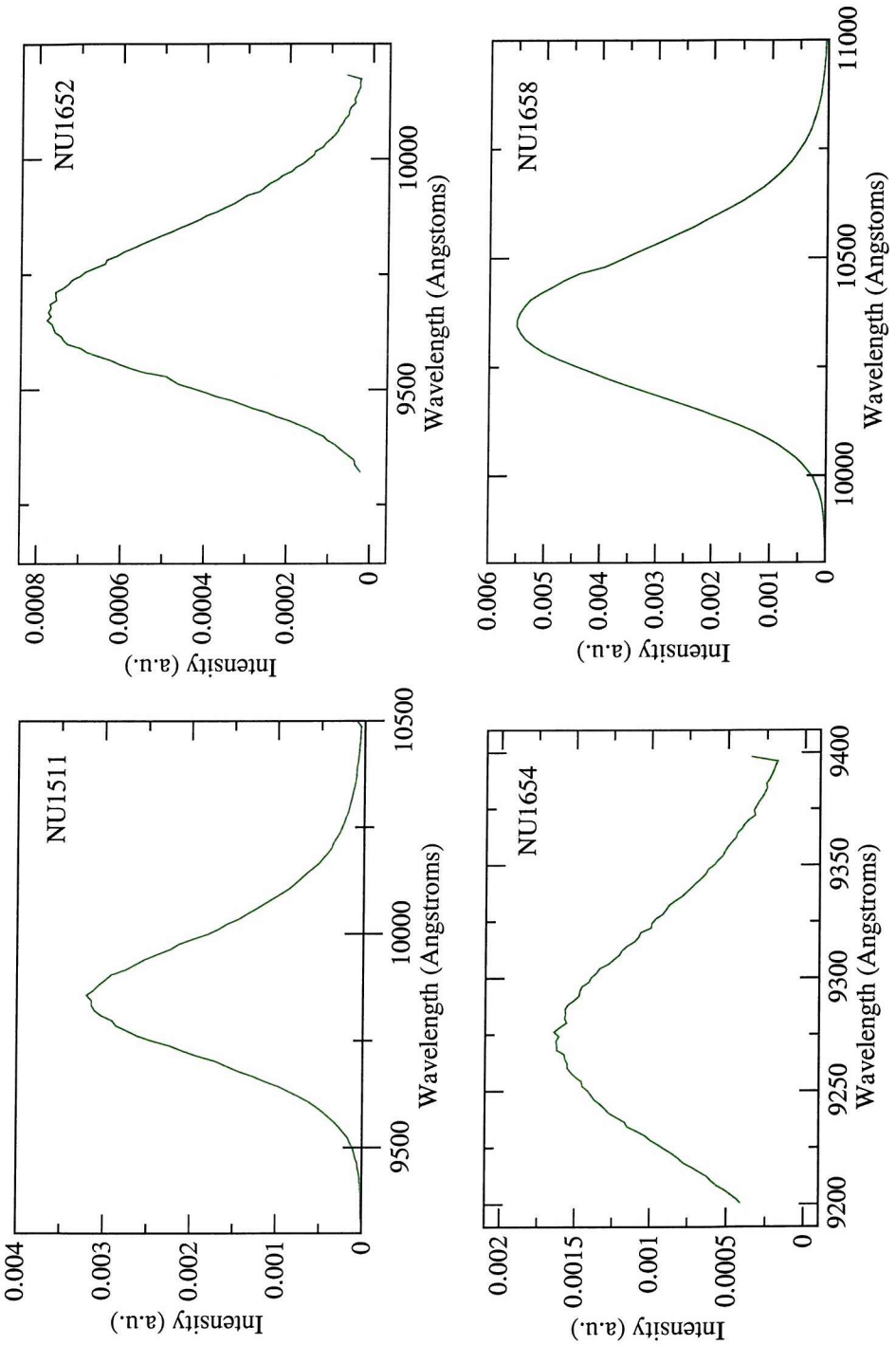

Figure 3.1: **Photoluminescence Spectra from Samples under Investigation.**

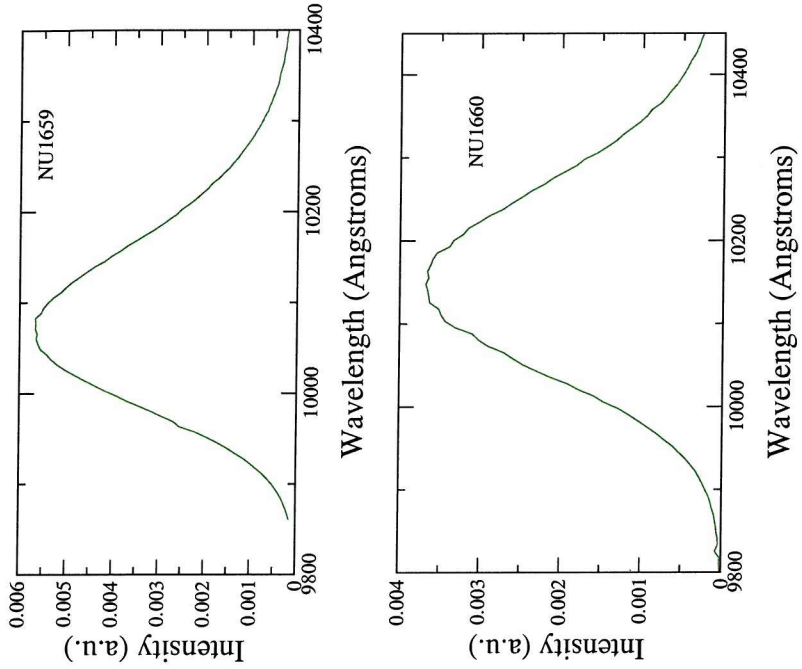

Figure 3.2: **Photoluminescence Spectra from Samples under Investigation.**

Sample Photoluminescence Properties		
Sample Name	PL Peak (eV)	PL Width (eV)
NU1652	1.288	0.052
NU1654	1.339	0.017
NU1658	1.198	0.055
NU1659	1.234	0.027
NU1660	1.227	0.031
NU1511	1.262	0.044

Table 3.2: **Table showing measured photoluminescence characteristics of the quantum dot samples.**

3.3 The Optical Orientation Apparatus

Figure 3.3 shows the general experimental apparatus. Light from an Argon Ion pumped Titanium Saphirre laser was regulated by means of an array of neutral density filters, the optical power incident on the sample was measured directly to ensure comparable power densities for each spectrum.

After some steering optics, the beam was polarised either linearly, or right (σ^+), or left (σ^-) circularly polarised using a linear polariser and quarter wave plate combination. It was also possible to introduce alternating circular polarisation between $\sigma^+$and σ^-using a linear polariser and a rotating zero order quarter wave plate combination, (central wavelength 800 nm). The beam was then focused down to a diameter of about 400μm via a biconvex lens, (f=25 cm), to produce an average power density of about 1.8 Wcm^{-2} at the sample surface. In order to ensure a free beam path for the photoluminescence, the focusing lens was sliced in half as detailed in figure 3.3.

The sample was located at the core of a 6 Tesla split coil super-conducting magnet, oriented so that the field lines were either parallel or anti-parallel to the growth direction of the sample, (the Faraday configuration). The magnet was powered by a 75 Amp constant current power supply built in-house, (labeled P.S.U. in diagram 3.3), with the current being programmable by means of a manually controlled 0-10 volt ramp unit.

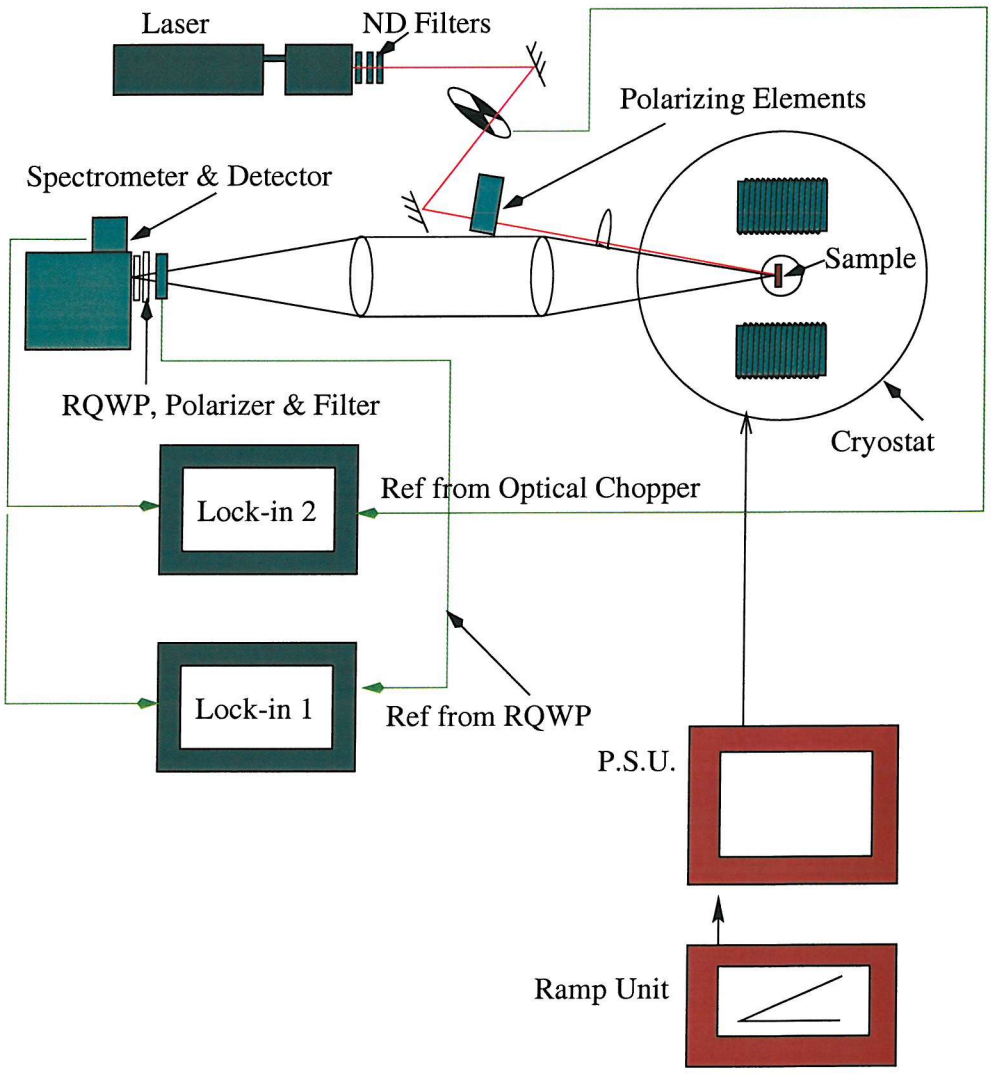

Figure 3.3: **Diagram showing the general optical orientation experimental apparatus.**

Luminescence from the sample was collected and collimated by a convex lens (f=30 cm), and then focused using an identical lens onto the slits of a single grating Jobin Yvon HR320 spectrometer (f=0.35 m). The photoluminescence was analyzed by a rotating quarter wave-plate (RQWP) and linear polariser combination situated at the input slits of the spectrometer. A filter was also placed in front of the input slits of the spectrometer to block scattered laser light. The central wavelength of the RQWP was 1 μm and of zero order.

Light from the spectrometer was dispersed into a North Coast Germanium PIN photo-detector which was located at the exit slits of the spectrometer. In order to reduce noise in the amplifier, it was cooled to 77K by liquid nitrogen. The output of the detector was connected to the inputs of two Stanford analogue lock-in amplifiers whose references were taken from the RQWP, whose frequency range was 130-140Hz, and the optical chopper, (frequency of the order 1kHz). Successive photoluminescence spectra were then recorded as a function of applied magnetic field.

The accuracy of the positioning of the sample with respect to the collected luminescence was determined by reflecting the beam off of the sample and measuring the angle between the incident and reflected beams. This was due to the fact that linear polarised radiation has a dipolar pattern proportional to $\sin^2 \alpha$, where α is the angle between the perpendicular to the growth direction and the direction where the measurements were made, and therefore, accurate positioning of the sample, collection optics, magnets and incident laser beam was required.

3.4 Analysis of the Photoluminescence

The photoluminescence was analyzed by the RQWP and linear polariser combination situated at the inputs of the spectrometer. The RQWP is located in a cylinder within a circular bearing housing so that it can rotate freely. It is driven by an o-ring that was stretched around the cylinder and a shaft of a DC motor with integral tachometer. This allows constant speed operation through electronic feedback in the control circuit of the DC motor. The reference signal, at twice the rotation frequency is provided by an LED and photo-diode which detect two holes cut into the cylinder at 180^o to each other. This provided an accurate and stable reference frequency for one of the lock-in amplifiers.

Circular light passing through the RQWP will become linearly polarised rotating at the frequency of the rotating quarter wave plate, and linear polarised light will produce alternating $\sigma^+$and σ^-light separated by the original linear polarisation at twice the frequency of the rotating quarter wave plate. For σ^+light passing through the RQWP and polariser combination, the transmitted intensity is given as:

$$I_{\sigma+} = \frac{I_{\sigma+}}{2}[1 + cos(2\omega t)] \tag{3.1}$$

where $I_{\sigma+}$ is the intensity of the σ^+component, ω is the angular frequency of the rotating quarter wave plate and t is time. For σ^-incident light the transmitted intensity ($I_{\sigma-}$) is in anti-phase with the $I_{\sigma+}$ curve.

The Lock-in signal whose reference was taken from the optical chopper

records the total photoluminescence collected, ($(I_{\sigma+} + I_{\sigma-})$ or the sum signal), while the lock-in whose reference was taken from the RQWP and linear polariser combination allows selective transmission of σ^+or σ^- light in alternative half cycles, ($(I_{\sigma+} - I_{\sigma-})$ or the difference signal).

We had to normalize the two outputs of each Lock-in signal due to the differing responses the detector has at each reference frequency. This was done by passing light from a white light source through a quarter wave plate whose central wavelength was 1064Å, thus introducing σ^-light into the detector system at roughly the same wavelength range as the photoluminescence peaks from the samples. The apparent degree of circular polarisation was then recorded as a function of wavelength and this was then used to normalize the measured photoluminescence spectra.

3.5 Data Acquisition

A data flow chart is shown in figure 3.4 for reference. An IBM 386 PC running a data acquisition programming language – Asyst was used to obtain the data. The computer was linked to a Microlink multiplexer unit via a National Instruments IEEE/GPIB board. The microlink controlled the lock-in detectors and spectrometer while laser emission wavelength selection, magnetic field sweep rate and magnetic field strength were selected manually. The magnetic field strength was monitored by a shunt resistor provided at the back of the P.S.U.

Near total automation of the experiment was achieved through a programmable stepper motor controller card that allowed automation of the

spectrometer. Analogue signals were used to control the stepper motor controller sent through the microlink interface giving the added advantage that mechanical backlash from the spectrometer gearing was consistently removed.

Once the lock-in amplifiers had been set up and calibrated, and the desired magnetic field strength had been obtained, the spectrometer wavelength selector was positioned at the lower wavelength of the photoluminescence peak to be recorded.

The computer was then set to begin its run, the sum and difference signals were recorded simultaneously as a function of wavelength to obtain the full photoluminescence line profile. In order to ensure adequate integration time for the lock-in amplifiers, a delay of six times the time constant of the lock-in amplifiers was performed. The sum and difference signals were then read and saved to disk with the values for the current wavelength setting from the spectrometer, and the value of the current field strength.

3.6 Modification to the Optical Orientation Apparatus

The Hanle effect measurements required a magnet that could be set precisely to zero because the small Hanle signals tend to decrease rapidly with

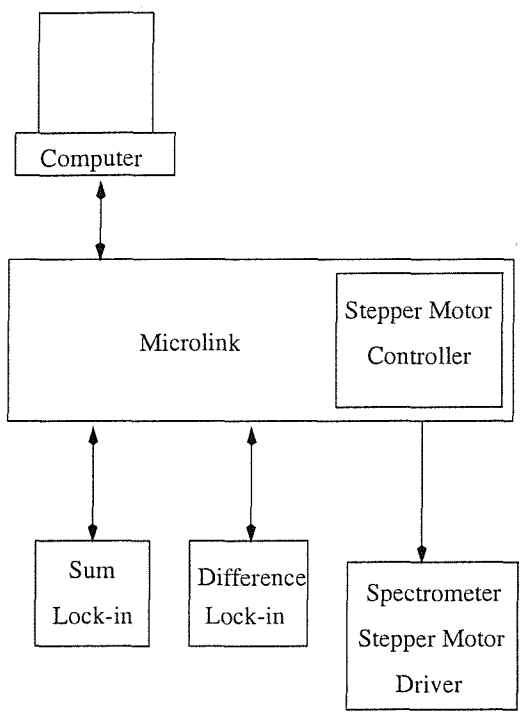

Figure 3.4: **Flow Diagram of the Optical Orientation Apparatus.**

any value of field. This was not possible with the super-conducting magnet due to reminant fields. Therefore the setup was changed by exchanging the bath cryostat and super-conducting magnet for a continuous flow cryostat positioned between the poles of an electromagnet. This modification gave a considerably improved photoluminescence collection aperture and also allowed rotation of the sample with respect to the magnetic field direction.

The Hanle effect requires measurement of the degree of polarisation of the photoluminescence line as a function of applied magnetic field. Therefore the spectrometer slits were opened to give a passband comparable to the photoluminescence line width. This allowed integration of the intensity of the line while simultaneously blocking scattered laser light.

Since the measurements required automation of the magnetic field sweep, we used (in place of the original Asyst program), the Tool Command Language (TCL), together with the graphical interface TK and the GPIB libraries with their TCL extensions to perform the required data acquisition. The microlink was taken out as there are ADC ports on the back of the Stanford lock-in amplifiers with which all other components could be controlled.

The lock-in amplifiers were calibrated by passing 100% circular polarised light through the system and maximizing the phase to obtain the maximum amplitude. The sum and difference signals were then recorded as a function of the applied DC magnetic field.

For the ODNMR measurements, one further modification had to be made,

a search coil was added to the sample holder to produce a radio frequency magnetic field at 90° to the DC magnetic field. Here we examine the total polarisation of the photoluminescence as a function of radio frequency at an applied static magnetic field strength. A synthesized radio frequency source and power amplifier were used to drive the coil.

The experimental procedure was as follows: The lock-in detectors were calibrated in the same manner as with the Hanle effect experiment, the static magnetic field was ramped to its desired value. The experiment was the left for a period of twenty minutes to allow for alignment of the nuclear species with the static magnetic field.

A radio frequency field was then turned on and the degree of resulting polarisation recorded together with the static magnetic field strength and the radio frequency value. Again a delay of six times the lock-in time constant was used to ensure adequet integration of the signal.

3.7 Cryostats

3.7.1 Vaughan and Cameron Bath Cryostat

The super-conducting magnet was cooled in a 10 litre Vaughan and Cameron bath cryostat. A vacuum jacket between the outer wall and the inner cans was pumped down to about $5x10^{-6}$ Torr. The can surrounded by the vacuum jacket contains about 10 litres of liquid nitrogen. This in turn cools a 77K radiation shield surrounding the bottom of the helium can.There are four sets of fused quartz windowsallowing optical access to the centre of

the helium can.

The helium can contains both the sample, (mounted on a sample stick), and a 6 Tesla split coil super conducting magnet. The sample stick carries a number of circular brass spacers that fit snugly into a tube that runs down the length of the cryostat to the centre of the magnet. Baffles are also attached to this tube which fit snuggly to the inner wall of the helium can. The bottom of the sample stick fits into a housing at the bottom of the magnet. In this way, lateral movement and vibration of the sample is suppressed.

The magnet is suspended via three hollow stainless steel tubes connected to the removable top plate and also to the brass baffles positioned at equal distances at the top of the helium space to act as radiation shields, the location of the magnet in the helium can prevents lateral movement of the magnet during operation.

Optical access to the sample was via four fused quartz windows positioned at 90^o intervals at the same height as the sample. Filled with liquid helium, the helium space was pumped continuously during the experiment to induce super fluidity. This removes bubbles from boiling helium and lowers the base temperature from 4.2K to 1.8K and is essential for optical experiments. The cryostat has a helium hold time of 16 to 20 hours with a fill of 10 litres of helium.

3.7.2 Oxford Instruments Continuous Flow Cryostat

The Oxford instruments continuous flow cryostat was used for the Hanle effect and ODNMR measurements. Liquid helium is forced from a storage dewar by a rotary pump connected to the helium return line into the heat exchanger. The transfer of helium from the dewar is done in a controlled manner by means of a needle valve located in the transfer tube.

A diode used as a temperature sensor and a resistive heater is located in the heat exchanger and in combination with an Oxford Instruments ITC4 temperature controller, allows a stabilisation of the temperature in the sample space from 4.2 K to room temperature.

The sample sits on a sample stick in direct proximity to the heat exchanger and therefore cold helium gas can flow around the sample ensuring the sample temperature can be maintained at 4.2K. Surrounding the heat exchanger is a radiation shield which in turn surrounds a vacuum jacket pumped to a pressure of around $5x10^{-6}$ Torr. The warm helium gas is passed through the transfer tube, a rotary pump and into the return line for recycling. Localised heating effects on the sample due to high laser powers can be a problem when using this type of cryostat due to the fact that the liquid helium is not in direct contact with the sample.

3.8 North Coast Germanium Detector

The North Coast germanium detector model number CEO817E comprises a Germanium PIN diode photo detector element that is sensitive to light

in the range 0.7-1.7μm. The detector includes a preamplifier of which the first stage and the feedback circuit is cooled to 77K by liquid nitrogen and has a measured bandwidth of 20 kHz. The dark noise equivalent power of the detector is 6x10^{-15} WHz$^{-\frac{1}{2}}$. Additionally, the detector is sensitive to cosmic rays which produce random spikes at the output.

For the ODNMR experiments, the signals due to the nuclei were an order of magnitude smaller than these spikes and therefore we used a sample and hold circuit to remove the spikes in real time.

3.9 Laser Systems

3.9.1 Argon Ion Laser

A Coherent I90 Argon ion laser, rated initially at 4W and upgraded later to 6W provided the pump source for the Titanium Sapphire laser. It was operated in multi wavelength mode. The principle wavelengths of 488nm and 514 nm show strong absorption in the crystal rod of the Titanium-Sapphire laser.

3.9.2 Titanium-Sapphire Laser

All experiments presented in this thesis required laser absorption into the GaAs (800 nm) bulk. Therefore a Spectra-Physics 3900 CW Titanium sapphire laser was used giving wavelengths selectable between 700 and 850nm by means of a birefringent filter and a micrometer. A pump power of 5W typically produced 60mW laser power at 800nm.

3.10 Magnets

3.10.1 Electromagnet

The magnet was a split coil 0.1 Tesla resistive magnet, used for both the Hanle effect measurements and the ODNMR measurements with a maximum field of about 0.12 Tesla. For calibration, we used an Oxford Instruments Hall probe and meter. The probe was situated with the flow cryostat removed at the same position as the sample with the flow cryostat in position. The field was then swept making a calibration curve for the magnet, the cryostat was then replaced and the same calibration was performed with the Hall probe situated to one side of the cryostat. With this data available, it is possible to calibrate for the field inside the cryostat with respect to the field measured outside the cryostat. Hysteresis effects were smaller than the homogeneity of the field strength across the poles of the magnet.

3.10.2 Super-conducting Magnet

A split solenoid 6 Tesla super-conducting magnet was used for the exciton g-factor experiments, and housed in the bath cryostat. It was controlled by means of a 75 Amp home built power supply. The power supply was in turn controlled by means of a variable sweep rate controller, also built in-house. Field measurement was measured by the voltage across a shunt resistor fixed to the power supply unit.

3.11 The Radio Frequency Synthesizer

The radio frequency source was a Wavetek 178 0.1-50MHz Waveform Synthesizer producing a sine wave of amplitude 0-20V into a 50 Ω load. The minimum frequency steps were 5μHz with an error of $\pm$0.01μHz.

Although it was possible to select the sweep mode in which the frequency is swept from one frequency to another in a specified sweep time, it was decided we would set individual frequencies and use the TCL program to set the resolution of the instrument as this produced greater control of the experiment.The signal was boosted by a radio frequency amplifier providing a field strength of 0.1-0.7 mT.

3.12 Spectrometer

A single grating Jobin Yvon HR320 spectrometer was used for all experiments presented in this thesis. It had a 0.35 m focal length. For the exciton g-factor measurements, the spectrometer was controlled using the microlink interface together with a stepper motor controller circuit, this was modified for the Hanle and ODNMR experiments when a computer's parallel port provided the necessary clock pulses directly. The resolution was measured to be 0.018 Åμm^{-1}. For the exciton g-factor experiment, the resolution was of the order 4Å.

Bibliography

[1] M. Henini, S. Sanguinetti, S.C. Fortina, E. Grilli, M. Guzzi, G. Panzarini, L.C. Andreani, M.D. Upward, P. Moriaty, P.H. Beton, and L. Eaves, Phys. Rev. B, **57**, 6815 (1998)

Chapter 4

Exciton g-factors in $In_{0.5}Ga_{0.5}As$ Quantum Dots

4.1 Introduction

Knowledge of the exciton g factor in SAQDs is important because it is a function of the spin and orbital angular momentum and therefore gives a sensitive measure of the electronic structure in these systems. It also governs the spin-splitting in a magnetic field and therefore is relevant for magneto-optical polarisation measurements, and electron-nuclear spin coupling [1]. This chapter details the Zeeman splitting measurements done to obtain the exciton g factors (g^*_{ex}), in a series of $In_xGa_{1-x}As/GaAs$ SAQD samples.

Electron states are usually degenerate in spin in the absence of a magnetic field. The application of a magnetic field will tend to lift this degeneracy and the difference in energy between the spin split states is called the Zeeman effect. Examination of the spectra of recombination radiation in the presence of an applied magnetic field will therefore show a splitting in the photoluminescence line profile.

In the following measurements, we use a technique originally described by M. Snelling [2] to obtain the exciton g factors in a series of GaAs/-$Al_xGa_{1-x}As$ quantum wells. This technique was applied because it is possible to obtain both the sign and magnitude of the Zeeman splitting simultaneously in the regime where the photo-luminescence line-width is very much greater than the value of the Zeeman splitting. Therefore a direct determination of the Zeeman splitting energy is impossible.

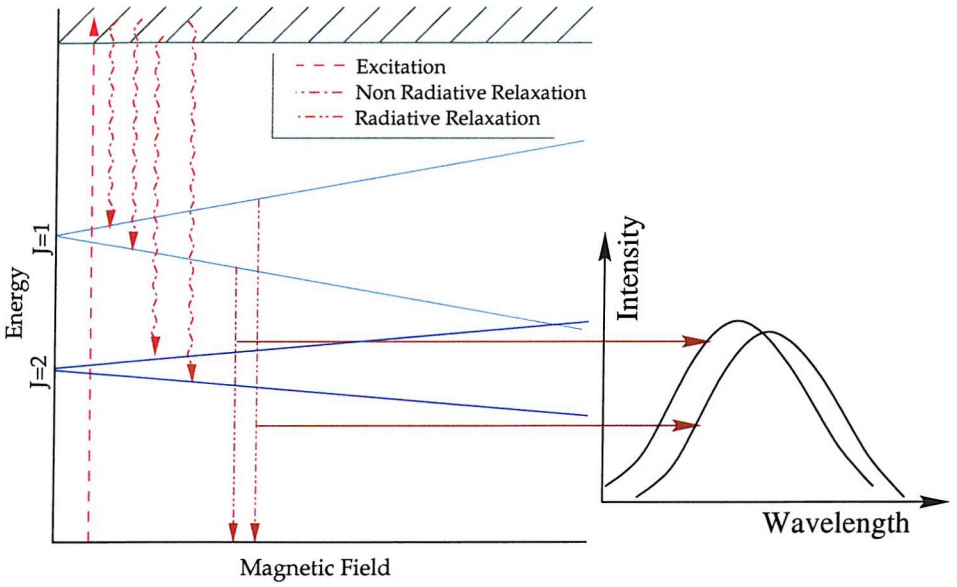

Figure 4.1: **Diagram Showing the Dynamic Transitions assumed to be valid for the exciton g factor experiment**

4.2 Experimental Background and Theory

The exact relaxation mechanism in the SAQDs and wetting layer is controversial [3]. The pump laser was tuned to 800 nm (the GaAs bulk) where electrons undergo non-radiative relaxation to the SAQD states. Also, due to the fact that the QWP has a central wavelength of 800 nm, we ensured 100% σ^+ or σ^- polarised light entering the sample. For wavelengths smaller than 800 nm, the energy in excess of the bulk band-gap energy results in loss to the lattice via elastic collisions. At each collision, the spin orientation is also altered, and therefore we would expect a decrease in optical orientation with increasing pump energy.

The absorption of light into the sample excites carriers from the valence

band into the conduction band of the GaAs bulk. The carriers then undergo non-radiative relaxation and may be captured by the quantum dots where they form excitons (see figure 4.1). These excitons may be characterised by their angular momenta projections M [4] in the growth direction (z):

$$M = S_{e,z} + J_{h,z} \tag{4.1}$$

where $S_{e,z} = \pm\frac{1}{2}$, the electron spin, and $J_{h,z} = \pm\frac{3}{2}$, the heavy hole spin projected in the z direction. Due to the strain between dot and substrate, the heavy and light holes are strongly split in energy and therefore the light holes may be neglected for this theoretical analysis [4].

For linearly polarised excitation, near equal populations of the four basis exciton states is expected, tending towards a Boltzmann distribution. However, the degree of thermalisation depends on the relaxation rates between levels and the radiative recombination time. The g factor comes from an understanding from the properties of an electron in a magnetic field, therefore we introduce the Larmor frequency. The precessional motion of a charged body in a magnetic field is given by the Larmor frequency ,Ω [5].

$$\Omega = \frac{q\mathrm{B}}{2m} \tag{4.2}$$

where q is the charge, B the magnetic field strength and m is the mass of

the charged object. For an electron, the Larmor frequency is:

$$\Omega = \frac{g_e \mu_B B}{\hbar} \tag{4.3}$$

where g_e is the electronic Lande g factor and μ_B is the Bohr magneton given by :

$$\mu_B = \frac{e\hbar}{2m_e} \tag{4.4}$$

where e is the electron charge. The electron g factor is actually the ratio between electronic spin to orbital motion and is influenced by the coupling of angular momenta between electrons. For a free electron, g takes the value 2.00232 but, because electrons in a lattice are subject to spin-orbit coupling between the highest valence band (HH) and the lowest conduction band (CB), an effective g factor (denoted g_e^*) which is different to that of the isolated atomic case exists. Therefore the orbital contribution to the g factor is associated with the band structure due to spin-orbit coupling. The interaction of heavy hole and electron spins in an external static magnetic field B is [6][7][8]:

$$\hat{H}_z(B) = \mu_B \sum_{i=x,y,z} (g_{e,i}^* S_{e,i} - \frac{g_{h,i}^*}{3} J_{h,i}) \tag{4.5}$$

where μ_B is the Bohr magneton, and g_e^* and g_h^* are the electron and hole g factors respectively. By using the basis states $|M = \pm 1>, |M = \pm 2>$, the matrix describing the interaction of spins with the magnetic field, (B =

$(sin\theta, 0, cos\theta)$ with $\theta = 0^o$) is:

$$H_z(B) = \frac{\mu_B B}{2} \begin{pmatrix} (g^*_{e,z} + g^*_{h,z}) & 0 & 0 & 0 \\ 0 & -(g^*_{e,z} + g^*_{h,z}) & 0 & 0 \\ 0 & 0 & (g^*_{e,z} - g^*_{h,z}) & 0 \\ 0 & 0 & 0 & -(g^*_{e,z} - g^*_{h,z}) \end{pmatrix} \quad (4.6)$$

Assuming rotational symmetry along the growth direction, the solution to the above equation gives the Zeeman splitting of the optically active states as:

$$\Delta E = \frac{\mu_B B_z}{2}(g^*_{e,z} + g^*_{h,z}) \quad (4.7)$$

and

$$\Delta E = \frac{\mu_B B_z}{2}(g^*_{e,z} - g^*_{h,z}) \quad (4.8)$$

for the optically inactive states. It is customary to allow:

$$g^*_{e,z} + g^*_{h,z} = g^*_{ex} \quad (4.9)$$

where g^*_{ex} is called the exciton g factor and equation 4.7 becomes:

$$\Delta E = \frac{\mu_B g^*_{ex} B_z}{2} \quad (4.10)$$

which is the equation we have used to obtain the exciton g factor in our measurements.

4.3 Determination of the Zeeman Splitting

The method used to extract the Zeeman splitting value from the sum, ($I_{\sigma+}$ + $I_{\sigma-}$) and the difference signal, ($I_{\sigma+}$ – $I_{\sigma-}$) was originally described by M. Snelling [2]. Once the data had been calibrated for the response of the system, it is possible to obtain the value of the Zeeman splitting. After the σ^+ and σ^- components of the spectra were separated from the sum, and difference components, (see figure 4.3 for example data), the Zeeman splitting of the exciton may be obtained by accurate determination of the energy separation of the two components as described below.

The σ^+ and σ^- components all appeared to progressively split with increasing field, however there was also a corresponding increasing difference in intensity between the σ^+ and σ^- components. This is due to the greater difference in the population distribution of levels, and as this would translate, when combined with any spectral asymmetry into a fictitious splitting, the components were normalised before the determination of the Zeeman splitting value.

A Gaussian is fitted to one component of the spectra using a non-linear least squares method, then the mean square deviation of the line profile with respect to the other component for a series of energy shifts was calculated, (see figure 4.2). It was found that the mean square deviation passes through a minimum at a certain value of energy displacement which was taken to be the value of the Zeeman splitting.

The limiting statistical uncertainty with which the line position may be

known is $\frac{1}{n\sqrt{N}}$ where n is the number of points in the spectrum and N is the wavelength integrated photoluminescence intensity. Therefore, the second assumption is that the fitted line follows the measured spectrum exactly. The individual quantum dot line shape is Lorentzian and the size distribution Gaussian, this produces a voidian line profile in the photoluminescence spectra which is insolvable analytically. Therefore we assumed a Gaussian line shape to fit the experimental data.

In order to see whether this introduced systematic errors into the splitting determination, we fitted a series of Gaussian lines to known numerically calculated splittings using two voidian line profiles, one shifted by a known value. We found no evidence that this introduced any systematic error in the splitting determination. It is important to note that due to the fact that the growth method produces a dot density of the order 10^{10}cm^{-2}, we cannot obtain a sufficient spatial resolution to resolve individual SAQDs. Therefore, the value of the Zeeman splitting obtained by measurement is the average value over the entire ensemble.

Finally, because the method allows the complete separation of the spin split components, we can ascertain the sign of the g factor using equation 4.10.

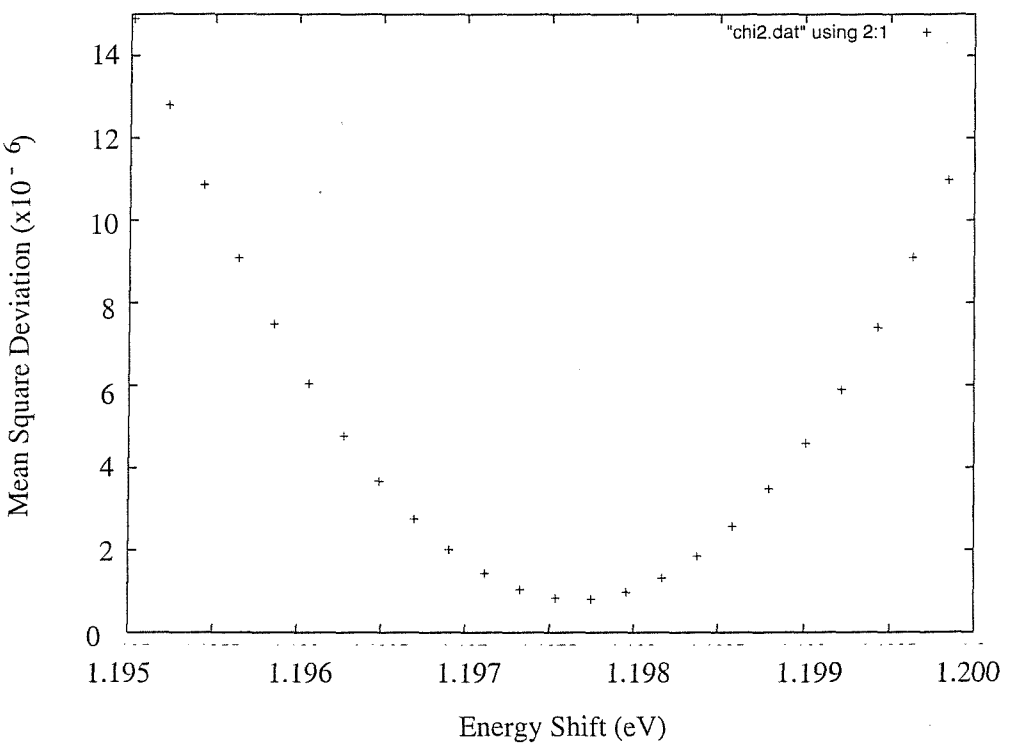

Figure 4.2: **Diagram showing the variation of the mean square deviation of the Gaussian fit as a function of energy displacement. The minimum is taken to be the difference between the spin split components.**

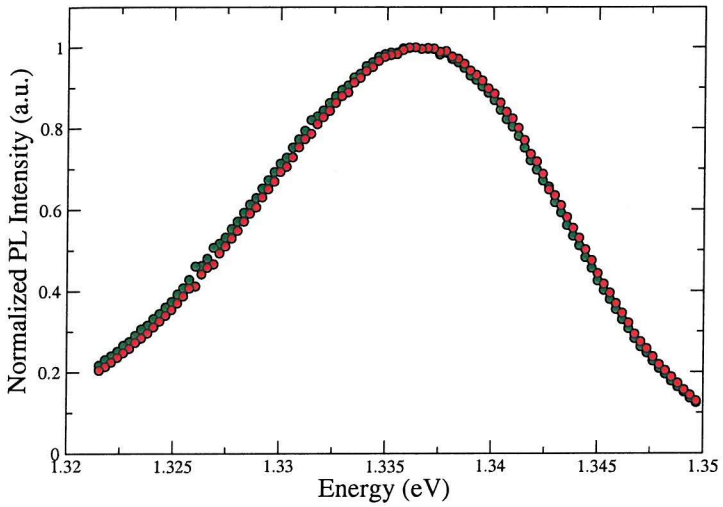

Figure 4.3: **Diagram showing the $\sigma^+$and σ^-components of the PL after normalisation.**

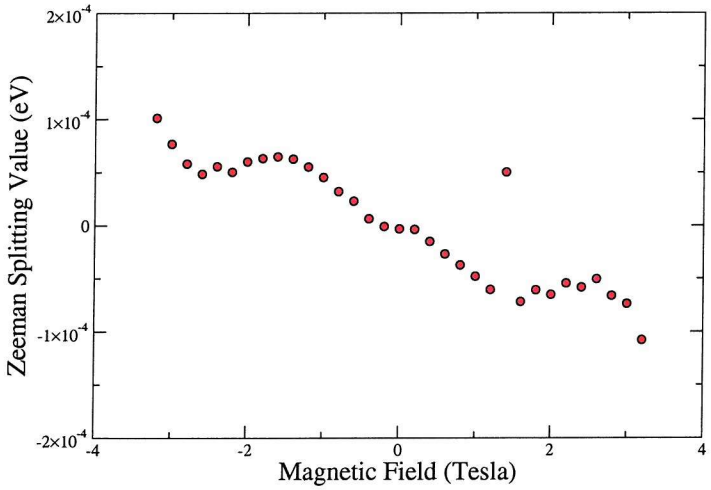

Figure 4.4: **Diagram showing the Zeeman splitting of the quantum well RMB1040 used to ensure the experimental setup was working as expected.**

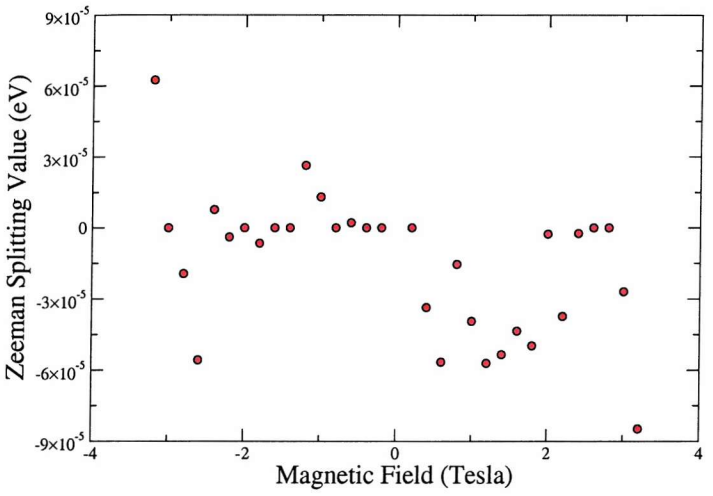

Figure 4.5: **Diagram showing the Zeeman splitting of NU1511 using linearly pumped light.**

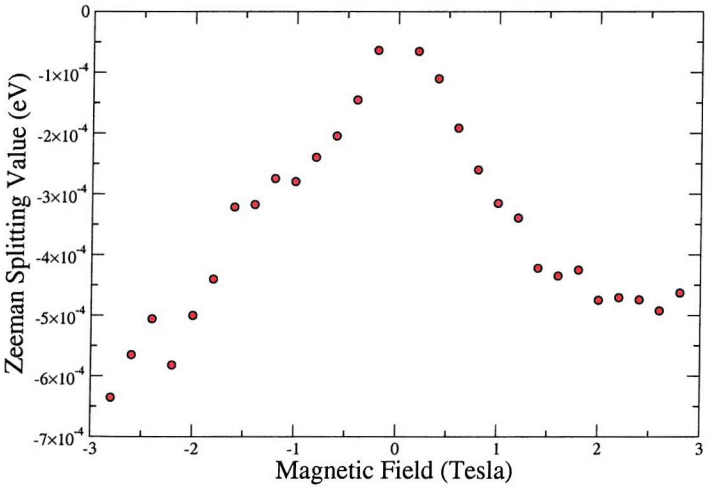

Figure 4.6: **Diagram showing the Zeeman splitting of NU1652, pumping polarisation was linear.**

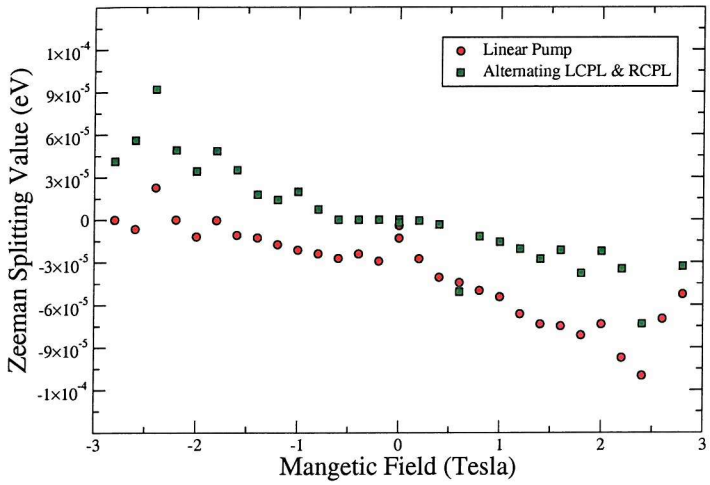

Figure 4.7: **Diagram showing the Zeeman splitting of sample NU1654 pumped with linear light and alternating L/RCPL.**

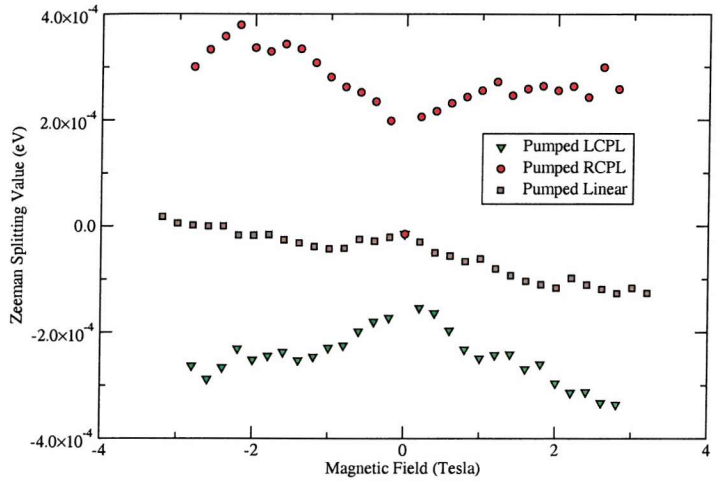

Figure 4.8: **Diagram showing the Zeeman splitting of sample NU1654, pumped with LCPL, RCPL, and linear light.**

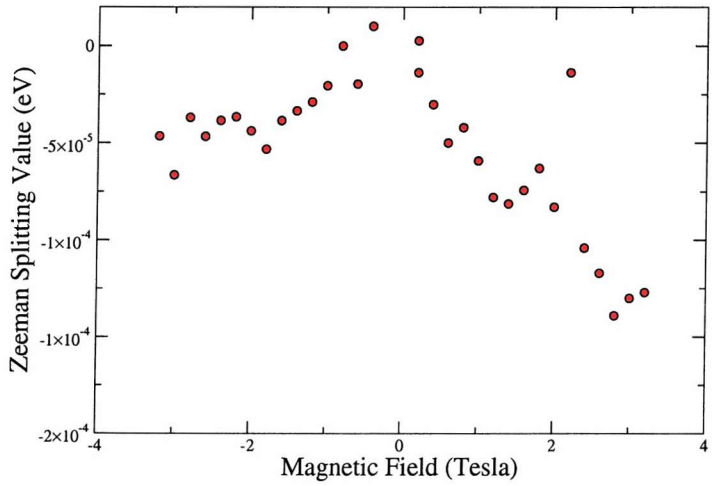

Figure 4.9: **Diagram showing the Zeeman splitting of sample NU1658, pumped with linear light.**

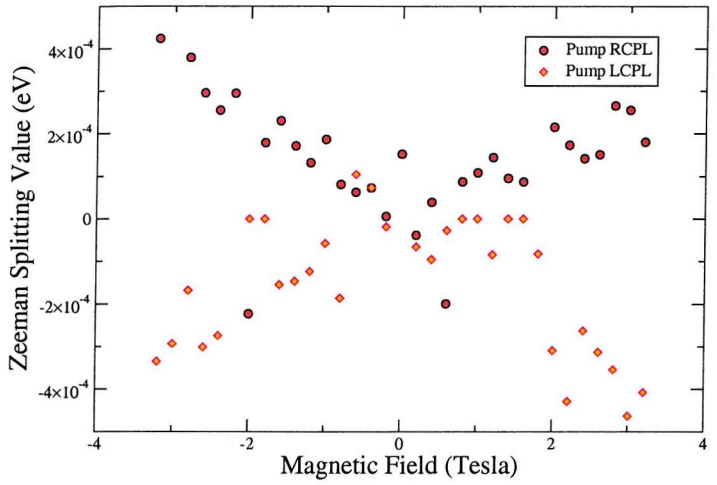

Figure 4.10: **Diagram showing the Zeeman splitting of sample NU1658, pumped with LCPL and RCPL.**

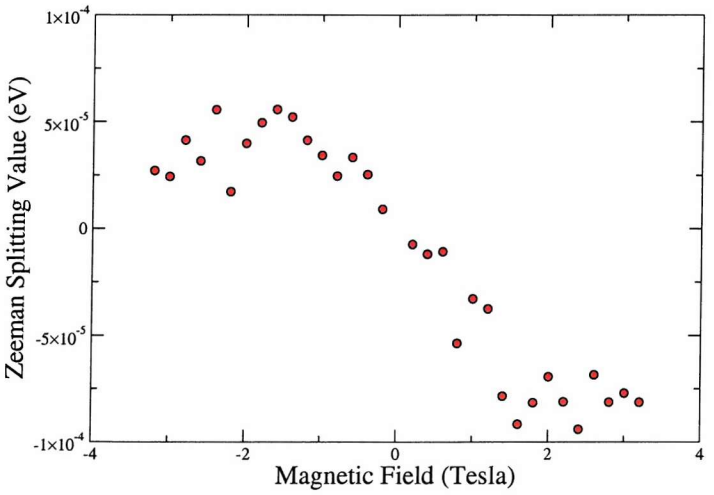

Figure 4.11: **Diagram showing the Zeeman splitting of NU1659 pumped with linear light.**

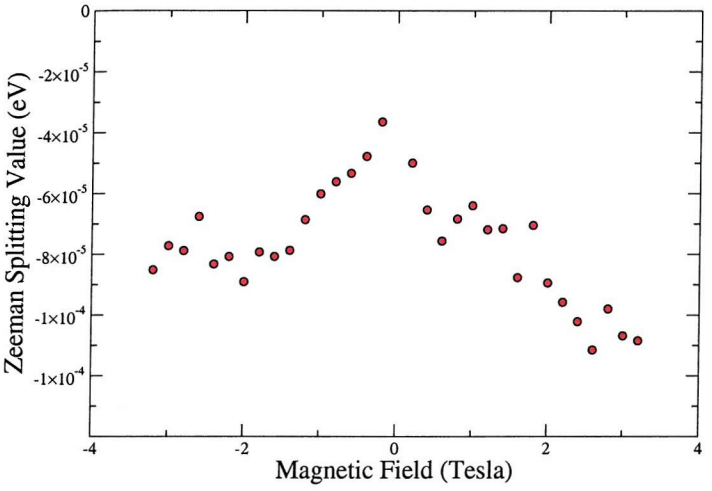

Figure 4.12: **Diagram showing the Zeeman splitting of sample NU1660 pumped with linear light.**

4.4 Results

Figures 4.4 – 4.12 show the apparent Zeeman splitting for a variety of pumping conditions and table 4.1 gives the measured exciton g factors using the method described in the previous section.

In order to ensure the experimental apparatus was giving consistent results, we obtained a single quantum well sample, RMB1040 whose photoluminescence spectrum showed a single peak at the same wavelength as the spectra from the SAQD's. We then pumped the sample with linear light and recorded the spin-split components as a function of applied field.

The result for this is shown in figure 4.4. As may be seen, the low field Zeeman splitting is linear, deviating from linearity with increasing field.

Sample g factors	
Sample Name	g factor
NU1511	undetermined
NU1652	-5.1±0.3
NU1654	-0.3±0.3
NU1658	-0.9±0.1
NU1659	-1.0±0.2
NU1660	-0.3±0.1

Table 4.1: **Table showing measured exciton g factors from the SAQDs.**

There is also a peak at 1.5 Tesla, this has been first observed by Snelling [2] and has been attributed to mixing between the optically active and the optically inactive states due to differing effective masses of their carriers [7]. We then changed the quantum well sample for a SAQD sample and repeated the experiment. We expected a curve similar to figure 4.4, in other words, we expect the sign of the Zeeman splitting to change when we change the direction of the magnetic field. As may be seen in figures 4.5–4.12, the sign of the Zeeman splitting does not change for a change in magnetic field direction. The other point to notice is that the magnitude of the Zeeman splitting is also considerably smaller than the quantum well sample. We initially used a linear pump to ensure equal spin populations of spin up and spin down carriers in the SAQDs. However, as may be seen in figure 4.7, the response deviated substantially from that described by equation 4.10.

However, the Zeeman splitting curves for the SAQDs are very similar to that found in reference [9] that describes the Zeeman splitting in the pres-

ence of a nuclear field, and therefore it was decided to examine the response of the Zeeman splitting for a variety of different pumping conditions, the results of which may be seen in figures 4.7 and 4.8 for sample NU1654.

We believe that the deviation from equation 4.10 in the linear pumping case is due to the ellipticity of the linear pump polarisation induced by birefringence in the quartz windows of the bath cryostat, (the strain is caused due to contraction and distortion in the material at liquid helium temperatures). The very small amount of ellipticity produced in this way was enough to cause the build up of nuclear spin polarisation, and due to the larger value of feedback in these systems on the hyperfine interaction, effect recombination radiation.

In order to suppress the nuclear field, we pumped the sample by alternating the circular polarisation between left and right circular polarised light rapidly. This has the effect of destroying all nuclear polarisation because although electron spin has sufficient time to polarise, the nuclear system does not, and therefore no net nuclear spin can build up. For excitation with circular polarised light, the samples consistently show elliptical recombination radiation, therefore the sum of the spin relaxation times in the cascade process must be greater than the sum of recombination times.

The sign of the g factor is negative in all samples, this may be easily seen by making a comparison with equation 4.10 and the slope of the curves in the figures when the nuclear field is suppressed, (suppression of the nuclear field occurs on pumping the sample with alternating LCP and RCP light).

The number of published papers that examined the exciton g factor in SAQDs has slowly increased in the last decade. One of the most striking results is that there is a strong variation of measured exciton g factors in similarly grown systems [10]. Also a number of methods have become available to allow examination of single SAQDs: methods used include the reduction of the inhomogeneous photo-luminescence line width by interrupted growth [10], near field optical microscope techniques to obtain the required spatial resolution [11], electron beam lithography and wet chemical etching to decrease the number of SAQDs grown [12] [13] and the growth of mesa structures to ensure only a few dots are optically excited [4].

The exciton g factors show a wide variation in value. For example, for InAs/GaAs SAQD systems, Wilson [14] gives an exciton g factor of 0.7, while Toda [11] found the exciton g factor to be in the range 1.21 – 1.73, (the SNOM technique allowed individual SAQDs to be resolved). We have unfortunately not been able to measure an exciton g factor for our only InAs/GaAs SAQD (NU1511), as the splitting data was too noisy to ascribe a sensible g factor to,(see figure 4.5).

There have also been a number of g factor studies into $In_xGa_{1-x}As/GaAs$ systems, Kuther [12] found the exciton g factor of an interrupted growth sample of $In_{0.60}Ga_{0.40}As/GaAs$ SAQDs to be 3.02. Interrupted growth causes the size distribution to decrease but the average size of the SAQDs to increase through the coagulation of small dots. Because the g factor is sensitive to its environment, the value of the exciton g factor is likely to be different to our samples because growth interrupted samples tend to relax the strain distribution around the dots. Bayer [10] also examined

growth interrupted $In_{0.60}Ga_{0.40}As/GaAs$ SAQDs and found three types of SAQDs with exciton g factors, -3.2, -0.7 and +0.6. Bayer [4] also looked at non-interrupted growth SAQDs grown on mesa structures, and found the exciton g factor to be -0.8. All the above samples were (100) grown. Therefore, a comparison with (100) grown samples may be made.

The exciton g factor for NU1652 seems quite large with a value of -5.1 in comparison to the above, however NU1658, with an exciton g factor of -0.9 lies in the range of those found by the other authors. However, the coverage parameter L, (see table 3.1) is the only difference between the two samples.

NU1652 has a coverage parameter of 1.1 nm which implies the SAQDs should be smaller than those found in NU1658 which is in agreement with the photoluminescence peak energy. The smaller dots though could have a larger g factor due to hybridisation with the wetting later in the hole states [15]. At the same rate, all the other exciton g factors seem to indicate that the exciton g factors for the (311) grown samples are roughly the same as the (100) grown samples. Therefore the effect of growth direction in these do not seem to affect the g factors significantly.

Henini [16] reported an arrow like shape in the [211] direction in (311) grown SAQDs. Due to the different confinement regimes in different directions, the polarisation of recombination luminescence has been shown to be shape dependent and elliptical light will be seen for a linear pump. However, this will only introduce a slight shift in the Zeeman splitting with magnetic field, and the exciton g factor is only influenced by the slope.

Therefore, this will have no effect on the measured values. The (311) samples were NU1654, NU1659, and NU1660. Comparison between the exciton g factors for NU1654 and NU1660 show the difference in coverage parameter L (see table 3.1) has little effect on the exciton g factor. However, comparison of NU1659 with NU1660 shows a significant difference in exciton g factor. The difference between the two samples was whether the growth was started on a Gallium or an Arsenic plane, and therefore the difference in surface chemistry translates into a difference in size and shape of quantum dot.

One other possibility for the asymmetry of the Zeeman splitting is that bi-excitons [12] [17], charged excitons [10] and excited states [18] cause a fictitious splitting. Because these tend to broaden the photoluminescence line asymmetrically, the measured Zeeman splitting value consists of a constant fictitious splitting value due to the asymmetry of the photoluminescence line plus the actual value of the Zeeman splitting. Bayer [10] found excited state emission even for the lowest excitation powers (100 μW).

However, Philip Marsden of Southampton University tried to find evidence of excited states by pumping with a very high pump density at 800nm and examined the spectra of the emitted radiation from the sample. (up to 62 mW at 2 ps with 80MHz repetition rate). He found no evidence of any excited states in any of the samples. Therefore, either it is not possible to observe excited states in these systems unlike that in reference [14] or, the excited states are already present in the low power spectra, but other relaxation mechanisms allow non-radiative recombination to become more favourable at high pump powers.

Kotlyar et al [21] made a theoretical analysis and experimental study of the Zeeman spin splittings and g factors in nano-structures. Their theory was based on the Kane model predicting a nonlinear increase in the exciton g factor with decreasing diameter of the dots. To add experimental weight to their theory, they needed a method to accurately manufacture quantum dots with an known diameter. They decided to use deep-etched $In_{10}Ga_{90}As/GaAs$ samples finding the diameter of the dots to overestimate the exciton g factor predicted by the theory by about 10% although the experimental data follows the theoretical curve well.

Fitting our measured g factors to their theoretical curve gives a value of 30 nm for NU1652 and all other samples have predicted diameters in excess of 50 nm due to their small measured g factors. From the available known data about our samples, we have 1 μm x 1 μm atomic force microscope images of samples NU1652 which show an average diameter of about 3 nm, and NU1654 with an average diameter of about 2 nm. The error in the samples g factors to average diameter when compared to the theory leads us to conclude that the different materials used and/or the method of manufacture of the quantum dots means they are not comparable.

We also have to give information on the possible In concentration in our samples. Fry et al [22] examined SAQDs using photo-current spectroscopy under an electric field with interesting results, contrary to the recent theoretical predictions, Fry et al found that the holes are localised above the electrons in SAQDs. This inverted alignment can only be explained if two conditions are fulfilled, the SAQDs must have a graded $In_{1-x}Ga_xAs$ composition with x decreasing from base to apex, and the pyramid needs to be severely truncated in order to obtain a dipole of the correct sign. We have

found no information on the variation with the g factor with increasing $In_{1-x}Ga_xAs$ composition.

Finally, Hendorfer et al [23] examined the g factors in strained $In_{1-x}Ga_xAs$ layers grown on GaAs. The electron g factor was found to go from -0.2 at x=0 to -16 at x=1 in the $< 100 >$ axis ($g_{||}$), and -0.2 at x=0 to -2 at x=1 perpendicular to the $< 100 >$ axis ($g_{\perp}$). For the same material making up our samples, Hendorfer et al found the g factors for $In_{0.5}Ga_{0.5}As$ to be -4 and -0.3 for $g_{||}$ and $g_{\perp}$ respectively.

4.5 Conclusion

We have measured the exciton g factors of a range of $In_{0.5}Ga_{0.5}As/GaAs$ SAQDs. The Zeeman splittings generally show a linear field dependence in the absence of a nuclear field and at low field values as expected in these systems. There are also non-linearities at higher fields due to field induced mixing between the optically active and the optically inactive exciton states. For circularly polarised light, the ellipticity of the recombination radiation shows that the spin relaxation time (τ_s) is greater than the recombination time (τ_r).

The method used to obtain the exciton g factors is both simple, reliable and accurate as shown by other authors [19][2][20], and has been used for many years successfully on quantum wells. However, it has not been possible to obtain the mechanism for the apparent Zeeman splitting in the SAQD samples due to the fact that, excited states and bi-exciton features would be hidden in the large photo-luminescence line-width of these

samples, and therefore the existence of these states could introduce a fictitious splitting value due to the asymmetry of the photo-luminescence line-profile, however, we have no evidence of the presence of any other states other than the ground state.

One possible improvement that could be made to the experiment is the fabrication of a mesa structure on top of the samples. This would facilitate the resolving of individual SAQDs spectroscopically, providing additional information on the electronic structure, which in turn would allow us to obtain the Zeeman splitting for individual SAQDs, without the additional contributions from either the other states from different SAQDs, or from other electronic states in the same SAQD.

Bibliography

[1] G. P. Flinn, R. T. Harley, M. J. Snelling, A. C. Tropper, T. M. Kerr, Semicond. Sci. Technol., **5**, 533 (1990)

[2] M.J. Snelling, Ph.D. Thesis, Optical Orientation in Quantum Wells, University of Southampton, (1991)

[3] M.R.S. bulletin, Various, February 1998

[4] M. Bayer, O. Stern, A. Kuther, and A. Forchel, Phys. Rev B, **61**, 7273 (2000)

[5] S. Gasiorowicz, Quantum Physics, Wiley International, (1974) (Chapter 14 Pages 235)

[6] H. W. van Kesteren, E. C. Cosman, and W. A. J. A. van der Poel, C. T. Foxon, Phys. Rev. B, **41**, 5283 (1990)

[7] E. Blackwood, M. J. Snelling, and R. T. Harley, S. R. Andrews, C. T. B. Foxon, Phys. Rev. B, **50**, 14246 (1994)

[8] E.L. Ivchenco and G.E. Pikus, Superlattices and other Heterostructures, Springer Series in Solid State Sciences, Volume 110 (1997)

[9] M. I. D'yakanov and V. I. Perel, Optical Orientaion, North Holland, (1984) (Pages 394)

[10] M. Bayer, A. Kuther, F. Schäfer, J. P. Reithmaier, and A. Forchel , Phys. Rev. B, **60**, 8481 (1999)

[11] Y. Toda S. Shinomori, K. Suzuki, and Y. Arakawa, Appl. Phys. Lett., **73**, 517 (1998)

[12] A. Kuther, M. Bayer, and A. Forchel, A. Gorbunov and V. B. Timofeev, F. Schäfer and J. P. Reithmaier, Phys. Rev. B., **58**, 7508 (1998)

[13] M. Bayer, A. Kuther, A. Forchel, A. Gorbunov, V. B. Timofeev, F. Schäfer, and J. P. Reithmaier, T. L. Reinecke and S. N. Walck, Phys.Rev Lett., **82**, 1748 (1999)

[14] L. R. Wilson, D. J. Mowbray, M. S. Skolnick, M. Morifuji, M. J. Steer, I. A. Larkin and M. Hopkinson, Phys Rev. B., **57**, 2073 (1998)

[15] M. Grundmann, O. Steir, and B. Bimberg. Phys. Rev. B, **52**, 11969 (1995)

[16] M. Henini, S. Sanguinetti, S. C. Fortina, E. Grilli, M. Guzzi, G. Panzarini, L. C. Andreani, M. D. Upward, P. Moriaty, P. H. Beton, and L. Eaves, Phys. Rev. B, **57**, 6815 (1998)

[17] F. Findeis et al, Phys. Rev. B, **61**, 10579 (2000)

[18] D. J. Mowbray et al, Optical and Magneto-optical Spectroscopy of InAs/GaAs Self-Organised Quantum Dots, Proc. Semiconductor Science and Technology, (1998)

[19] E. Blackwood, Ph.D. Thesis, Spin-polarised Dynamics in quantum wells, University of Southampton, (1993)

[20] N. J. Traynor, Ph.D. Thesis, Magneto-optics of excitons in quantum wells, University of Southampton, (1996)

[21] R. Kotlar and T. L. Reinecke, Phys Rev B., **63**, 085310

[22] P. W. Fry, I. E. Itskevich, D. J. Mowbray, M. S. Skolnick, J.J. Finley, J. A. Barker, E. P. O'Reilly, L. R. Wilson, I. A. Larkin, P. A. Maksym, M. Hopkinson, M. Al-Khafaji, J. P. R. David, A. G. Cullis, G. Hill and J. C. Clark, Phys Rev Lett., **84**, 733 (2000)

[23] G. Hendorfer and J. Schneider, Semicond. Sci. Technol. **6**, 595 (1991)

Chapter 5

The Hanle Effect in $In_{0.5}Ga_{0.5}As$ Quantum Dots

5.1 Introduction

Most of the impetus in measuring the oblique Hanle effect was to see whether nuclear effects were indeed possible in our samples, and if so possibly provide an explanation for the asymmetrical shape in the Zeeman splitting measurements. It also would provide a good method to find which samples would be suitable for the ODNMR experiments. To our knowledge, this is the first investigation of the Hanle effect in $In_{0.5}Ga_{0.5}As$-/GaAs SAQDs. Measurements on the Hanle depolarisation allow a number of material parameters to be ascertained: The sign of the electron g factor may be determined [6] and if the electron g factor is known, the spin relaxation and recombination times (τ_s and τ_r respectively) may also be calculated.

The transverse Hanle effect is obtained by inducing optical orientation in the conduction band electrons of the GaAs bulk. This produces a non-equilibrium spin population in the SAQDs after non-radiative relaxation and together with an applied magnetic field orientated perpendicular to the growth direction [2], allows the depolarisation of the conduction spin electrons with applied magnetic field to be studied.

It was not possible to obtain the electronic g factor directly as most methods used to separate the electron and hole g factors from the exciton g factor require resonant pumping [2]. However, Dr. Philip Dawson of UMIST has measured the recombination time for one of our samples, namely the (311) oriented $In_{0.5}Ga_{0.5}As$ sample NU1654 [3], and together with the electron g factor measured by Bayer [4], it was possible to obtain the initial

spin polarisation state (S_i) in this sample. With S_i and τ_r known, it was possible to ascertain the spin relaxation time (τ_s) according to equation 5.11.

Ideally, the experiment should be resonantly pumped however, this proved impossible due to zero Stokes shift in the SAQDs [5] [6] [7] [8]. The incident radiation was tuned to 800 nm in order to ensure accurate $\sigma_{\pm}$ polarisation for the same reasons as those given in the Zeeman splitting chapter. Due to the fact that it is not possible to resonantly pump the SAQDs, we had to rely on the previously observed result from the Zeeman splitting measurements: that the spin relaxation time is slower than the recombination time and therefore, the exciton states in the SAQDs are spin polarised at recombination.

It should be noted that it is not impossible to induce resonant or near resonant excitation in SAQDs. Adler used two photon absorption [9] to observe phonon relaxation from the first excited state to the ground state, and observed the ground state transition recombination time to be 600 ps, (for a sample temperature below 50K). Other methods have included the embedding of the SAQD's within a planar micro-cavity whose resonance mode, is tuned to the ground state transition of the SAQD's [10]. Other methods have included the resonant pumping of excited states which produces a nearly resonant relaxation condition in the ground state of SAQD's, and two colour, two photon absorption [11].

Once we recorded the transverse Hanle depolarisation of the conduction electron spin system subject to a transverse magnetic field, we recorded the oblique Hanle effect for various angles (θ) between the incident radi-

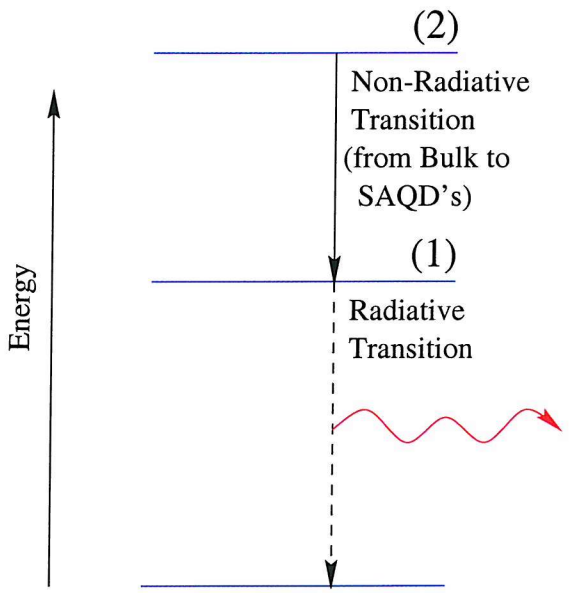

Figure 5.1: **Diagram showing the two level system assumed to be relevant to the electronic structure in our SAQD's.**

ation direction and the magnetic field direction. The oblique Hanle effect shows a shift in the Lorentzian maximum due to the existence of a nuclear field. Measurements of this shift of the Lorentzian maximum from the zero field allows the observation of the maximum average hyperfine nuclear field B_N [2].

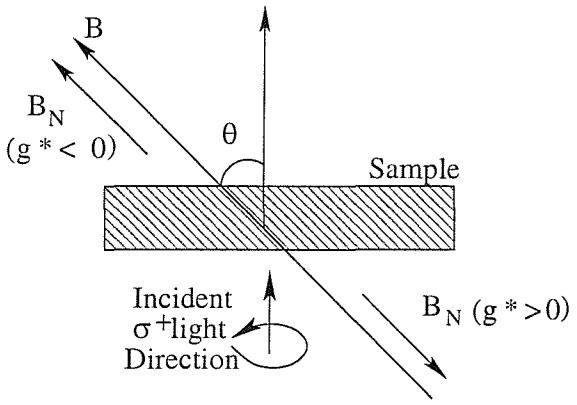

Figure 5.2: **Diagram showing the orientation of the sample with respect to the exciting light and the external field. The direction of the nuclear field B_N is clearly shown with the corresponding sign of the electronic g factor (g^*)**

5.2 Theory

The transverse Hanle effect has already been explained in the theoretical chapter (chapter 2). It shows that the de-polarisation of the electronic spin in an increasing magnetic field has a Lorentzian line-profle. However, the non-resonant excitation of the sample modifies the Lorentzian line-profile of the Hanle curve (as given in equation 2.15) [12].

The non-resonant Hanle equation is derived below for a two level system which we assume is a similar system to our SAQD's. Electrons are pumped into state 1 and luminescence is observed from state 2, this is shown in figure 5.1. The electron gets from state 1 to state 2 via a non-radiative transition. Therefore, the equations of motion describing the average spin of electrons in a magnetic field [12] is:

$$\frac{dS^{(1)}}{dt} = \Omega_{(1)} \times S^{(1)} - \frac{S^{(1)}}{\tau_s^{(1)}} + \frac{S_0}{\tau_r^{(1)}} \tag{5.1}$$

for level 1, and for level 2:

$$\frac{dS^{(2)}}{dt} = \Omega_{(2)} \times S^{(2)} - \frac{S^{(2)}}{\tau_s^{(2)}} + \frac{S^{(1)}}{\tau_r^{(2)}} \tag{5.2}$$

where $\Omega_{(i)}$, $\tau_s^{(i)}$ and $\tau_r^{(i)}$ are the Larmor frequency, the spin lifetime and the recombination lifetime of state i. Assuming $\Omega_{(i)}$ is perpendicular to S_0, then the stationary state solution ($\frac{dS}{dt} = 0$) in the growth direction (z) becomes:

$$S_z^{(2)}(B) = S^{(2)}(0) Re \frac{1}{(1 + i\Omega_{(1)}\tau_s^{(1)})(1 + i\Omega_{(2)}\tau_s^{(2)})} \tag{5.3}$$

where

$$S^{(2)}(0) = \frac{\tau_s^{(2)}}{\tau_r^{(2)}} \frac{\tau_s^{(1)}}{\tau_r^{(1)}} S_0 \tag{5.4}$$

Here it should be noted that the final spin state of the electron is a function of both $\tau_s^{(1)}$ and $\tau_s^{(2)}$ and it is this that changes the line shape from the Lorentzian line profile. Equation 5.3 may then be reduced to:

$$S_z^{(2)}(B) = S^{(2)}(0) \frac{1 - \Omega_{(1)}\tau_s^{(1)}\Omega_{(2)}\tau_s^{(2)}}{(1 + (\Omega_{(1)}\tau_s^{(2)})^2)(1 + (\Omega_{(2)}\tau_s^{(2)})^2)} \tag{5.5}$$

which is the Hanle equation for a cascade process. Generalising the above equation to several energy levels, we obtain:

$$S_z^{(n)}(B) = S^{(n)}(0) Re \prod_{k=1}^{n} \frac{1}{1 + i\Omega_{(k)}\tau_s^{(k)}} \tag{5.6}$$

where n is the number of levels in the cascade process and the multiplication is over all states involved in the cascade.

$$S_z^{(n)}(0) = S_0 \prod_{k=1}^{n} \frac{\tau_s^{(k)}}{\tau_r^{(k)}} \tag{5.7}$$

It is interesting to examine the Hanle curve for a large number of steps n because it deviates significantly from the simple resonant Lorentzian case. Using the identity $1 + i\Omega_{(k)}\tau_s^{(k)} = e^{ln(1+i\Omega_{(k)}\tau_s^{(k)})}$ and expanding the logarithm in terms of $\Omega_{(k)}\tau_s^{(k)}$, keeping only the first term in the expansion and assuming all $\Omega_{(k)}$ are equal, we obtain from equation 5.6:

$$S_z(B) = S(0)\cos(\Omega t_o) \tag{5.8}$$

with

$$S(0) = S_0 \exp(-\frac{t_0}{\tau_s^k}) \tag{5.9}$$

where $t_0 = \sum_{k=1}^{n} \tau_k$, the total recombination time of an electron from initial to final transition. Here we have also assumed $\tau_s >> \tau_r$. Therefore, for a large number of unknown of electronic levels, the Hanle curve goes from a Lorentzian to a cosine line-shape as a function of magnetic field, and will therefore allow us to tell whether the cascade in our measurements has a large number of transitions or not.

For these experiments we are also interested in obtaining the spin relaxation time (τ_s). This is usually accomplished by means of the measurement of the half width at half maximum (HWHM) of the transverse Hanle curve ($\Delta B_{\frac{1}{2}}$), and the value of the polarisation at zero field with resonant pumping conditions, together with the electron g factor, allows calculation of both the recombination time (τ_r) and the spin relaxation time (τ_s).

We have not been able to measure the electronic g factor directly, however we have been able to ascertain that the electron g factor measured by Bayer et al [4] is probably similar to ours as they studied similar SAQD's to us. We therefore assume that the electron g factor in our samples are similar to those studied by Bayer et al. It is not possible to obtain all the necessary parameters in the cascade process to obtain τ_r and τ_s, however, if we can obtain the initial spin state of electrons as they enter the SAQD's, we can then obtain a measure of the spin relaxation time by using the equation for the resonant pumped Hanle effect (equation 2.15).

We therefore have to obtain the spin orientation of the electrons as they

relax into the SAQD's. Using equations 2.11, 2.15 and 2.16 we find:

$$S_i = \frac{\tau_r g^* \mu_B \Delta B_{\frac{1}{2}} S_0}{\hbar} \tag{5.10}$$

and

$$\tau_s = \frac{\hbar}{g^* \mu_B \Delta B_{\frac{1}{2}}} \left(\frac{S_i}{S_0}\right) \tag{5.11}$$

Substituting S_i into the above equation, (equations 5.10 and 5.11) we can therefore obtain τ_s. For a magnetic field direction other than the perpendicular to the samples growth direction, and a magnitude greater than the average magnitude of the local nuclear fields, we find the hyperfine interaction polarises the nuclear spin system which then acts back onto the electrons changing the recombination polarisation. In the oblique Hanle effect, we find a shift the Lorentzian peak by $-B_N \cos(\theta)$, due to compensation of the external field by the nuclear field. There is also a sharp peak at zero field due to the random nature of the local nuclear fields. This is shown in equation 2.32, which implies that by measurement of the Lorentzian maxima as a function of the cosine of the angle between the magnetic field direction, and the initial electronic spin direction, the maximum average hyperfine nuclear field (B_N) may be obtained.

Examination of figure 5.2 shows that the shift of the Lorentzian peak gives information on the sign of the electronic g factor. We have assumed for all the following analysis that the spin relaxation and recombination times for all transitions other than the final radiative transition are negligible in comparison to the spin relaxation and recombination times in the SAQD's. There is some evidence to support this, Yuan [13] measured the recombination of many particle states using frequency up-conversion, at a delay of

20ps, the dot occupancy had already built up and a strong filling of SAQD levels gave rise to four photoluminescence peaks. Therefore we assume that the transition into the SAQD's is very quick (faster than 20ps).

5.3 Experimental Details

Details of the experimental apparatus have already been given in chapter 3. In order to ensure that the incident radiation was accurately positioned at 90° to the magnetic field and parallel to the growth axis of the sample, the reflection of the incident beam was used to position the sample relative to the beam, then a protractor set onto the sample stick was used to change this angle. The magnetic field was then set at 90° to the sample by looking at successive maxima of the Hanle effect curve in the absence of a nuclear field.

We first examined the transverse Hanle effect in each sample at a temperature of 10K. Pump light was right circularly polarised to ensure easy comparison with the Zeeman splitting data. If the sample showed an adequate transverse Hanle signal, the oblique Hanle effect was then recorded. For the oblique Hanle effect, the sample was orientated in the plane, parallel to the external magnetic field and the exciting beam. This induced a nuclear field B_N as shown in equations 2.35.

For the transverse Hanle effect, we require the nuclear field to be suppressed. This is accomplished by positioning as accurately as possible the magnetic field with respect to the exciting beam. We require the presence of a nuclear field for the oblique Hanle effect however, and therefore we

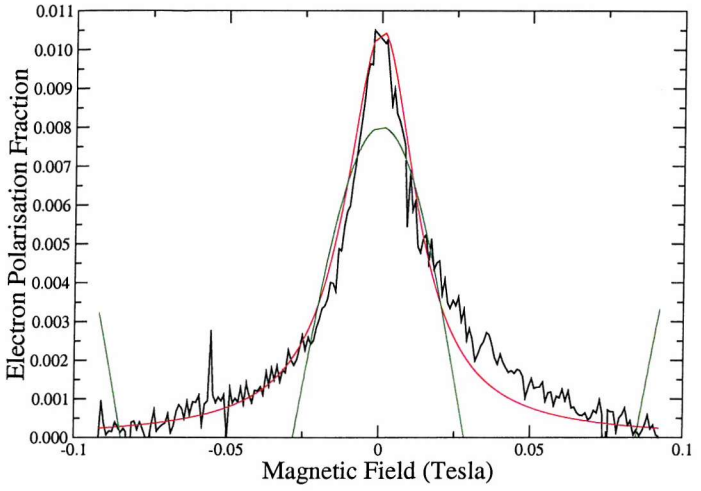

Figure 5.3: **Diagram showing the transverse Hanle effect from sample NU1660. The red line is a Lorentzian curve fitted to the data, while the green line is a cosine function fitted to the data. The reasonable fit to the Lorentzian line profile implies very few transitions occur in the cascade process before recombination.**

change the angle between the incident light beam and the external magnetic field to induce one. Data analysis was accomplished in real time for detector response at the sum and difference frequencies. Due to the fact that the time constant of the lock-in was so long (300 ms), we had time to analyse the data in real time. The sum and difference signals were converted to the polarisation as given by equation 2.8 and recorded to disk, together with the electromagnet driving current and the magnetic field strength, (a hall probe, situated at one side of the cryostat allowed continuous monitoring of the magnetic field).

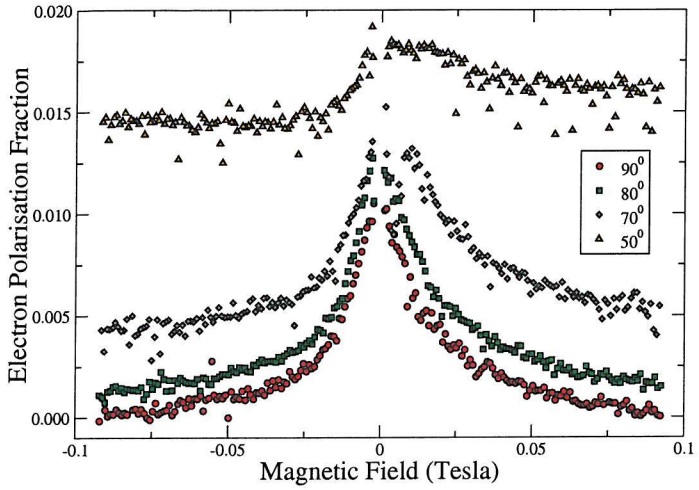

Figure 5.4: **Diagram showing some oblique Hanle curves for $\theta < 90$ from sample NU1660.**

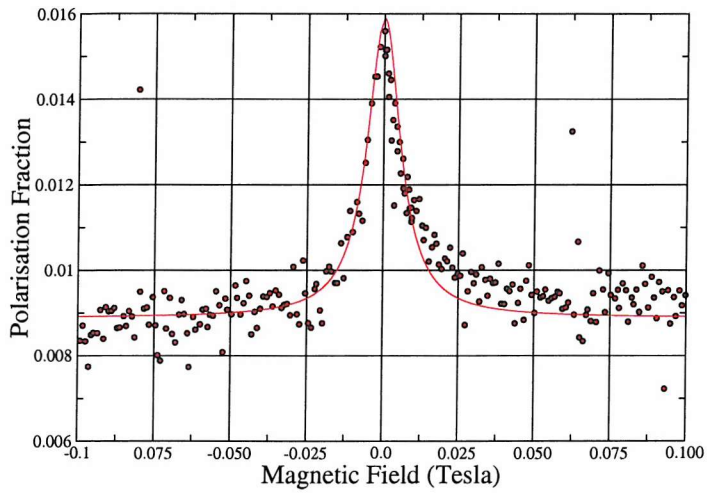

Figure 5.5: **Diagram showing the transverse Hanle effect from sample NU1654, the fit (red line) is a Lorentzian curve plus a constant to the data.**

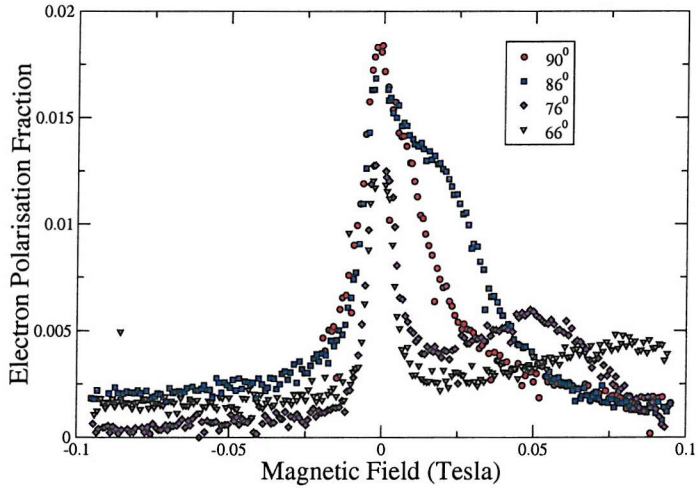

Figure 5.6: **Diagram of some selected Hanle curves in the presence of a nuclear field for $\theta < 90$ from sample NU1654.**

5.4 Results

All samples showed some response at zero field, however, we only obtained sufficient polarisation in zero field in two samples, namely NU1654 and NU1660 to record the transverse Hanle effect. We present the results from each sample in turn.

5.4.1 The Hanle Effect in NU1660

The results of the transverse Hanle measurements are shown in figure 5.3. The red line is a Lorentzian fit to the data and the green, a cosine function fitted to to the data. The reasonably good fit to the Lorentzian line profile indicates that the number of electronic transitions the electrons pass through in the cascade process is small. The Lorentzian line profile fitted was as follows:

$$y = \frac{A0}{(1 + (xA1)^2)} \tag{5.12}$$

where A0 (represents the inital polarisation fraction), and A1 (represents the Lamor frequency) were fitting parameters. We obtained $A0 = (10.5 \pm 0.8) \times 10^{-3}$ and $A1 = 71 \pm 3\ \mathrm{s}^{-1}$ for the parameters. However, because we do not have any information on the recombination time, the spin relaxation time or the polarisation state in the SAQD's, we can not obtain any further information.

The oblique Hanle effect was then examined, with the results shown in figure 5.4. The curve shows that for decreasing values of θ, the polarisa-

tion tends to the polarisation at zero magnetic field with no shift in the peak, an explanation for this may be in reference [10] who found that the spin relaxation in InAs/GaAs SAQD's is quenched. What is meant by spin relaxation being quenched is that the spin relaxation is so long in comparason to the electron lifetime that for all purposes, there is no decrease in the electron spin during the electron lifetime. Therefore the electron depolarisation with magnetic field is suppressed and the Hanle curve tends to a constant.

5.4.2 The Hanle Effect in NU1654

Following on from the previous sample, we obtained the transverse Hanle curve for sample NU1654, this is shown in figure 5.5. The Hanle depolarisation curve has a rather strange peak in that it proved impossible to fit either a Lorentzian or a cosine function to the data on its own, however, assuming a constant offset in the data, a Lorentzian plus constant seemed the best fit and is shown as the red line in figure 5.5. The fitted lineshape is shown below:

$$y = \frac{A0}{(1 + (A1x)^2)} + A2 \tag{5.13}$$

where A0 (initial spin polarisation), A1 (the Lamor angular frequency) and A2 (offset in the initial spin polarisation) are fitting parameters. We obtained the following results for the fit: $A0 = (7 \pm 0.2) \times 10^{-3}$, $A1 = 7.55 \pm 0.05\ s^{-1}$, and $A2 = (8.9 \pm 0.2) \times 10^{-3}$. As with NU1660, the first result is that the curve is far closer to a Lorentzian than a cosine type line shape, although with an offset on the data, and therefore there are very

few transitions between the electrons entering the SAQD's and being excited into the conduction band of GaAs bulk.

The HWHM ($\Delta B_{\frac{1}{2}}$) for the transverse Hanle effect was measured to be 7.0 ± 0.2 mT, and the maximum polarisation of the Hanle curve, S_o: 0.018 ± 0.006. Together with the recombination time measured by Dawson to be 950×10^{-9} ps, and assuming the measured g factor in reference [4], to be valid for these samples, we have calculated the spin relaxation time τ_s to be (3.0 ± 0.2) ns.

The oblique Hanle curve however seems very similar to quantum wells in that, with decreasing angle θ, the maxima is increasingly shift in field, see figure 5.6. This has allowed us to obtain the largest maximum average nuclear field, and is accomplished by measuring the shift of the Lorentzian maxima, as a function of the cosine of the angle between the incident light beam, and the magnetic field direction, θ. We then fitted a straight line to the data shown in figure 5.7. The fit obtained was:

$$y = 0.205cos(\theta) + 0.001 \tag{5.14}$$

with an error of the order 0.001 Tesla in the slope of the graph. We therefore estimate the maximum nuclear field B_N to be 0.205 ± 0.001 Tesla.

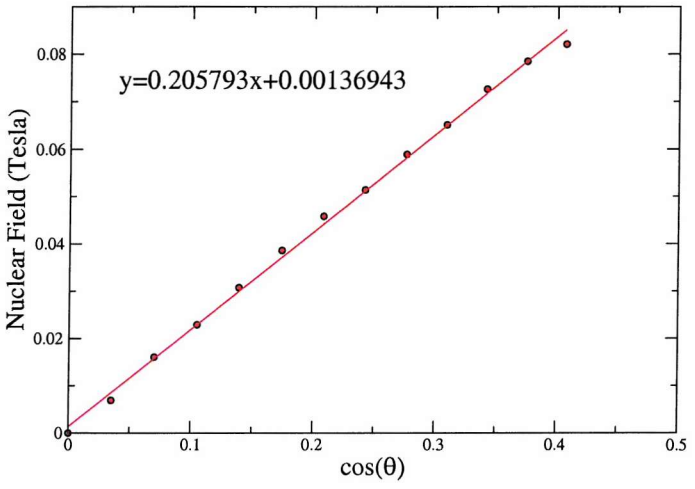

Figure 5.7: **Diagram showing peak of the de-polarisation shift as a function of the cosine of the angle between the magnetic field B, and the incident light direction. The red line is a least squares line-fit to the data, the fitted parameters of which are shown in the insert**

5.5 Discussion

The fact that we find a nuclear polarisation signal implies the asymmetry found in the Zeeman splitting is indeed a nuclear effect and not just the existence of excited states in the envelope of the photoluminescence lineshape.

In quantum wells, the dynamics of carriers confined with allowed momentum in at least the planar directions (x,y) leads to rapid thermalisation with the lattice. Therefore, in quantum wells, we find radiative recombination predominantly originating in the lowest available states, and we find the associated fast spin relaxation times.

However, due to the fact that the zero dimensional density of states in SAQD's imposes more severe restrictions on thermalisation [14] [15], we find the observation of excited states in photoluminescence spectra [16] [17] [8]. These excited states are seen at very low excitation densities due to the restricted intersubband level relaxation rates [18]. This so called phonon bottleneck occurs between levels predominantly which are separated by no more than a few meV from the longitudinal optic, or the longitudinal acoustic phonon energies [19].

Therefore we expect the spin relaxation time to be enhanced in systems of lower dimensionality than quantum wells. The spin relaxation time has been measured in III-V SAQD's by Paillard [10]. Paillard measured the spin relaxation time in InAs/GaAs SAQD's embedded in a planar GaAs micro-cavity, with the cavity mode tuned to the ground state of the SAQD's. Therefore it is possible for the ground state to be resonantly

pumped and the photoluminescence from the sample to be distinguished from the backscattered light.

Paillard [10] never observe, at any temperature, any temporal decay of the linear or circular luminescence polarisation, regardless of the excitation polarisation and magnetic field value. Therefore, this is strong evidence of carrier spin freezing in these systems.

We have found that the spin relaxation time is considerably longer than the recombination time in our InGaAs/GaAs systems, which confirms that the spin state of conduction electrons is very long lived. What is more, is that the SAQD's in reference [10] are of a different chemical composition (InAs/GaAs) and therefore, this seems to be a general property of these systems. The constant value of spin implies that spin relaxation in SAQD's is indeed suppressed.

This also gives an explanation for the strange oblique Hanle curves in both sample NU1654 and NU1660. As spin relaxation mechanisms are suppressed, the positive feedback mechanism in the hyperfine interaction would feed back on the electrons and force a spin freezing effect. Therefore we find an almost constant value of polarisation in the recombination radiation.

5.6 Conclusion

We have found the sign of the electron g factor in the two samples to be negative. For the transverse Hanle curves, we find a similar strange be-

haviour which we attribute to the suppression of spin relaxation for these systems in low excitation powers. This is not unexpected and has been theoretically investigated by Benisty [14] [20] who predicted a low scattering rate in SAQD's and therefore, a corresponding long spin relaxation time.

Paillard [11] is the only experimental paper dealing with the spin relaxation time in SAQD's, and we find a similar result in that the spin relaxation time is much longer than the recombination time.

For sample NU1654, we find the spin relaxation time to be $(3.0\pm0.2)\times10^{-9}$ seconds assuming a recombination time of 950×10^{-12} seconds. The maximum average nuclear field in NU1654 was found to be 0.205 ± 0.001 Tesla. No quantitative results were found for sample NU1660 due to the strange behaviour of the oblique Hanle peaks and the lack of the value of the recombination time.

Bibliography

[1] Daniel J. Guerrier, Ph.D. Thesis, Optically Nuclear Detected Magnetic Resonance in Semiconductors, University of Southampton (1997)

[2] M. I. D'Yakanov and V. I. Perel, Ed. F. Meier and B. P. Zakharchenya, Optical Orientation, North Holland (1984)

[3] Philip Dawson, Private Communication.

[4] M. Bayer, O. Stern, A. Kuther, and A. Forchel, Phys. Rev B, **61**, 7273 (2000).

[5] M. J. Steer, D. J. Mowbray, W. R. Tribe, M. S. Skolinck, M. D. Sturge, M. Hopkinson, A. G. Cullis, C. R. Whitehouse, and R. Murray, Phys. Rev. B, **54**, 17738 (1996)

[6] A. Efros, M. Rosen, M. Kuno, M. Nirmal, D. J. Norris, and M. Bawendi, Phys. Rev. B, **54**, 4843 (1996)

[7] M. Bayer, A. Kuther, A. Forchel, A. Gorbonov, V. B. Timofeev, F. Schafer, J. P. Reithmaier, T. L. Reinecke, and S. N. Walck, Phys. Rev. Lett., **82**, 1748 (1999)

[8] D. J. Mowbray et al, Optical and Magneto-optical Spectroscopy of InAs/GaAs Self-Organised Quantum Dots, Proc. Semiconductor Science and Technology (1998).

[9] F. Adler, M. Geiger, A. Bauknecht, D. Haase, P. Ernst, A. Dornen, and F. Scholz, J. Appl. Phys., **83**, 1631 (1998).

[10] M. Paillard, X. Marie, P. Renucci, T. Amand, A. Jebeli, and J. M. Gerard, Phys. Rev. Lett., **86**, 1634 (2001).

[11] M. Paillard, X. Marie, E. Vanelle, T. Amand, V. K. Kalevich, A. R. Kovsh, A. E. Zhukov and V. M. Ustnov, Appl. Phys. Lett., **76**, 76 (2000)

[12] F. Meier and B.P. Zakharchenya, Optical Orientation, North Holland, (1984) (Chapter 2 page 40)

[13] Z. L. Yuan, E. R. A. D. Foo, J. F. Ryan, D. J. Mowbray, M. S. Skolnick, and M. Hopkinson, Phys. Stat. Sol., **224**, 409 (2001)

[14] H. Benisty, C. M. Sotomayer-Torres, and C. Weisbuch, Phys .Rev. B, **44**, 10945 (1991)

[15] M. Grundmann, O. Stier, and D. Bimberg, Phys. Rev. B, **52**, 11969 (1995)

[16] A. Chavez-Pirson, J. Temmyo, H. Kamanda, H. Gotoh, and H. Ando, Appl. Phys. Lett., **72**, 3494 (1998)

[17] M. Bayer, T. Gutbrod, A. Forchel, V. D. Kulakovskii, A. Gorbunov, M. Michel, R. Steffen, and K. H. Wang, Phys. Rev. B, **58**, 4740 (1998)

[18] K. Brunner, U. Brokkelmann, G. Abstreiter, M. Walther, G. Bohm, G. Trankle, and G. Weimann, Phys. Rev. Lett., **69**, 3216 (1992)

[19] R. Heitz, M. Grundmann, N. N. Ledentsov, L. Eckey, M. Veit, D. Bimberg, V. M. Ustinov, A. Yu Egorov, A. E. Zhukov, P. S. Pop'ev and Zh. I. Alferov, Appl. Phys. Lett., **68**, 361 (1996)

[20] H. Benisty, Phys. Rev. B, **51**, 13281 (1995)

Chapter 6

Oblique Field ODNMR in $In_{0.5}Ga_{0.5}As$ Quantum Dots

6.1 Introduction

The history of ODNMR in SAQDs is a very brief one, to the best of our knowledge, only one author has examined nuclear effects in zero dimensional quantum systems [1]. Gammon et al measured the Overhauser shift [2] [3] in the photoluminescence spectra in the presence of a radio frequency field. Set to the resonance frequency of one of the nuclear species that make up the sample, the presence of the radio frequency field tends to suppress the overall nuclear polarisation, and due to the existence of the hyperfine interaction, feedback to the electronic spin system, induces a change in the photoluminescence polarisation. Therefore it is possible to record the photoluminescence spectrum in the presence and absence of the radio frequency field, and the shift of the photoluminescence lineshape gives a measure of the nuclear species polarised via the hyperfine effect in the sample. This is called the Overhauser shift and in this way, he identified all the nuclear species that make up the sample.

The sample consisted of quantum dots formed from width fluctuations in an AlGaAs/GaAs quantum well. Because the fluctuations tend to weakly confine electrons in the plane of the semiconductor layers, and strong confinement occurs in the growth direction of the quantum wells, electrons tend to show optical properties similar to that expected from a zero dimensional structure.

In this chapter, we present data obtained from examining ODNMR in SAQDs using the oblique ODNMR technique. We were limited to one sample as it was the only one that showed an ODNMR signal due we believe to the resolution of our apparatus. This sample was NU1654, a

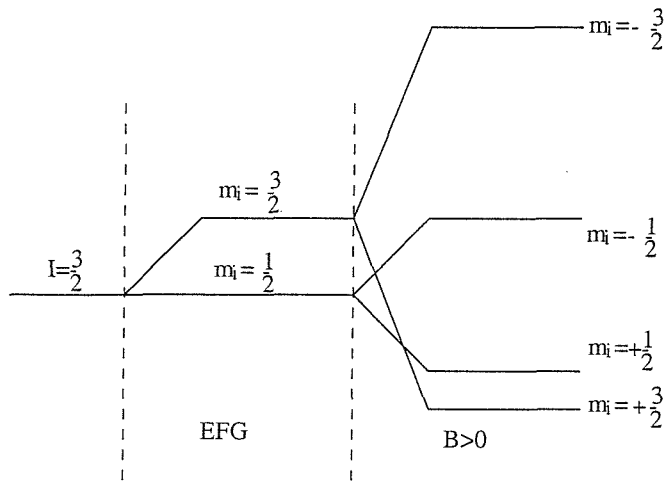

Figure 6.1: **Diagram showing the spin fine structure of a nucleus for $I = \frac{3}{2}$ in the presence of an electric field gradient and external magnetic field. The degeneracy of the nuclear species may be removed as shown by means of an external magnetic field or an electric field gradient.**

(311) grown $In_{0.5}Ga_{0.5}As/GaAs$ SAQD sample. It was also the sample that showed the largest Hanle signal (see chapter 5). After a discussion on the techniques and differences between adiabatic fast passage, and the oblique ODNMR method, a number of points are discussed with reference to the experimental setup. We then present the experimental results followed by a discussion on those results. Finally the conclusion brings the chapter to a close.

6.2 Experimental Details and Theory

The technique traditionally used to detect NMR in semiconductors is the adiabatic fast passage method [12]. It is this method that was used to record the first ODNMR spectrum in $Al_{0.2}Ga_{0.8}As$ by Ekimov et al [4] in 1972. In low dimensional semiconductor heterostructures, the first observation of ODNMR in quantum wells was made by Flinn [5]. He studied a series of type I $GaAs/Al_{0.3}Ga_{0.7}As$ quantum wells using the adiabatic fast passage method, and later examined many of the methods different characteristics.

Later Guerrier [6] found that the oblique ODNMR technique lent itself more readily to the study of low dimensional systems. He then went on to study quadrapole resonances in quantum wells, and was able to demonstrate the correlation between strain and splitting of the quadrapole resonance peak of ^{75}As in GaAs/AlGaAs quantum wells [7].

The nuclear fine structure of an atom may be affected by both electric field gradients (for atoms with a nuclear spin $I > \frac{1}{2}$, which then possess a quadrapole moment [8]), and external magnetic fields. This is pictorially shown in figure 6.1 for a nucleus of $I = \frac{3}{2}$.

Electric field gradients effect the nuclear fine structure by lifting the degeneracy of the $I_z = \frac{3}{2}$ and $I_z = \frac{1}{2}$ nuclear spin states. This occurs due to the replacement of gallium by indium in the GaAs lattice [9] [10] which reduces the crystal symmetry, and in particular due to the differing nuclear electron-negativities of the bonding atoms, disturbs the symmetry of the valence electron states near the arsenic sites. This produces an electric

field gradient (efg) at the indium–arsenic bond sites. Because gallium and arsenic are very similar in structure [11], the quadrapole interaction is negligible for these bonds and are generally considered to be unperturbed [9]. A further application of an external magnetic field then lifts the $\pm\frac{3}{2}$ and $\pm\frac{1}{2}$ nuclear spin states as shown in figure 6.1.

As mentioned previously, there are two methods used to detect NMR in semiconductors, however, they both rely on the same basic principle which is given below: The degeneracy of the nuclear spin states is lifted by means of an external magnetic field, allowing the existence of a nuclear spin temperature under conditions of optical orientation.

A radio frequency field is then applied at an angle of 90^o to the external magnetic field direction, and it is this field that is used to induce nuclear transitions at the resonance frequency of one of the nuclear isotopes. During resonance, the nuclear spin temperature tends to undergo a change, however, the method used to change the nuclear spin temperature differ for the two methods [12].

This is because during resonance with one of the nuclear species, the radio frequency field induces magnetic dipole transitions when the energy between nuclear levels is equal to the resonance frequency given by [13]:

$$\hbar\omega_o = \hbar\gamma_N B_{ext} \tag{6.1}$$

where γ_N is the gyro-magnetic ratio of isotope N, and B_{ext} is the external magnetic field. Radio frequency transitions during resonance are illustrated in figure 6.2.

Hyperfine coupling between the nuclear and electronic spin system then acts back on the conduction electron spin states, resulting in a change in the polarisation of recombination radiation emitted from the sample. This may be measured to detect the change in the nuclear spin temperature by measuring the photoluminescence polarisation state.

A further requirement is that the local nuclear fields (B_L) must be smaller than the maximum value of the radio frequency magnetic field (B_I) otherwise nuclear orientation becomes subject to dipole–dipole relaxation and thus nuclear polarisation is quickly suppressed [14].

ODNMR has a number of advantages over conventional NMR, [6] the first being that unlike conventional NMR, ODNMR can detect resonances in a very small region of space because optical orientation tends to cause large non-thermal nuclear population distributions.

Nuclei tend to relax via simultaneous interchange of spin angular momenta and therefore this tends to lead to the surrounding nuclei becoming slowly oriented, this process is called spin diffusion. Therefore it is possible to measure nuclear spin diffusion in isolation in these samples. However, this has not been proved in SAQDs where the large strain fields may suppress spin diffusion across barriers.

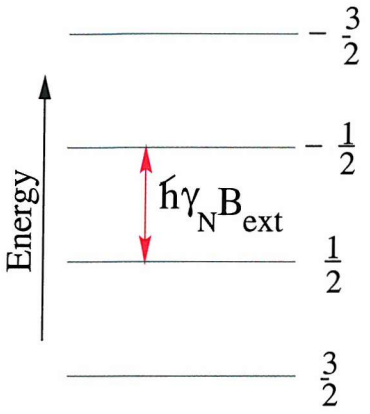

Figure 6.2: **Diagram showing the spin levels of a nucleus for $I = \frac{3}{2}$. The degeneracy of the nuclear species may be removed as shown by means of an external magnetic field. The application of a radio frequency magnetic field gives a resonance condition for transitions between different nuclear spin states m_I as $\hbar\gamma_N B_{ext}$.**

6.2.1 Adiabatic Fast Passage

The adiabatic fast passage technique [15] is quite straightforward in that an external magnetic field is orientated parallel to the exciting light beam, (and therefore parallel to the electron polarisation), and the growth direction of the SAQD sample, therefore according to equation 2.24, the nuclear field attains its maximum value.

A radio frequency field is then orientated at 90^o to the exciting light direction. Resonance between the radio frequency magnetic field and the nuclear spin system is achieved by sweeping the radio frequency magnetic field in a fixed external longitudinal field, or visa versa: using a fixed radio frequency field and sweeping the external longitudinal magnetic field.

A full treatment of the theoretical aspects of adiabatic fast passage is given

in reference [16], here we present a visual model of the phenomenon. Off resonance, the nuclear field is orientated parallel to the exciting light beam and the external magnetic field as shown in figure 6.3, and represented by (A), having attained its maximum value after time t.

On resonance, the nuclear spins that are resonant with the radio frequency field drive the nuclear spin, and therefore its associated nuclear field through 180^o. This occurs when the difference in the energy between nuclear spin states, becomes equal to the energy of the radio frequency oscillations and is shown in (B) of figure 6.3.

Therefore, it is simpler to view the passage through resonance from a co-ordinate system that is rotating with the radio frequency, rather than from the fixed laboratory frame, (a full derivation may be obtained in reference [17]). Since the radio frequency magnetic field is orientated at 90^o to the nuclear polarisation, initially, from the viewpoint of the rotating frame, all nuclear spins are pointing in the z direction, parallel to the growth direction of the sample.

As resonance is reached, and assuming that the radio frequency is in the x direction of the rotating frame, we see the resonant spins form an angle θ with the non-resonant nuclear spins given by [18] [19]:

$$\theta = \arctan\left(\frac{B_I}{\frac{\omega_o}{\gamma_N} - B_{ext}}\right) \tag{6.2}$$

where B_I is the radio frequency magnetic field maximum, and has to be greater than the local nuclear fields (B_L). On resonance, the radio frequency field drives the resonant nuclear spins through a rotation of 180^o. Nuclear spins are therefore at an angle θ to the non-resonant nuclear spins.

The vector sum of fields deviates during resonance and forces an increase in nuclear spin temperature though the oblique Hanle effect.

Back in the laboratory frame, the electron spin system experiences a total field consisting of the external field B_{ext}, the non-resonant nuclear spins ($\sum B_N$), and the resonant field (B_n) that swings out towards the x–y plane. Thus the total nuclear field deviates from the growth axis of the sample, and the oblique Hanle effect causes a change in the electron polarisation as the radio frequency, (ω_o) is swept through resonance. After resonance, the nuclear spins are completely disordered and start to reorient under optical orientation.

As with the Hanle effect, the sign of the electronic g factor, nuclear gyromagnetic ratio, and the handedness of the polarisation of pump light influence the manner in which the nuclear spins add or subtract from the total nuclear orientation during the passage through resonance. The two extremes are shown in figure 6.3 where it is obvious that the situation where the external field is orientated anti-parallel to the nuclear polarisation direction, produces a greater de-polarisation.

It should be noted that a number of factors influence the line-shape of the resonance signal and passage through resonance is not dictated by the nature of nuclear de-polarisation only. The hyperfine interaction transfers angular momentum from the nuclear to the electron spin system and visa versa effectively, therefore the electronic spin system influences the nuclear spin system as much as the nuclear affecting the electronic spin system, albeit in a slower fashion due to the slower nuclear relaxation

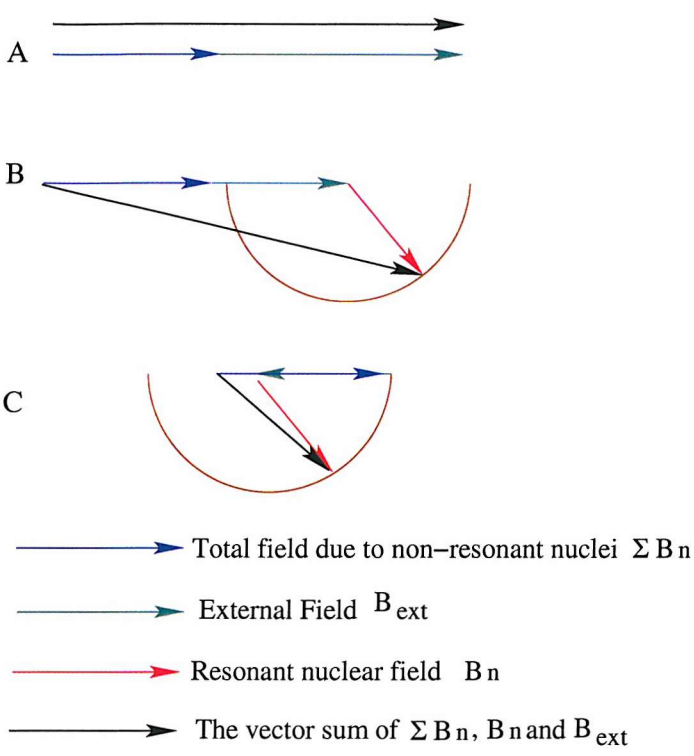

Figure 6.3: **Diagram showing the principle behind the adiabatic ODNMR technique. A) The radio frequency field is off resonance and therefore the hyperfine interaction attains its maximum value. B) The radio frequency field is on resonance with one of the nuclear species during fast adiabatic passage, the nuclear field follows the arc drawn. Thus, the electronic spin system experiences the vector sum of the external field (B_{ext}), the sum of all non-resonant nuclei ($\sum B_n$) and the oblique field B_n, denoted by the solid black line. Therefore we see electron depolarisation due to the oblique Hanle effect. C) the second resonance condition is when the hyperfine interaction is in the opposite direction to the external field (B_{ext}), in this case the change in the field experienced by the electronic spin system is greater and therefore easier to detect.**

time. We therefore would expect the line-shape of the passage through resonance to be very complicated.

There are a number of other influences of the ODNMR line-shape, the largest being inhomogeneities in the nuclear polarisation. SAQDs exist in a highly strained matrix and therefore different dots will experience slightly different environments. The electron spin system also are subject to slightly different confinement regimes and through the hyperfine interaction, is the nuclear spin system.

The largest disadvantage with adiabatic fast passage is the speed with which resonance must be passed through. ODNMR can only be observed for systems with $T_1 >> T_2$. In other words we require the passage through resonance to be slow enough that the resonant isotopes spin population, is unchanged, and therefore adiabatic passage may be realised, but fast enough that we can neglect exchange of spins with the lattice, (faster than T_1).

It is important to note, the word adiabatic pertains to the quantum mechanical interpretation, and not the thermodynamic interpretation, namely the evolution of a statistical ensemble when an external parameter is changed in such a way that no transitions are induced, and the population of the various energy levels remain unchanged [20].

6.2.2 The Oblique ODNMR Technique

Guerrier [6] noted that the oblique ODNMR technique has a number of advantages over the adiabatic fast passage method. If the adiabatic fast

passage technique is used when coupled with a low photoluminescence efficiency from the sample, then this would make detection of an ODNMR signal particularly difficult due to the fact that the NMR signal only exists during resonance, and therefore very little time is available during the passage of resonance for the signal to be collected by the detector system. This was borne out when we failed to obtain any ODNMR signal in NU1654 using the adiabatic fast passage technique.

The oblique ODNMR technique relies on the fact that the transverse Hanle effect line-shape is quite different from the oblique Hanle effect line-shape, this may be clearly seen in figure 2.6 and is due to the existence of a nuclear field in the oblique Hanle curve as given in equation 2.24.

Nuclear polarisation may be suppressed by the use of radio frequency radiation at the nuclear resonance frequency of one of its isotopes. Therefore, if the sample is tilted, a nuclear field will build up in a short time. When the radio frequency radiation is tuned to one of the nuclei's resonant frequencies, flip–flip transitions, (as given by equation 6.1), between the nuclear states are allowed. This has the effect of increasing the nuclear spin temperature and therefore usually decreasing the corresponding electron spin polarisation through the hyperfine interaction.

Fast adiabatic sweeps are also not required because the method used to detect the nuclear resonance, does not depend on the time of passage of rotation of nuclear spins as in the adiabatic technique. Instead, nuclear polarisation is decreased by the random transitions between different spin states at resonance, and, does not depend the actual passage through resonance.

This improves signal to noise by freeing time lost to equipment response. The detection of nuclear resonances is achieved by recording the change in electron spin polarisation as the nuclear field is first adiabatically reversed, in a manner similar to the previous technique, and then destroyed on passage of the radio frequency field through resonance. Finally it is restored by the hyperfine interaction with the optically oriented electrons.

The resonance signal shape therefore has the form of a sharp rise and slow exponential fall or, depending on the sign of the electron g factor and nuclear gyro-magnetic ratio, a sharp fall and slow exponential rise. This may be very easily seen in the two Hanle curves recorded in figure 6.4. For a sample orientation of 66^o, an ODNMR signal taken with a static external magnetic field less than 0.4Tesla , would be positive, and negative for fields greater than 0.4 Tesla.

For the above reason, the line-shape is further complicated by the position of the maximum of the oblique Hanle curve. This has the effect of artificially making some resonances far stronger than others and may also change the sign of the resonance line during the same radio frequency sweep. Another advantage is the observation of the exponential repolarisation of nuclei via the hyperfine interaction with electrons after resonance de-polarisation provided the radio frequency field is not swept too slowly.

The magnitude of the signal is greatest when the field due to the resonant nuclear isotope is completely removed, therefore slower radio frequency sweep times improve the signal to noise ratio. Additionally, this simultaneously increases the light collected by the Germanium detector, and therefore also improves the signal to noise ratio.

Balanced to this are the spikes due to ionising radiation. Scattering by high energy particles in the upper atmosphere causes a cascade of particles that interact with the detector. These spikes can be 10 to 100 times greater than the NMR signal. During the latter part of the experiment, we used a simple sample and hold circuit to detect when a spike occurred and hold the current value of signal for a characteristic time. This has the effect of removing the spikes at the expense of loosing detector collection time.

6.2.3 Quadrapole Effects

No description of NMR would be complete without reference to quadrapole effects. In systems where energy is transferred from electromagnetic radiation to the energy of the carriers, conservation of energy and momentum disallows transitions between energy levels of more than one quanta. For a nuclear spin system, transitions involving more than one quantum of spin are therefore forbidden [21] [22], (i.e. $|\frac{3}{2}, \frac{3}{2} >$ to $|\frac{3}{2}, -\frac{3}{2} >$).

However, in 1977 quadrapole transitions were observed in a p–type Al_x-$Ga_{(1-x)}As$ sample [23] [10], and although no theoretical understanding had been given at the time, it was plain that the observations were due to the quadrapole transition. It was later shown that the observed forbidden transitions were due to a finite mixing between the I=$\frac{1}{2}$ and the I=$\frac{3}{2}$ states, and therefore the normal magnetic dipole rules [22] do not apply.

All nuclei with a spin greater than $\frac{1}{2}$ possess an electric quadrapole moment [8]. For SAQDs quadrapole effects perturb the ODNMR signal considerably due to the nature of the growth mechanism of these structures. Unlike quantum wells, the SAQDs form by deposition of material, lattice

Probability of finding In-As bonds in InGaAs		
Arrangement of unit cell Ga In	Number of possible arrangements in unit cell	Probability
4 0	1	$0.50^4 = 0.0625$
3 1	4	$4 \times 0.5^3 \times 0.5 = 0.250$
2 2	6	$6 \times 0.5^2 \times 0.5^2 = 0.375$
1 3	4	$4 \times 0.5.5^3 = 0.250$
0 4	1	$0.5^4 = 0.0625$

Table 6.1: **Table showing the probability of finding an indium-arsenic bond in a Zinc-Blende type lattice. There are a maximum of 4 atoms that can bind to arsenic, assuming there is equal probability of finding either a gallium atom or an indium atom at one of these sites, the binomial distribution gives us the fraction of unit cells with one, two, three or no indium atoms bonded to arsenic. The table shows 25% (0.250) of As atoms are adjacent to one indium atom and three indium atoms respectively, 37.5% (0.375) are adjacent to two indium atoms, and only 6.3% have no indium atoms adjacent to them and therefore do not suffer an electric field gradient.**

mismatched to the substrate material. Minimisation of the free energy causes three dimensional growth to be favourable, and therefore SAQDs from on the substrate, (for a more in depth discussion, see chapter 2).

The SAQDs tend to form slightly distorted shapes due to the slightly different strain field experienced by each SAQD. For the type of SAQD in our samples, no time was allowed after the initial growth to allow the structure relax which produces an uneven strain distribution throughout the structure. Further distortion from the capping layer also causes an uneven strain distribution field. Therefore not only would it be difficult to detect quadrapole resonances in SAQDs due to the slightly different strain fields that each dot exists in, but the transfer of energy between dipole and quadrapole resonances could modify the NMR signal strengths.

The quadrapole signal is also subject to the number of indium atoms in the lattice that form a bond with arsenic, and are therefore subject to an electric field gradient. For this purpose, we may use the binomial distribution [24] to find the statistical fraction of atoms perturbed by indium. For a random distribution, and indium concentration of 50 % the binomial distribution gives us the probability:

$$P(m) = \begin{pmatrix} n \\ m \end{pmatrix} p^m (1-p)^{n-m} \tag{6.3}$$

describing the likelihood of obtaining m orientations for n possibilities where:

$$\begin{pmatrix} n \\ m \end{pmatrix} = \frac{n!}{m!(m-n)!} \tag{6.4}$$

This therefore allows us to calculate the total percentage of indium–arsenic bonds in an InGaAs lattice. The results are shown in table 6.1. Arsenic can bond with a maximum of four atoms in the InGaAs lattice. For equal numbers of In and Ga atoms bonding with arsenic, column one shows the possible arrangement of atoms in the unit cell, column two describes the total number of arrangements for the number of In/As atoms in column one, column three shows the binomial distribution calculated for this arrangement and multiplied by the number of arrangements in the unit cell. As may be seen there are only 6.25% of indium atoms that are not perturbed by an electric field gradient because there are no indium atoms forming a bond with arsenic.

The ^{75}As, ^{69}Ga and ^{71}Ga all have a spin of $\frac{3}{2}$, however, ^{113}In and ^{115}In have a spin of $\frac{9}{2}$ and also exhibit the largest quadrapole splitting, because it also possesses the largest electric quadrapole moment, (see table 6.2). We therefore suggest that our sample, NU1654, is heavily perturbed by quadrapole transitions.

6.2.4 Experimental Information

The experimental setup has already been extensively described in chapter 3 and no further mention of it will be made here. In order to obtain the largest NMR signal, and assuming the nuclear polarisation is fully suppressed during the passage through resonance, we required the greatest difference between the two curves. Thus, to facilitate this, the transverse

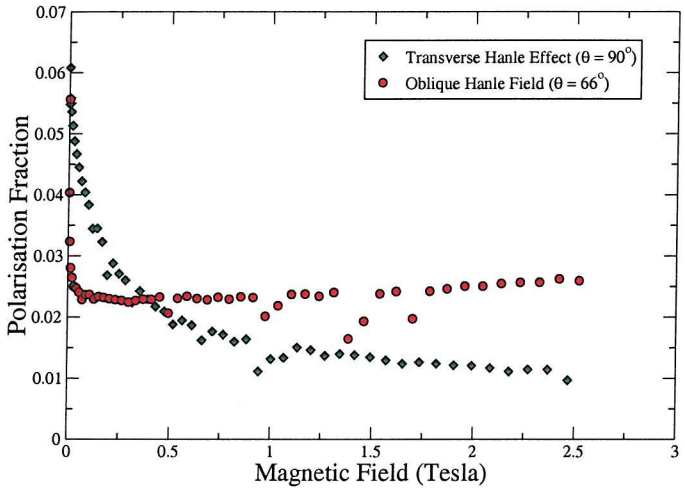

Figure 6.4: **Diagram showing example transverse and oblique Hanle effect curves for NU1654. Successive oblique Hanle curves for different angles (θ) were obtained in order to obtain the greatest difference between the oblique and transverse Hanle curves, and therefore to obtain the greatest ODNMR signal.**

Hanle curve was compared in turn with successive oblique Hanle curves for different angles θ.

We obtained the largest ODNMR signal for a particular orientation of the sample in this manner. Figure 6.4 shows an example of the two curves where the greatest change in polarisation may clearly be seen. The Hanle curves in this case were obtained from sample NU1654.

The sample is arranged in the experiment in the same manner as that of the oblique Hanle effect with the slight difference of a search coil, which was fixed to the sample stick in such a way as to provide the radio frequency magnetic field at 90^o to the sample growth direction and 90^o to the external magnetic field. A nuclear field is induced by optical orientation of the conduction electrons by the tilting of the sample in the external magnetic field. This makes an angle between the external magnetic field and incident light less than 90^o.

One assumption we should note is that on tilting the sample in the field, we also change the angle the incident light makes with the sample. However the difference between the refractive indices is so large that we believe the light still interacts with the SAQDs at, or very close to parallel to the samples growth direction. We assume therefore, that the initial electron spin direction is always parallel to the sample growth direction.

The samples were then cooled to 10K in a continuous flow cryostat, and an external magnetic field was provided by the electromagnet orientated in the same manner as the Hanle effect measurements. Once the external magnetic field had reached its set value, the experiment was left for between five and twenty minutes with the laser radiation incident on the

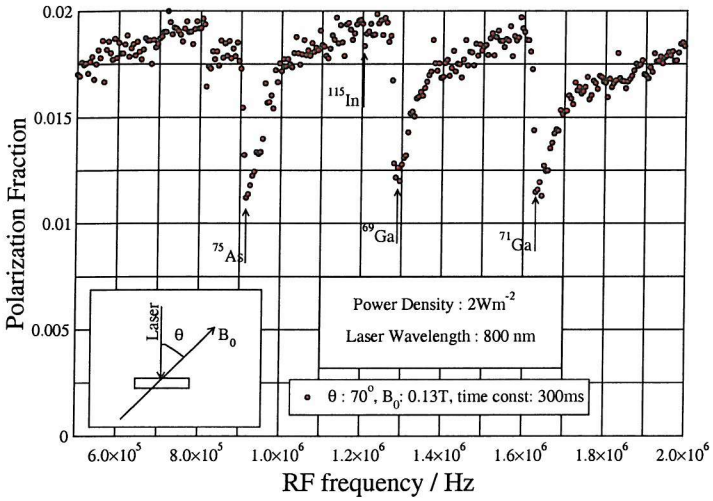

Figure 6.5: **Diagram showing results from the ODNMR experiments on sample NU1654, The inserts show the sample orientation and relevant values used to take the scan**

sample.

This allows enough time for optical orientation to align the nuclear spin system. Then the radio frequency field is swept through the dipolar resonances of gallium, arsenic and indium, simultaneously, the degree of polarisation of the recombination luminescence was recorded for the entire photoluminescence line-width in the same manner as the Hanle effect measurements (chapter 5). In order to improve the signal to noise ratio, successive ODNMR spectra were averaged together.

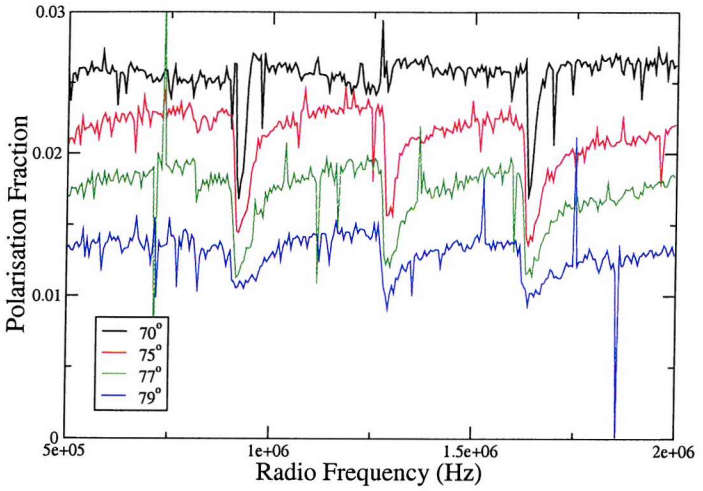

Figure 6.6: **Diagram showing successive ODNMR spectra for different angles θ. Large spikes present in the data are due to the interaction of the detector with charged particles.**

6.3 Results

The ODNMR spectrum of NU1654 is shown in figure 6.5. It was obtained by sweeping the radio frequency field from 0.5 to 2.0 MHz in a static external magnetic field of 0.13 Tesla, with the sample in a tilted field orientated at 70° to the growth direction. The dipolar ^{75}As, ^{69}Ga and ^{71}Ga resonances are clearly shown, however, the ^{113}In and ^{115}In resonances could not be detected.

A number of methods were then devised to try and detect the missing indium resonance. The first being to ensure the equipment was working over the frequency range of the experiment. A small subset of experiments were then devised to try and obtain the indium resonance signal.

The first experiment swept the external magnetic field with a static radio frequency field, set at the resonance frequency of one of the indium isotopes (9.33MHz). Unfortunately, it was not possible to increase the external magnetic field to above 0.12 Tesla, or lower the radio frequency field below 0.1MHz due to equipment restrictions (see chapter 3), therefore we used an external magnetic field of 0.1 Tesla, and expected a resonance frequency of 0.933MHz for ^{115}In. We tried this at a number of different tilts of the sample, and also tried averaging many sweeps to no avail.

Finally, we took successive oblique Hanle curves in the presence of the indium resonance frequency and compared the line-shape with that of the same curves with no radio frequency field applied. We found no shift in the curves due to the presence of indium and therefore, conclude that the dipolar indium signal must in some way be suppressed.

In order to prove the resonances seen are from the dipolar ^{75}As, ^{69}Ga and ^{71}Ga isotopes, we repeated the experiment for different orientations (θ) of the sample, the peak positions are then graphed with the external magnetic field strength. The individual ODNMR spectra for a selection angles may be seen in figure 6.6.

A simpler method is to keep the orientation fixed and examine the ODNMR signal for differing values of external magnetic field. Due to the dipolar nature of the resonance, we expect a linear relationship between the peak position of the resonance and the external Magnetic field. These curves are shown in figure 6.7 where the straight lines are a least squares fit to the data. The gradient showing that the resonances do indeed correspond to the dipolar resonances as shown in table 2.1.

Finally we wanted to examine the recovery of the nuclear spin temperature. Under conditions of continuous illumination, the electronic spin system tends to re-orient the nuclei via the hyperfine interaction in a characteristic time T_1. The reorientation tends to show an exponential change in electron polarisation with time, this could be either a rise, or a decay depending on the relative displacement of the transverse and oblique Hanle curves. The characteristic time T_1 may be obtained by a least squares fit to the data. The following equation was used:

$$y(t) = A0e^{(-\frac{t-A1}{A2})} + A3 \tag{6.5}$$

to the data, where $A0$ to $A3$ are fitting parameters, with the following results: $A0 = (5.66 \pm 0.03) \times 10^{-3}$, $A1 = 45 \pm 5$, $A2 = 37.708 \pm 0.003$, $A3 = 0.024 \pm 0.001$. The data and fitted curve is shown in figure 6.8.

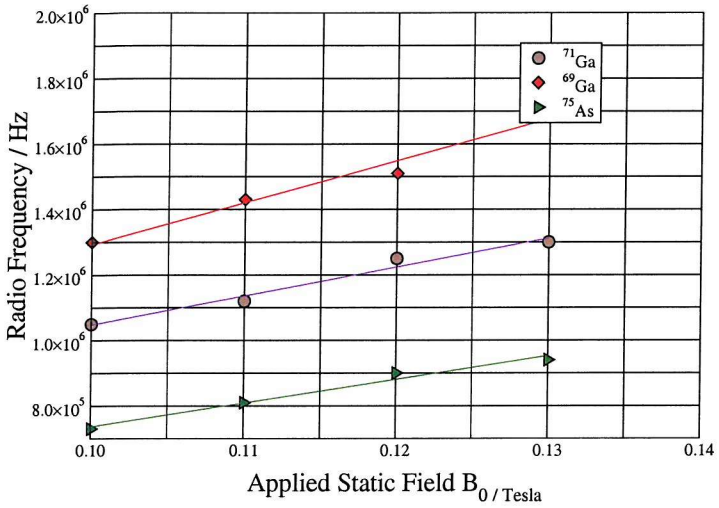

Figure 6.7: **Diagram showing the peak positions of the dipolar nuclear peaks in the ODNMR spectra for each of the nuclear isotopes identified in sample NU1654.**

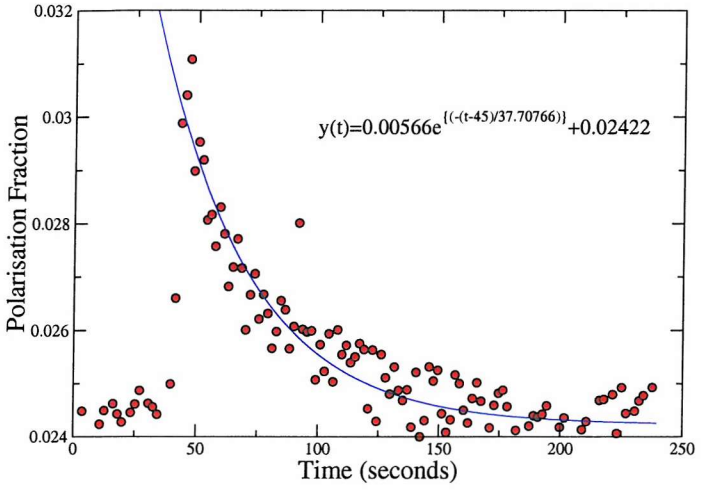

Figure 6.8: **Diagram showing a fitted exponential curve to the recovery of ^{69}Ga resonance peak. The external magnetic field was set to 0.13 Tesla with a sample orientation of 70^o.**

Nuclear Quadrapole Moments of Isotopes		
Isotope	Electric Quadrapole Moment (Q)	Natural Abundance (%)
^{69}Ga	0.178	60.4
^{71}Ga	0.112	39.6
^{113}In	1.14	4.28
^{115}In	1.16	95.72
^{75}As	0.3	100

Table 6.2: **Table showing the quadrapole moments of the isotopes in the sample NU1654, in units of barns (x10^{-24}cm^2). Source in reference [25]**

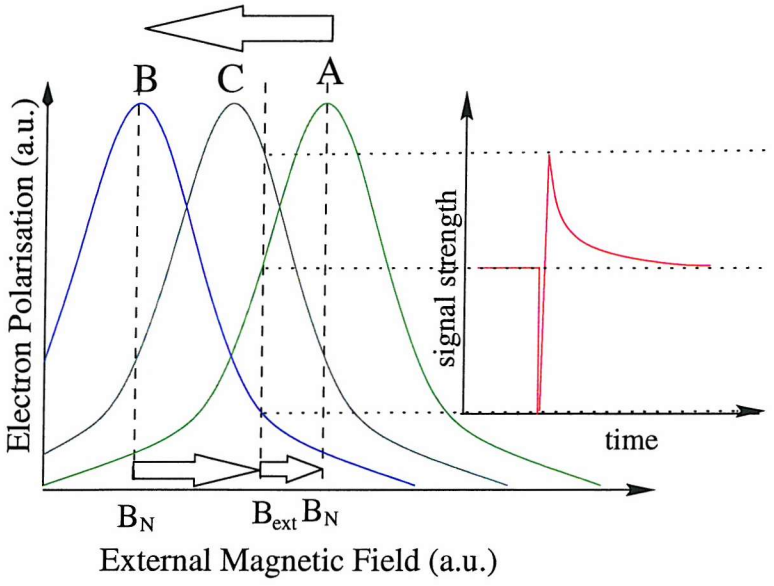

Figure 6.9: **Diagram showing the line-shape of the ODNMR signal as the radio frequency passes through resonance.**

6.4 Discussion

The missing ^{113}In signal was quite expected in that it has a natural abundance of only 4.28%. Therefore there are not many ^{113}In isotopes available to be able to contribute to the NMR signal. However, the ^{115}In signal should have been very strong because of the high concentration of indium in the $In_{0.5}Ga_{0.5}As$ sample. To further compound the problem, the one mechanism that can change both the NMR shape and strength, namely the quadrapole interaction has always been found to be a very weak signal [26].

The line profile of the oblique ODNMR signal is also affected due to the displacement of the oblique Hanle curve relative to the fixed magnetic field, the principles of which are given below: Before resonance, the peak

of the oblique field Hanle curve is displaced from zero field as discussed in chapter 2, and shown in figure 6.9, (A).

Then as the radio frequency reaches resonance, the nuclear spin rotates through 180° to point in the opposite direction to that of the external magnetic field, as in adiabatic fast passage. Due to the sudden change in nuclear spin the Hanle peak rapidly shifts to B, and therefore the electronic polarisation after resonance is lower than the original value. Our apparatus cannot resolve this fast component because the long collection time per point is far longer than the time it takes for the next stage of the passage through resonance to occur, (B $\Rightarrow$ C).

This occurs because as the radio frequency continues through resonance, the transverse Hanle effect causes a rapid de-polarisation of nuclei due to the transverse relaxation mechanism. This spin-lattice relaxation produces a rapid shift of the Hanle curve back to position B. Finally, the slow exponential recovery of spin polarisation occurs under the influence of optical orientation [27].

There are only a few ways in which the indium signal might be suppressed, the first of these is that the Zeeman energy levels may not be sufficiently well separated to produce a population difference, and therefore nuclear polarisation would be significantly reduced as the overlap of the wave-functions would allow a decrease in the spin-spin interaction time.

Another possibility is the loss of the nuclear spin polarisation due to relaxation mechanisms. We do not have any proof of which mechanism may be responsible for the indium results. Therefore here follows a simple discus-

sion on general relaxation mechanisms, and their application to SAQDs.

There are two different types of nuclear spin in crystal lattices [28]. The first type are spins located close to areas of localised electron wave-functions. The example given in Abragam is that of impurities which localise electrons due to the abrupt change in charge distribution at the impurity site. Obviously, the confinement of electron wave functions within the area of a quantum dot also provides the same type of confinement. These spins are directly relaxed via their hyperfine coupling to electrons trapped on the impurity, as are spins located in the vicinity of the quantum dots. This is because the localisation of the electron wave function allows stronger coupling between the electrons and nuclei as given in equation 2.24. Consequently this leads to stronger coupling in SAQDs and is the most obvious possible mechanism for the lack of nuclear spin polarisation in indium.

The second type of spin are from nuclei located further away from centres of localised electrons. These nuclei are relaxed via transport of magnetisation from the nuclei that are close to electron wave functions. This process is often called spin diffusion and becomes possible due to the existence of spin-spin interactions between different nuclei. Therefore we can define the diffusion radius as the distance from the centre of the localised electron that distinguishes the two different types of nuclei [29].

Nuclear relaxation is therefore a function of both of these relaxation mechanisms, usually these may not be studied independently of each other, however Malinowski has managed to examine spin diffusion via specialised quantum well structures [30]. In order to examine how the nuclear relaxation could influence the ODNMR signal, we have to examine their transition probabilities. Abragam gives complete details in reference [31].

The Hamiltonian for nuclear spin-phonon coupling is given by:

$$\hbar H_{sp} = \hbar \sum_q F^{(q)} A^{(q)} \tag{6.6}$$

where $F^{(q)}$ and $A^{(q)}$ are the lattice and nuclear spin operators respectively. The operator F has the dimensions of frequency, A is dimensionless. In general, F is a function of the relative positions of neighbouring atoms. F is in general a function of the relative positions of neighbouring atoms in a lattice, $(r_1 - r_2 + u_1(r_1) - u_2(r_2)$ where $u_i(r_i)$ represents the wave function of atom i at position r_i). We use the first order approximation $(u_1 - u_2)_x \approx (r_1 - r_2)\frac{\partial u_1}{\partial x}$ and expand F in terms of the stresses:

$$W_{ik} = \frac{1}{2}\left(\frac{\partial u_i}{\partial x_k} + \frac{\partial u_k}{\partial x_i}\right) \tag{6.7}$$

of the lattice, an expansion we write symbolically thus:

$$F = F_0 + F_1 W + F_2 W^2 + F_3 W^3 + ... \tag{6.8}$$

$F_1 W$ describes the absorption or emission of a single phonon, $F_2 W^2$ describes the absorption or emission of two phonons, or the Raman process, the absorption and simultaneous emission of a single phonon etc, F_1, F_2, F_3 have dimensions of frequency and are all of comparable magnitude.

The transition probability is actually particularly difficult to calculate because the strain distribution has to be taken into account. Although a few authors have calculated the strain distribution [32] [33] [34], as far as we know, no one has examined the nuclear levels of a highly strained crystal such as the SAQD environment. However, we can say that all terms in

the transition probability are generally small, the main feature being a $\frac{1}{T_{sp}}$ relationship to the square of the frequency of the phonon where T_{sp} is the characteristic time of this process. The physical reason for the inefficiency of the direct process is due to the fact that only phonons in the neighbourhood of the frequency ω_o contribute. Therefore if the nuclear levels happen to correspond to the phonon energy, nuclear relaxation in indium could become a favourable relaxation mechanism.

A far smaller relaxation mechanism is that of nuclear spin-spin interactions, or nuclear spin diffusion [29]. Nuclear spin diffusion relies on mutual spin flips from like isotopes which do not involve energy exchange with the lattice, and therefore the additional indium introduced in the GaAs lattice to produce the SAQDs also introduce additional dipolar and quadrapolar disorder. Therefore we do not believe this mechanism would play a significant role in the relaxation of indium isotopes.

The last relaxation mechanism is that of the nuclear quadrapole interaction. The nuclear quadrapole interaction is calculated by examining the mutual electrostatic interaction due to, both electron and the nuclear charge distributions [35]. The Hamiltonian describing a nucleus of spin I in the presence of an external field (B_{ext}) contains two terms:

$$H = H_z + H_Q \tag{6.9}$$

the first term is the normal Zeeman term, given as:

$$H_z = \gamma \mathbf{I} \bullet \mathbf{B_{ext}} \tag{6.10}$$

The second term is the quadrapole interaction. Due to the fact that the

quadrapole interaction is direction dependent, H_Q is also direction dependent. Therefore we define a set of coordinate axes using a symmetric tensor V_{ij} that describes the efg due to the electron distribution, with off diagonal elements equal to zero plus an extra term that describes the deviation from these axes due to distortion of the lattice (η). H_Q is given as:

$$H_Q = A\left[3I_z^2 - I(I+1) + \frac{1}{2}\eta(I_x^2 = I_y^2)\right] \tag{6.11}$$

where A is a constant given as:

$$A = \frac{e^2qQ}{4\hbar I(2I-1)} \tag{6.12}$$

Here Q is the nuclear quadrapole moment, and if we choose the tensor such that $|V_{zz}| \geq |V_{xx}| \geq |V_{yy}|$, then $\eta = \frac{V_{xx}-V_{yy}}{V_{zz}}$. Table 6.2 lists the electric quadrapole moments of the gallium, indium and arsenic isotopes. One thing that does stand out is the fact that the cross-section for Indium is greater than that for any of the other isotopes. Therefore according to equation 6.11, we can say that the indium quadrapole signal should perturb our samples considerably, however, this has always been found to be a very weak effect.

6.5 Conclusion

This work represents the first study to show nuclear effects in SAQDs. We have observed the gallium and arsenic isotope resonances, however, we could not observe the indium resonance. We have also presented a number of different experiments to try and resolve an indium resonance to no

avail. Therefore we assume the indium resonance is somehow suppressed. In order to explain the absence of the indium signal, we have also given a number of possible relaxation mechanisms that might contribute to the absence of the signal.

It is however, almost impossible to examine any of these mechanisms under the current experimental setup. An enormous amount of work needs to be completed in order to provide quantitative results for these structures, two points show themselves as more important than all others. The first is the need to obtain luminescence from single SAQDs. Knowledge and observation of excited states may allow resonant or near resonant pumping, allowing accurate examination of the electronic structure. This would in turn allow experiments to be made on the signal strengths, and therefore transition probabilities to be examined. The second point is the use of a stronger electromagnet as higher external fields will ensure the different spin states of the nuclear levels are sufficiently split to ensure a nuclear spin temperature under optical orientation.

Bibliography

[1] D. Gammon, S. W. Brown, E. S. Snow, T. A. Kennedy, D. S. Katzer, and D. Park, Science, **277**, 85 (1997)

[2] A. W. Overhauser, Phys. Rev, **91**, 476 (1953)

[3] A. W. Overhauser, Phys. Rev, **92**, 411 (1953)

[4] A. I. Ekimov and V. I. Safarov, JETP Lett, **15**, 319 (1972)

[5] G. P. Flinn, Ph.D. Thesis, Laser Spectroscopy of Semiconductor Quantum Wells, University of Southampton, (1991)

[6] Daniel J. Guerrier, Ph.D. Thesis, Optically Detected Nuclear Magnetic Resonance in Semiconductors, University of Southampton, (1997)

[7] D. J. Guerrier, and R. T. Harley, Appl. Phys. Lett. **70**, 1739 (1997)

[8] A. Abragam, Principles of Nuclear Magnetism, Oxford Science Publishing, (1961) (Chapter 6 Page 162).

[9] V. G. Fleisher and I. A. Merkulov, Ed. F. Meier and B.P. Zakharchenya, Optical Orientation, North Holland, (1984) (Chapter 5 Page 245)

[10] V. P. Zakharchenya, V. A. Novikov, and V. G. Fleisher, JETP Lett. **26**, 203 (1977)

[11] L. Pauling, The nature of the chemical bond and the structure of molecules and crystals, Cornell University Press, (1940)

[12] M.I. D'Yakanov, and V. I. Perel, Ed. F. Meier and B.P. Zakharchenya, Optical Orientation, North Holland, (1984) (Chapter 1 Page 63)

[13] M. Goldman, Spin Temperature and Nuclear Magnetic Resonance in Solids, Oxford Clarendon Press, (1970)

[14] M. I. D'Yakanov, and V. I. Perel, Ed. F. Meier and B.P. Zakharchenya, Optical Orientation, North Holland, (1984) (Chapter 1 Page 64)

[15] A. Abragam, Principles of Nuclear Magnetism, Oxford Science Publishing, (1961) (Chapter 3 Page 65).

[16] M. I. D'yakanov and V. I. Perel, JETP, **38**, 177 (1973)

[17] A. Abragam, Principles of Nuclear Magnetism, Oxford Science Publishing, (1961) (Chapter 2 Page 19).

[18] D. Paget and V. I. Berkovits, Ed. F. Meier and B.P. Zakharchenya, Optical Orientation, North Holland, (1984) (Chapter 8 Page 404)

[19] C. P. Slichter, Principles of Magnetic Resonance, Harper and Row, (1963) (Chapter 2 Page 18)

[20] A. Abragam, Principles of Nuclear Magnetism, Oxford Science Publishing, (1961) (Chapter 5 Page 135).

[21] G. Lampel, Phys. Rev. Lett. **20**, 491 (1968)

[22] V. G. Fleisher and I. A. Merkulov, Ed. F. Meier and B.P. Zakharchenya, Optical Orientation, North Holland, (1984) (Chapter 5, Page 221)

[23] V. I. Berkovits and V. I. Saraov, JETP Lett. **26**, 256 (1977)

[24] Jon Mathews and Robert Walker, Mathematical Methods of Physics, Addison-Wesley Publishing, (1973) (Chapter 14 page 378)

[25] C. R. Weast, Handbook of Chemistry and Physics, 69^{th} edition, CRC press, (1988)

[26] D. Paget and V. I. Berkovits, Ed. F. Meier and B.P. Zakharchenya, Optical Orientation, North Holland, (1984) (Chapter 8 Page 411)

[27] M. I. D'yakanov, V. I. Perel, V.L. Berkovits, and V.I. Safarov, Sov. Phys. JETP, **40**, 950 (1974)

[28] A. Abragam, Principles of Nuclear Magnetism, Oxford Science Publishing, (1961) (Chapter 9).

[29] D. Paget, Phys. Rev. B, **25**, 4444 (1982)

[30] A. Malinowski, M. A. Brand, and R. T. Harley, Proceedings of the 5^{th} conference on the Physics and Applications of Spin Phenomena in Semiconductors (PASPS), Sendai, Japan, September 2000.

[31] A. Abragam, Principles of Nuclear Magnetism, Oxford Science Publishing, (1961) (Chapter 9, Page 408).

[32] C. Priester, I. Lefebre, G. Allan, and 0. Lannoo, Mechanisms of Thin Film Evolution, MRS Symposia Proceedings No. 137 (Materials Research Society, Pittsburgh, 1994), Page 131

[33] S. Christiansen, M. Albrecht, H.P. Strunk, and H.J. Maier, Appl. Phys. Lett. **64**, 3617 (1994)

[34] M. Grundmann, O. Stier, and D. Bimberg, Phys. Rev. B **52**, 11969 (1995)

[35] A. Abragam, Principles of Nuclear Magnetism, Oxford Science Publishing, (1961) (Chapter 6 Page 160).

[36] J. A. Marohn, P. J. Carson, J. Y. Hwang, M. A. Miller, D. N. Shykind, and D. P. Weitekamp, Phys. Rev. Lett. **75**, 1364(1995)

Chapter 7

Future Work and Conclusions

7.1 Conclusions

We have measured the exciton g-factors of a range of $In_{0.5}Ga_{0.5}As/GaAs$ SAQDs. These results are the first presented in the low field regime for these structures. The Zeeman splittings generally show a linear field dependence at low field values as expected in these systems. There are also non–linearities at higher fields due to we believe, field induced mixing between the optically active and the optically inactive exciton states. For circularly polarised light, the ellipticity of the recombination radiation shows that the spin relaxation time (τ_s) is greater than the recombination time (τ_r) as expected due to the localisation of their carrier wave-functions, and this therefore, together with the non symmetric nature of the Zeeman splitting, led us examine the nuclear field in these structures.

The method used to obtain the exciton g-factors is both simple, reliable and accurate as shown by other authors [1][2][3], and has been used for many years successfully on quantum wells. However, it has not been possible to obtain the mechanism for the apparent Zeeman splitting in the SAQD samples due to the fact that, excited states and bi-exciton features would be hidden in the large photo-luminescent line-width of these samples, and therefore the existence of these states could introduce a fictitious splitting value due to the asymmetry of the photo-luminescent line-profile, however, we have no evidence of the presence of any other states other than the ground state in any of our samples.

In the Hanle effect measurements, we have found the sign of the electron g-factor in the two samples measured to be negative. For the transverse

Hanle curves, we find a similar strange behaviour which we attribute to the suppression of spin relaxation for these systems in low excitation powers. This is not unexpected and has been theoretically investigated by Benisty [4] [5], who predicted a low scattering rate in SAQDs and therefore, a corresponding long spin relaxation time. Paillard [6] is the only experimental paper dealing with the spin relaxation time in SAQDs, and we find a similar result in that the spin relaxation time is much longer than the recombination time.

For sample NU1654, we find the spin relaxation time to be $(3.0\pm0.2)\times10^{-9}$ seconds assuming a recombination time of 950×10^{-12} seconds. The maximum average nuclear field in NU1654 was found to be 0.205 ± 0.001 Tesla. No quantitative results were found for sample NU1660 due to the strange behaviour of the oblique Hanle peaks and the absence of an experimentally determined value of the recombination time.

The ODNMR measurements in sample NU1654 represent the first study to show nuclear effects in SAQDs. We have shown the gallium and arsenic isotope resonances, however, we could not observe the indium resonance. We have also presented a number of different experiments to try and resolve an indium resonance to no avail. Therefore we assume the indium resonance is somehow suppressed. In order to explain the absence of the indium signal, we have also presented a number of possible relaxation mechanisms that might be responsible for its absence.

7.2 Future Work

In order to obtain more quantitative measurements, we believe it is necessary to decrease the size distribution of SAQDs either excited by the laser, or detected by the the experimental apparatus. There are a number of methods that have already been used in order to accomplish this. However, one of the easiest methods is the growth of a single layer of material on top of the sample. Selective etching or electron beam desorption would allow a fine hole to be made in this structure down to the substrate layer.

The material used to make the mesa structure should be opaque to the laser radiation, in this way it is possible to irradiate only a small number of quantum dots. At the same rate, the mesa structure should also be transparent to luminescence wavelengths in order to maximise the amount of light collected. This would give additional information on the electronic structure, which in turn would allow us to obtain the Zeeman splitting for individual SAQDs, without the additional contributions from either the other states from different SAQDs, or from other electronic states in the same SAQD. Additionally, the Zeeman splitting of the excited states, or bi-excitonic states, if any exist may be resolved.

The observation of singular excited states would also facilitate improvements in the ODNMR experiments. Excitation could be tuned to one of the excited states which would allow resonant pumping to occur and the total energy spectrum could be examined. Another possibility is the modification of the ODNMR experimental apparatus, examination of the Overhauser effect in the presence of a radio frequency field would allow

the shift as the frequency passes through resonance to be examined. If the section of the photoluminescence curve that has the greatest slope is recorded, the shift in the peak as the radio frequency signal passes through resonance would show the largest change of signal possible. Using this method might produce evidence of the indium dipolar signal. The use of a stronger electromagnet as higher external fields will ensure the different spin states of the nuclear levels are sufficiently split to ensure a nuclear spin temperature under optical orientation.

Finally, ODNMR has been shown to be very useful in obtaining information on the nuclear structure in these structures, it would be very interesting to obtain some of the low density SAQDs, these are grown in the same manner as our samples but are allowed to relax after growth, leading to lower density, larger radius quantum dots. It is possible to obtain luminescence from individual dots in this case so a mesa structure would not be required.

Bibliography

[1] E. Blackwood, Ph.D. Thesis, Spin-polarised Dynamics in quantum wells, University of Southampton, (1993)

[2] M.J. Snelling, Ph.D. Thesis, Optical Orientation in Quantum Wells, University of Southampton, (1991)

[3] N. J. Traynor, Ph.D. Thesis, Magneto-optics of excitons in quantum wells, University of Southampton, (1996)

[4] H. Benisty, C. M. Sotomayer-Torres, and C. Weisbuch, Phys .Rev. B, **44**, 10945 (1991)

[5] H. Benisty, Phys. Rev. B, **51**, 13281 (1995)

[6] M. Paillard, X. Marie, E. Vanelle, T. Amand, V. K. Kalevich, A. R. Kovsh, A. E. Zhukov and V. M. Ustnov, Appl. Phys. Lett., **76**, 76 (2000)

[7] J. A. Marohn, P. J. Carson, J. Y. Hwang, M. A. Miller, D. N. Shykind, and D. P. Weitekamp, Phys. Rev. Lett. **75**, 1364(1995)